Pontifícia Universidade Católica
do Rio de Janeiro

Renata Lorenzoni

Characterization of strain-hardening cement-based composites: Deep Learning, in-situ X-ray microCT and Digital Volume Correlation

Tese de Doutorado

Thesis presented to the Programa de Pós–graduação em Engenharia de Materiais e de Processos Químicos e Metalúrgicos of PUC-Rio in partial fulfillment of the requirements for the degree of Doutor em Engenharia de Materiais e de Processos Químicos e Metalúrgicos .

Advisor : Prof. Sidnei Paciornik
Co-advisor: Prof. Flávio de Andrade Silva

Rio de Janeiro
November 2021

Pontifícia Universidade Católica
do Rio de Janeiro

Renata Lorenzoni

Characterization of strain-hardening cement-based composites: Deep Learning, in-situ X-ray microCT and Digital Volume Correlation

Thesis presented to the Programa de Pós–graduação em Engenharia de Materiais e de Processos Químicos e Metalúrgicos of PUC-Rio in partial fulfillment of the requirements for the degree of Doutor em Engenharia de Materiais e de Processos Químicos e Metalúrgicos . Approved by the undersigned Examination Committee.

Prof. Sidnei Paciornik
Advisor
Departamento de Engenharia Química e de Materiais – PUC-Rio

Prof. Flávio de Andrade Silva
Co-advisor
Departamento de Engenharia Civil – PUC-Rio

Prof. José Roberto Moraes d´Almeida
Pontificia Universidade Católica do Rio de Janeiro – PUC-Rio

Prof. Daniel Carlos Taissum Cardoso
Pontificia Universidade Católica do Rio de Janeiro – PUC-Rio

Prof. Otavio da Fonseca Martins Gomes
Centro de Tecnologia Mineral – CETEM

Prof. Giovanni Bruno
Bundesanstalt für Materialforschung und -prüfung – BAM

Rio de Janeiro, November the 5th, 2021

Renata Lorenzoni

Graduated in Civil Engineering at Universidade Federal do Espírito Santo in 2013. Master's Degree in Engineering Materials and Chemical and Metallurgical Processes at PUC-Rio in 2017, specialized in the areas of: Materials Science, Digital Microscopy and Image Processing and Analysis.

Bibliographic data

Lorenzoni, Renata

Characterization of strain-hardening cement-based composites: Deep Learning, in-situ X-ray microCT and Digital Volume Correlation / Renata Lorenzoni; advisor: Sidnei Paciornik; co-advisor: Flávio de Andrade Silva. – Rio de janeiro: PUC-Rio, Departamento de Engenharia Química e de Materiais , 2021.

v., 123 f: il. color. ; 30 cm

Tese (doutorado) - Pontifícia Universidade Católica do Rio de Janeiro, Departamento de Engenharia Química e de Materiais .

Inclui bibliografia

1. Engenharia Química e de Materiais – Teses. 2. microtomografia computadorizada de raios x;. 3. segmentação;. 4. aprendizagem de máquina;. 5. correlação digital de volume;. 6. compósitos cimentícios reforçados com fibras.. I. Paciornik, Sidnei. II. de Andrade Silva, Flávio . III. Pontifícia Universidade Católica do Rio de Janeiro. Departamento de Engenharia Química e de Materiais . IV. Título.

CDD: 620:11

Acknowledgments

First and foremost, I would like to deeply thank my advisor, Professor Sidnei Paciornik, who trusted and encouraged me in this Ph.D. thesis. Professor Paciornik taught me beyond his great technical knowledge, but mainly about working with respect, cordiality, and kindness. Sidnei inspires me as a professional and as a person, and I hope to carry some of his wisdom into my life.

I wish to express my deepest gratitude to my co-advisor, Professor Flávio Silva, for so much knowledge shared in the cementitious materials field, which was essential for this work and will be fundamental in my academic career. I also strongly thank him for the trust placed in me to carry out a Ph.D. exchange program at TU Dresden.

I am grateful to Professor Viktor Mechtcherine, who welcomed me into his group with such affection, and to Dr. Iurie Curosu, who supervised me with such patience and dedication during my stay in Dresden. It was an exchange of knowledge and culture, which led me to great professional and personal growth, and I am deeply grateful for this opportunity.

I would like to express my gratitude to Professor Giovanni Bruno and his group, who welcomed me at Federal Institute for Materials Research and Testing in Berlin. Especially for Dr. Fabien Léonard, who led me in the in-situ microCT test and shared his knowledge about the technique.

I wholeheartedly thank each one from the Research Group in Digital Microscopy and Image Analysis, who were always available to help and who provided me so many fun moments, making hard work and difficult days lighter. A special thanks to Dr. Marcos Henrique, who calmly and patiently always helping and encouraging the work of all students.

To my friends, who become my family in Rio de Janeiro and played this role in these six years. I am deeply grateful to have had on this journey good friends to rely on hard times and to share happy moments.

Last but not least, I would like to thanks all my family's care and love. I am grateful to my brothers Rodrigo and Rafaela and my dad Dimas for understanding and supporting me on this journey. To my nephews Lucas and Caio, for filling my life with happiness. My greatest gratitude goes to my mom Valéria, who often believed in me more than I did and encouraged me to move forward. Thanks for being my inspiration.

"Trust in the Lord with all your heart, and lean not to your own understanding. In all your ways acknowledge him, and he shall direct your paths" Proverbs 3:5-6

This study was financed in part by the Coordenação de Aperfeiçoamento de Pessoal de Nível Superior - Brasil (CAPES) - Finance code 001.

Abstract

Lorenzoni, Renata; Paciornik, Sidnei (Advisor); de Andrade Silva, Flávio (Co-Advisor). **Characterization of strain-hardening cement-based composites: Deep Learning, in-situ X-ray microCT and Digital Volume Correlation**. Rio de Janeiro, 2021. 123p. Tese de doutorado – Departamento de Engenharia Química e de Materiais , Pontifícia Universidade Católica do Rio de Janeiro.

Considering the importance of micro and mesoscale analyses to understand the macro behavior of materials, this work brings innovative solutions for analyzing 3D images obtained by X-ray micro-computed tomography (microCT). The studied material was the strain-hardening cement-based composites (SHCC), a fiber reinforced cementitious composite that achieves significant deformations through multiple cracks formation, resulting in a cementitious material with pseudo ductile features. The first challenge of this work was to recognize and quantify the constituent phases in the 3D images of SHCC obtained by microCT. Materials with complex structures may present images in which the internal phases cannot be distinguished by the classical thresholding technique, requiring the use of another technique such as segmentation by Deep Learning (DL). Therefore, this work used DL as a solution for this task. Then, the features of each phase could be correlated to the macro mechanical behavior of the material in in-situ microCT tests. Another modern method for analyzing 3D images used was the digital volume correlation (DVC). DVC is a technique that estimates full-field strain in 3D over the entire volume of the specimen by correlating imaging volumes of the specimen in unloaded and loaded states. Thus, the images obtained from tensile and compression in-situ tests could have their internal displacements measured and strain calculated. In summary, this work brought advances to the 3D image processing and analysis field, applied to cementitious materials, but which could also adapt for the analysis of various materials.

Keywords

X-ray micro-computed tomography; segmentation; machine learning; digital volume correlation; strain-hardening cement-based composite.

Resumo

Lorenzoni, Renata; Paciornik, Sidnei; de Andrade Silva, Flávio . **Caracterização de compósitos cimentícios reforçados com fibras: aprendizagem profunda, microTC de raio x in-situ, correlação digital de volume**. Rio de Janeiro, 2021. 123p. Tese de Doutorado – Departamento de Engenharia Química e de Materiais , Pontifícia Universidade Católica do Rio de Janeiro.

Considerando a importância da análise em micro e meso escala para o entendimento do macro comportamento dos materiais, este trabalho apresenta soluções inovadoras para a análise de imagens 3D obtidas por microtomografia computadorizada de raios-X (microCT). O material estudado conhecido pelo termo em inglês "strain-hardening cement-based composites" ou pela abreviação SHCC é um compósito cimentício reforçado com fibras que atinge deformações significativas através da formação de múltiplas fissuras, estabelecendo um material cimentício com característica pseudo-dúctil. O primeiro desafio deste trabalho foi reconhecer e quantificar as fases constituintes nas imagens 3D de SHCC obtidas por microCT. Materiais com estruturas complexas podem apresentar imagens em que as fases internas não podem ser distinguidas pela técnica de limiarização clássica, exigindo o uso de outra técnica como a segmentação por Deep Learning (DL). Portanto, este trabalho utilizou DL como solução para esta tarefa. Desta forma, as características de cada fases puderam ser correlacionadas ao comportamento mecânico macro do material em ensaios de microCT in-situ. Outro método moderno de análise de imagens 3D utilizado foi a correlação digital de volume (em inglês, digital volume correlation - DVC). O DVC é uma técnica que estima o campo de deformação sobre todo o volume da amostra, correlacionando as imagens 3D nos estados descarregado e carregado. Assim, as imagens obtidas nos ensaios de tração e compressão in-situ puderam ter seus deslocamentos internos medidos e deformações calculadas. Em síntese, este trabalho trouxe avanços ao campo do processamento digital e análise de imagens 3D, aplicadas a materiais cimentícios, mas que também podem se adaptar à análise de diversos materiais.

Palavras-chave

microtomografia computadorizada de raios x; segmentação; aprendizagem de máquina; correlação digital de volume; compósitos cimentícios reforçados com fibras.

Table of contents

List of figures

List of tables

1
Introduction

In the search for new technologies in the field of civil construction, to build complex structures or to retrofit and strengthen old ones, new materials have been widely developed and studied. Among them is the strain-hardening cement-based composite (SHCC), a cement-based material that can resist increased tensile stresses over a significant deformation range. Many studies have shown its high mechanical performance and proved that SHCC is a promising construction material. (1)(2)(3).

Micro and mesoscale analyses are essential for a better understanding of the material's behavior. For SHCC, studies such as the interface of the constituent phases, the propagation of the micro-cracks, and the influence of the fiber distribution could justify the mechanical SHCC behavior and then contribute to the production of SHCC with better performance (4)(5). In this context, computerized microtomography (microCT) is a non-destructive technique able to provide 3D images of the internal material structure, which is already widespread in research for the qualitative and quantitative characterization of cementitious materials (6)(7). MicroCT can be coupled to in-situ mechanical tests, revealing microstructural changes when the sample is subjected, for instance, to compressive or tensile stresses.

The 3D images obtained from the microCT technique require specific and challenging studies, mainly for materials with complex structures such as the SHCC. In this scenario, digital image processing and analysis is a field that solves tasks of getting information from images. The processing has the role of facilitating the image visualization and/or adapting it for the quantitative analysis step. Optimizing these steps with modern computational tools leads to greater precision in quantitative analysis and, consequently, more accurate results in multidisciplinary research. In this context, deep neural networks based on machine learning known as Deep Learning (DL) may be a solution for complex image processing and analysis tasks.

A typical image processing and analysis task is segmentation. Segmenting an image means to separate a region of interest for a quantitative study,

and this is usually done by determining a range of tones of gray in the image histogram, a technique known as thresholding. However, materials with complex structures may present images in which the internal phases cannot be distinguished by the thresholding, requiring the use of another technique such as segmentation by DL.

Machine learning uses algorithms that learn iteratively from input and output data, allowing computers to find hidden solutions without being explicitly programmed to do so. The basic principle of DL network is machine training so that it learns to recognize the input that the user provides. In the case of the DL network applied to image segmentation, the machine will be trained to output the phase of interest.

From an in-situ microCT, a sequence of 3D images is obtained at different loading steps of the mechanical test. In addition to the qualitative and quantitative analysis of these images, it is possible to obtain the internal local displacement and strain of the material in different loading stages during the mechanical test using the technique called digital volume correlation (DVC). DVC is another modern computational tool used for 3D image analysis. This technique calculates displacement and strain correlating sub-volumes of the specimen image in two subsequent loading stages.

The general purpose of this thesis was the use and application of modern and innovative techniques in the 3D image processing and analysis field for cement based materials. As specific purpose, the work at hand has: developed a deep neural network able to segmenting each SHCC constituent phases; extract features of the segmented phases and correlate them with the mechanical behavior of the material; develop a setup for in-situ tensile and compression microCT tests; analyze and suggest suitable DVC codes to provide displacement and strain of in-situ tensile and compression microCT tests.

This thesis was structured in an introduction (chapter 1), literature review (chapter 2) and four chapters of studies related to 3D image processing of the SHCC material, and finally a chapter with conclusion and suggestion for further works.

In chapter three microCT was used to characterize a PVA-steel fiber reinforced strain hardening cementitious composites. Segmentation was performed by thresholding, in which two phases could be quantitatively analyzed: pores and steel fibers. The hybrid composites were produced replacing PVA by steel fibers in 25%, 50%, 75% and 100% fractions and changes in pore structure

and steel fiber alignment were investigated. The results were published in the Journal of Building Engineering and the paper was entitled "The use of X-ray microtomography to investigate the shear behavior of hybrid fiber reinforced strain hardening cementitious composites" (8). In the published paper, the micro-mesostructural characterization was correlated with the behavior of the composite when submitted to shear loading.

The first challenge of this thesis arises in chapter four. In this chapter, a DL network to segment the constitutive phases of SHCC images obtained from microCT was used. This step was successfully completed and the results of the work were published in the Journal "Cement and Concrete Composites" and entitled "Semantic segmentation of the micro-structure of strain-hardening cement-based composites (SHCC) by applying deep learning on micro-computed tomography scans" (9).

The work presented in chapter five used the network developed to quantify the SHCC phases of images obtained from an in-situ microCT test. The work was published in the Journal "Cement and Concrete Research" as "Combined mechanical and 3D-microstructural analysis of strain-hardening cement-based composites (SHCC) by in-situ X-ray microtomography" (10). In this research, in-situ tensile and compression microCT test were performed in SHCC specimen and the quantitative data were related to their mechanical response. Once again, deep learning network was essential for quantitative image analysis.

The fourth and final study of this thesis involves the use of DVC to measure internal displacement and strain through microCT images. Three open source DVC codes were applied to the in-situ microCT images of tensile tests obtained from the study of the previous chapter. The result of one of these codes was presented in the conference: "28 Congresso da Sociedade Brasileira de Microscopia e Microanálise" with the title "Digital Volume Correlation (DVC) applied to in-situ microCT Images of Strain-Hardening Cement-Based Composites (SHCC)" (11).

Finally, chapter seven concludes the importance of all the techniques used in the thesis for the characterization of materials in general and shows the relevant results obtained for the SHCC.

2
Literature review

SHCC is a promising material for the civil construction industry that has the ability to resist increased tensile force after crack formation, over a significant tensile deformation range. The increased resistance is achieved through effective crack bridging by fibers, across multiple cracks of widths in the micro-range (1). Such multiple cracking results in a remarkable tensile ductility prior to failure, bringing enhanced behavior in terms of mechanical performance of elements made of or strengthened with SHCC (2)(3)(12)(13)(14).

These positive features are achieved by a purposeful adjustment of the material composition, which targets a micromechanical balance between the crack-bridging behavior of the micro-fibers and the cracking behavior of the finely-grained cementitious matrix (15)(16)(17). Moreover, the arrangement of each constitutive SHCC micro phases also influences the material response. In any case, it is clear that their analysis at micro- and meso-scale can explain the macro mechanical behavior on various loading and environmental conditions (17)(18)(19). In addition, analyses on this level can also bring information about damage formation in the material (20)(7).

MicroCT represents a powerful tool for analyses at the micro- and meso-levels, since it can generate a 3D representation of the material micro-structure (7)(21)(22). This is a non-destructive technique in which its basic principle is the attenuation of an x-ray beam when passing through the sample. As the x-ray attenuation is related to the density and the atomic number of the material, different phases in the material will generate different gray levels in the image.

In order to obtain information of the material's microstructure, each of the constitutive phases must be distinguished. This distinction in images is done through the image processing step called segmentation. The standard way to segment different phases in an image is by choosing a cut-off on gray value range on their histogram (thresholding). For fiber reinforced composites this was already done for steel fibers (22). This is facilitated by the high density of the steel fibers compared to the surrounding cementitious matrix and the resulting different x-ray absorption, leading to distinct bright areas. The voids

are easily segmented by thresholding, which results in darker areas compared to the matrix.

In the case of SHCC usually composed by tiny polymeric fibers, however, several challenges arise. First, the micro-polymer fibers and the fine aggregates in the cementitious matrices require high resolution for their detection and accurate morphologic representation. Usually this implies in a compromise between the resolution of the scans and the size of the scanned specimen. Secondly, the low density of the polymer fibers does not allow their distinction from the air inclusions just based on the gray values. Similarly, the gray-value based segmentation of the fine aggregates from the cement matrix is not possible due to their similar densities. Thus, more sophisticated segmentation techniques must be applied.

The manual segmentation by human operators is not efficient and involves significant uncertainties (23). On the other hand, machine learning is a method that uses algorithms, that iteratively learn from data, allowing computers to find hidden insights without being explicitly programmed where to search (24). In this context, deep learning (DL) is a new technique which has proven to be efficient for segmentation of materials with complex microstructures (25)(26).

Once DL technique was applied for segmentation of complex phases in the material, their microstructure analyses by 3D images obtained from microCT become possible. A standard way for such analysis is to characterize the material before and after undergoing some type of mechanical test. Thus, the appearance of damage during the test can be related to the initial microstructure of the material. This can be achieved by an ex-situ or in-situ microCT test. The disadvantage of the *ex situ* microCT approach is that the observed damage status is inaccurately reflected because of crack closure effects. In-situ CT measurements enable a very accurate damage assessment even at very critical loading conditions (27).

For both cases, the pre and post test images can be compared for analysis of internal changes that have occurred in the material. The technique that has been widely used for this type of analysis is the digital image correlation (DIC), in particular its 3D volumetric version digital volume correlation (DVC), also known as volumetric DIC. The basic principle of DIC is to assess the displacements and strains fields by comparison of two images acquired at different stages of deformation. The first image is generally referred to as the reference image (sample without being subjected to mechanical loading) and

the second, acquired after an increment of deformation, as the deformed image (28). DIC (or DVC) provides displacement vectors over a set of points (sub-volumes) in the images, from which strains can be calculated to be used, for example, to constrain theoretical or numerical models. Thus it is possible to follow the evolution of displacements throughout a sample and throughout a loading experiment (29).

In this way, the use of DL as a segmentation technique for analysis of images obtained from in-situ microCT and the sequential use of the DVC technique to understand internal changes according to their microstructure may be innovative in terms of analyzing materials such as the SHCC. In short, the motivation of this study is to achieve innovative data from the SHCC microstructure through the development and use of modern techniques related to 3D images.

2.1 The strain-hardening cement-based composite (SHCC)

SHCC is a special type of reinforced concretes which generates multiple fine cracks when subjected to increasing tensile loading (30). Figure 2.1 shows how this happens when this material is under monotonic tensile loading. As the first crack forms, the fibers bridge the crack, leading the tensile stresses across the crack surfaces. With increasing load, the formation of new crack occurs. This leads to the subsequent development of another crack at the second weakest cross-section. This repeats itself, resulting in a set of almost uniformly distributed cracks. At the tensile strength f_t the localisation of the failure occurs, namely when one main crack develops. Due to a moderate opening of a large number of fine cracks, a strain capacity of several percent can be observed (31). Therefore, many types of loading and environmental conditions have been studied for this material such as its durability, cyclic loading, impact loading, flexural behavior, shear behavior, temperatures effect, and the following subsection presents some works that analyzed the behavior of SHCC under different mechanical loads and environmental conditions.

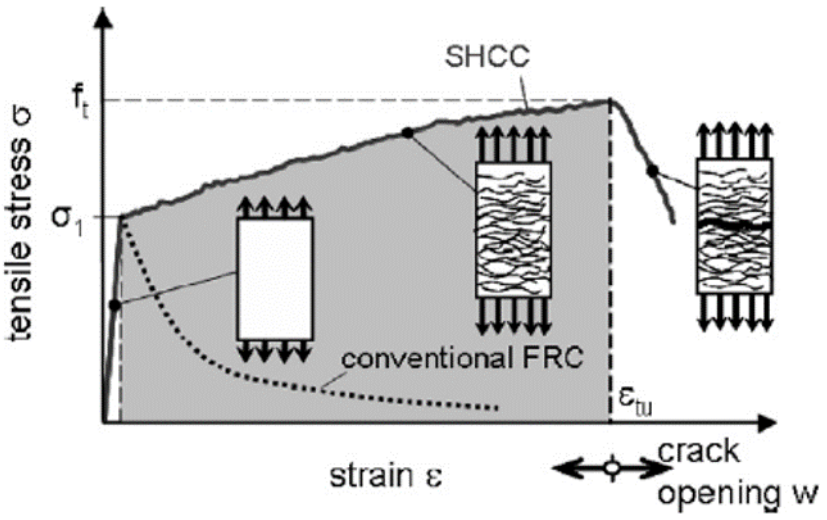

Figure 2.1: SHCC under monotonic tensile loading (31)

2.1.1 SHCC matrices and fibers

The interfacial bonding and fiber pullout properties, the material parameters of the fibers and of the matrix, the distribution of flaw sizes in the matrix, the fiber orientation and their dispersion in the matrix play an important role in the resulting composite mechanical behavior (32). Because of this, the choice of which matrix and fiber to be use in SHCC is of utmost importance.

Different matrices are used to manufacture SHCC, so the composition of the matrix can be varied in each study. For conventional matrices, the amount of the aggregate can be varied and the addition of fly ash has been constantly used. The aggregate influences the matrix strength so that it is increased with increasing sand. The addition of fly ash reduces the matrix strength, but the fiber-matrix interfacial zone is modified, leading to improved fiber slip from the matrix instead of fiber breakage (1).

Another widely used matrix is the ultra-high performance concrete (UHPC). While very high tensile and compressive strengths are achieved, such composites, in comparison to conventional SHCC, yield significantly lower strain capacities which can be traced back to less pronounced multiple cracking (18). When this matrix is used this material is also known as high-strength strain-hardening cement-based composites (HS-SHCC).

Regarding the fibers used, several types are studied as an option for SHCC composition. The SHCC can be mix designed, for example, with

polyvinyl alcohol (PVA), polyethylene (PE) or steel fiber (33). Also, hybrid fiber reinforced SHCC are studied (34)(8).

SHCC with PVA fiber is one of the most used. These fibers were analyzed separately from the matrix and the results showed that the behavior of a single PVA fiber can be considered as linear elastic–plastic and it was concluded that the components of irreversible deformation cannot be neglected. It was also concluded that PVA fiber creep can be considered insignificant (31). Other studies were carried out to reveal rate dependence in component phases (fiber, matrix, and fiber/matrix interface) and it was found that fiber stiffness, fiber strength, matrix toughness and fiber/matrix interface chemical bond strength were loading rate sensitive and they increase with loading rates in a PVA-SHCC system. These changes in component properties result in the reduction of tensile strain capacity of PVA-SHCC as the strain-rate increases (35).

The different tensile behavior between normal fiber-reinforced concrete and PVA fiber-reinforced was highlighted by the comparison of complementary energy from their bridging stress and crack open curve. It was concluded that PVA fiber features high interfacial chemical bond, frictional stress, and slip-hardening in a cementitious matrix. Moreover, the investigation on the effect of different fiber surface treatment composite performance revealed the importance of interface tailoring, with a higher oiling agent content that lowers the chemical bond interfacial friction, and surface abrasion, higher composite strain capacity and better performance consistency are obtained (36).

Another widely used fiber is polyethylene-based fiber. If this material has a density from 0.940 to 0.965 g/cm^3 it can be called high density polyethylene (HDPE). A study compared the behavior of three different types of SHCC subject to uniaxial impact tensile loading: the normal-strength matrix combined with PVA fiber, the normal-strength matrix with HDPE fiber, and a high-strength matrix with HDPE fiber. It was concluded that the strain rate sensitivity of the fiber-matrix interface depends strongly on the fiber type and matrix composition (41).

Less common fibers have also been studied as an option for SHCC, such a poly(p-phenylene-terephthalamide) (aramid), as-spun poly(pphenylene-2,6-benzobisoxazole)(PBO_AS) and high-modulus PBO fibers (PBO_HM). Research works that studied the tensile behavior of HS-SHCC made with these four fibers presented their properties (table 2.1).

Table 2.1: Physical and mechanical fiber proprieties (18).

	HDPE	**Aramid**	**PBO_AS**	**PBO_HM**
Diameter [a] [μm]	20	12	13	13
Density [g/m^3]	0.97	1.39	1.54	1.56
Tensile strength [Mpa]	2500	3400	5800	5800
Modulus of elasticity [Gpa]	80	74	180	270
Elongation at break [%]	3.5	4.5	3.5	2.5
Decomposing temp. [°C]	n.a.	500	650	650
Melting temp. [°C]	150	n.a.	n.a.	n.a.

n.a. - not available
[a] As measured with optical microscopy

These fibers were analyzed by scanning electron microscope (ESEM) and it was seen that they have different surface textures. The HDPE fibers have relatively deep longitudinal grooves along the entire fiber length. Both types of PBO fibers exhibit rather smooth surfaces, while the aramid fibers show a rough and non-uniform texture (figure 2.2) (18).

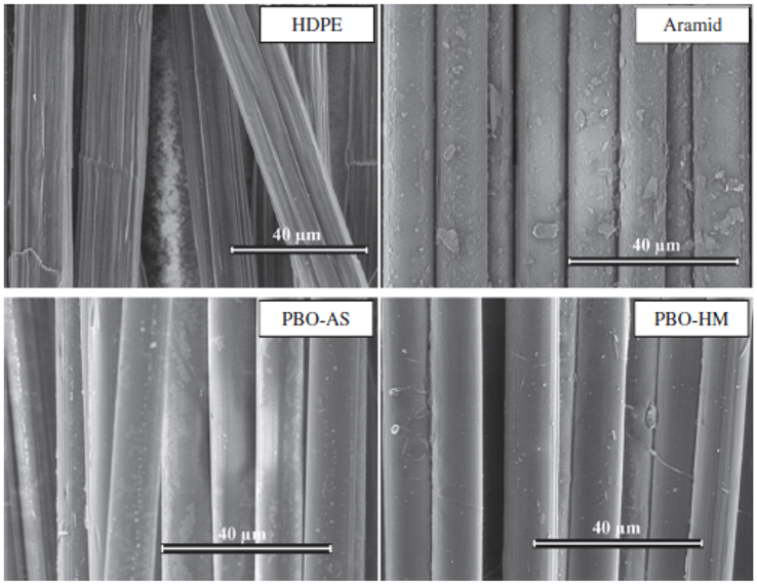

Figure 2.2: Surface textures of four types of polymeric fibers by scanning electron microscope (ESEM) (18).

The cementitious material reinforced only with steel fibers does not present a strain-hardening behavior (37), but this behavior can be achieved with the hybridization of steel and PVA fibers (34), for example.

2.1.2 Behavior of SHCC under different mechanical loads and environmental conditions

Since the properties of cementitious materials are related to the transport of water and aggressive chemical compounds, the study of their durability is essential. For SHCC this becomes more prominent, once their multi-crack formation cannot lead to significantly increased water or aggressive chemical compounds penetration. Therefore, the multi-cracks opening must be controlled to ensure the durability of the material.

In a preliminary research it was studied the durability of SHCC under mechanical, chemical, and thermal actions. It was concluded that a high ductility can be taken into consideration in service life design only if the structure is to be placed in an aggressive environment, such as marine environment (38). A subsequent research that analyzed the durability for the same actions showed that evidence has been presented that crack control is maintained up to large strain levels but is not proved to what extent this crack control is valid for different loading histories and paths (1).

Some research studied a way to reduce the penetration of fluid into the material. A study used neutron radiography to analyze water penetration in a neat SHCC and a SHCC produced by adding a silane-based water repellent agent. They concluded that if SHCC is made with water repellent, an efficient barrier against water penetration is built up and thus could consider a material ductile and durable (39).

The SHCC was already studied under cyclic loads since a deep knowledge of the fatigue behavior is indispensable for a safe and economical design of structural members, as well as for building elements for which such materials might be used. It was revealed that the hysteresis analysis of the stress–strain curves showed that the material stiffness decreases with an increasing number of loading cycles and a considerable partial inelastic deformation takes place in every cycle (31). Also, in another work, it was concluded that the repeated loading caused a decrease in the tensile strength of SHCC compared with the results from the monotonic tests (40).

The building of new structures with enhanced impact resistance is possible using SHCC, making this study of great importance. It has already been confirmed that in dynamic loading SHCC shows superior performance with regard to fracture energy when compared to conventional, high-performance

or ultra-high-performance concrete with or without fibers (2). A recent study compared two fiber materials and concluded that the first-crack strength of SHCC under impact loading depends not only on tensile strength and the strain rate sensitivity of the constitutive cementitious matrix, but also on the strength and strain rate sensitivity of the fiber-matrix interface (41).

Also motivated by the potential of SHCC in application for structural durability, studies of pure shear behavior were done. The shear strength of the cementitious composites was 50% higher than the ultimate strength obtained in the direct tension tests (42). Other study showed that the shear response of SHCCs is characterized by three phases: a linear first phase; followed by a shear hardening phase, where the formation of multiple microcracks is observed; and then a shear softening stage occurs, which is characterized by the formation of macrocracks (43). For a typical behavior when the material is subjected to tensile loading, see Figure 2.1.

It has been shown that the application of a SHCC layer to strengthen the tensile side of a plain concrete beam increased both load carrying capacity and ductility of beam under bending loading (44). Likewise in the case of shear strength, which the enhance durability of structural concrete was proved through the high ductility of the material in diagonal tension, or shear (42).

The temperature effect in SHCC has already been investigated for three different strain rates. In that study uniaxial tension tests with in-situ temperature control were performed at 22°C, 60°C, 100°C, 150°C. The experiment showed that the strain capacity increases with decreasing strain rate at temperatures of 22°C and 60°C, but for the temperature of 100°C this material property increases when the strain rate increases. At 150°C the investigated SHCC loses its ductility and no noticeable strain rate effect can be observed (19).

Many SHCC research works are focused on the use of this material for repair of concrete structures. The high ductility and strain capacity of SHCC give this material high potential for use in applications in which high, non-elastic deformability is needed, some of the most promising applications are structural repair and strengthening of existing structures (13) (45).

However, the SHCC behavior is linked with several possible variations in the material composition, such as the matrix mix composition or the type of fibers used, as shown in the previous subsection.

2.2 Micro-computed tomography (microCT) technique

MicroCT is a non-destructive technique that allows the investigation of the internal structure of a sample by creating three-dimensional images. The basic principle of microCT is a source emitting x-ray onto a sample, this x-ray is attenuated as it passes through the sample and then detected by a detector. This is done while the specimen holder rotates 360° about a single axis at a certain step, generating a sequence of projection images. The projection images are reconstructed using mathematical principles of tomography, finally providing a sequence of 2D slices that compose the 3D image (46). See in Figure 2.3 a schematic illustration of x-ray microCT acquisition and reconstruction processes.

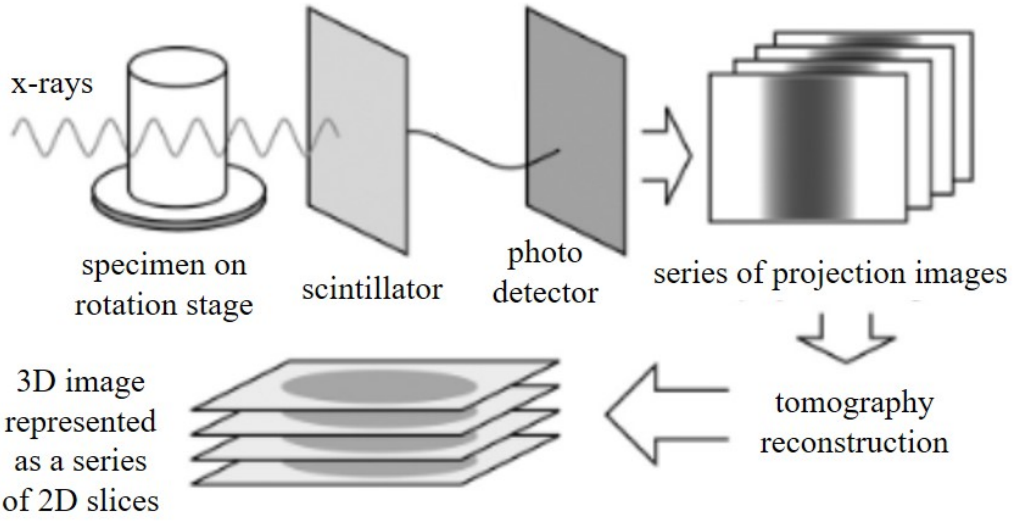

Figure 2.3: Schematic illustration of X-ray microCT acquisition and reconstruction processes (46).

Each internal phase of the material is distinguished in the image according to its x-ray attenuation coefficient. The x-ray attenuation coefficient is related to the atomic number (Z) and mass density of the chemical element or mixture of elements in the materials' phase. In general, for a fixed x-ray energy, lower-Z elements absorb less than higher-Z elements. Thus, the different phases, with different atomic numbers and density, will appear with different gray levels in the reconstructed image. Conventionally, higher-Z and density phases show up brighter and lower-Z and density phases show up darker.

From the image obtained, the qualitative and quantitative study of these is supported by the field known as digital image processing and analysis.

2.2.1
Digital image processing and analysis

To obtain data of the material's microstructure a standard procedure is usually followed, which begins with the acquisition of the image by some microscopy technique, see the flowchart in Figure 2.4. Succeeding image acquisition, by microCT in the research at hand, the process can be divided into two major steps known as digital image processing and digital image analysis.

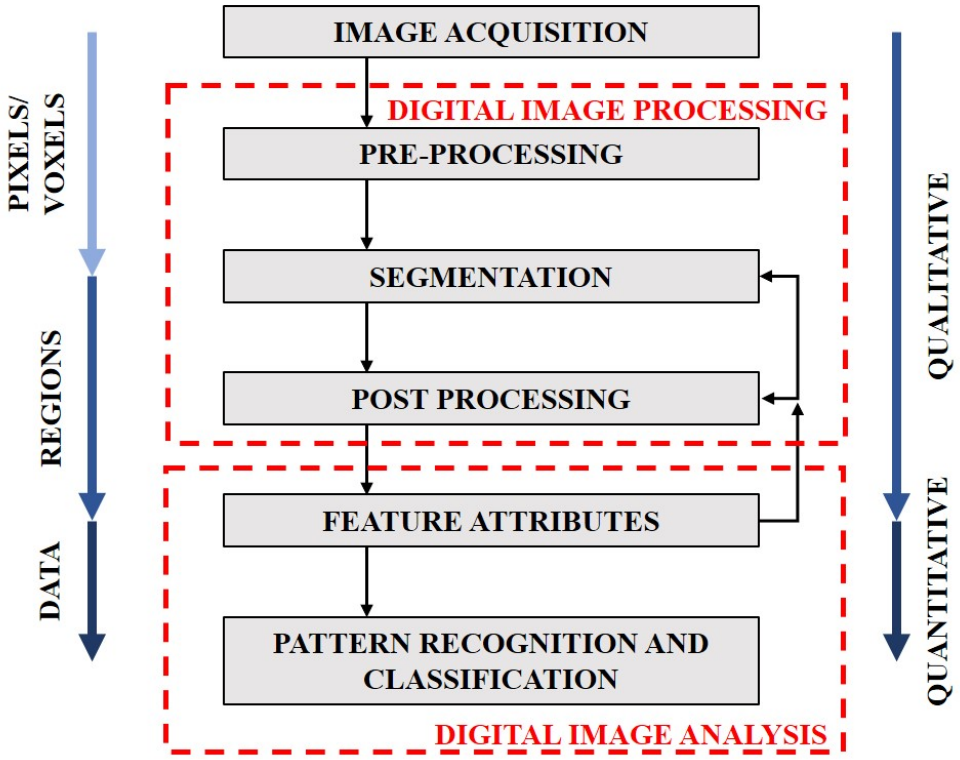

Figure 2.4: Standard digital image processing and analysis sequence. Adapted from (47).

The digital image processing step can comprise three steps: pre-processing, segmentation and post-processing. The pre-processing has the role of adapting the image for a better visualization (qualitative) and/or to reduce the errors of quantitative data that will be obtained in the following steps. A classic example of pre-processing are the filters for noise reduction. Image noise appears as pixels/voxels that do not match the surrounding region, which may compromise the segmentation step. Properly pre-processed, the image moves on to the segmentation step. At this point, the processes are no longer performed on each pixel/voxel and but rather on groups of adjacent pixels, called regions of interest (ROIs). Contextualizing this thesis, there are three ROI

corresponding to three constituent phases of SHCC: pores, fibers and fine aggregates. Once segmented, a post-processing step can be performed to correct the ROIs, eliminating spurious pixels and/or objects. For instance, objects can be eliminate by volume or aspect ratio. This step can be repeated after the feature extraction until reaching a satisfactory result.

In the digital image analysis step quantitative data are obtained and can be subdivided in two steps: the feature extraction and the pattern recognition/classification. In the extraction of features, sets of pixels/voxels connected within the ROI can be understood as objects, and features such as volume and aspect ratio can be measured for each object. Then, with the information of one or more features, the objects can be classified and/ or a pattern of the features can be determined.

An image histogram is a graphical representation of the tonal distribution in a digital image, which plots the number of pixels/voxels for each tonal value. The same phase in the material will be represented by pixels/voxels of similar gray levels, and this will appear as a peak in the image histogram. The standard method of segmentation is known as a thresholding, which distinguishes an ROI by choosing a range in the image histogram that contains the peak corresponding to a given phase. Thus, when the peaks are not well defined for each phase that constitutes the material, the thresholding method may not be efficient, requiring the search for alternative methods.

The segmentation can be considered a critical step since some images present difficulties to distinguish internal regions and that may lead to inaccurate data. As mentioned, the microCT technique generates gray levels according to the microstructural phase density. Therefore, if there are two or more phases with similar density in the material, that will generate voxels with similar gray levels for these different phases in the image. This will result in an image histogram of the voxel gray levels in which there will be no defined peaks for each phase.

In this context, the use of machine learning as a method for image segmentation has been strongly explored. The main difference between the two segmentation methods is that by thresholding the tone of the separate pixels/voxels is the only parameter used, while the machine learning takes into account the various attributes of groups of pixels, such as the shape and configuration of their tones. In this way, this method can solve the trouble of images that present overlapping peaks for two or more phases.

2.2.2 Machine learning applied to image segmentation

All studies about analysis of 3D images of cement-based composites presented so far used the thresholding method for segmentation of the phases. As mentioned before, this is not suitable to the complex microstructure of SHCC. In this context Deep Learning (DL) appears as a solution for this task.

Among several architectures of a DL network, the Convolutional Neural Network (CNN) is one that has been widely applied to image segmentation. CNNs already demonstrated excellent performance at tasks such as handwritten zip code digit classification (48) and face detection (49). In recent years, several works have shown that they can also be applied to more challenging visual classification tasks (50), such as in materials with complex microstructures (9) (23)(26)(51)(52)(53)(54)(55)(56).

In DL, multiple levels of representation are obtained by composing non-linear modules that transform the representation at one level into a representation at a higher, slightly more abstract level. For classification tasks, higher layers of representation amplify aspects of the input that are important for discrimination and suppress irrelevant variations (57). The networks require as input a training set, defined by the user upon the images. The network is trained until its outputs match the desired object classes, within a certain error criterion. The trained network can be checked for accuracy upon a set of reference images and is then ready to be applied to other images.

Research that used artificial neural network for segmentation of radiographic images was able to identify and quantify the damaged areas caused by drilling in composite materials. The authors justified the use of this segmentation technique saying that it is easy to use, efficient, accurate and robust to noise, common in radiographic images (52).

Neural networks also presented good results in the classification of internal damage in steels working in creep conditions. The damage was classified according to a database of standard images with the development phases of the damage processes. The advantage of using neural network for this task is that the accuracy of the traditional method vastly depends on the place chosen to take the metallographic structure, the proper interpretation of observed metallographic structure and the need of engagement of experts with sufficient practical knowledge. A computer assisted method reduces the human factor and allows an objective assessment of the material's structure (54).

2.2.3 In-situ microCT

The ability to perform mechanical tests or promote other kind of interaction with the specimen during tomographic image acquisition is known as in-situ microCT. This means that for the same specimen it is possible to obtain a sequence of 3D images at different stages of mechanical loading. The advantage of this technique is that it can monitor the failure patterns of materials during the mechanical test until failure.

In-situ microCT is not a common technique to analyze the SHCC nowadays, but has already been widely used for cement materials in general, mainly to characterize the fracture evolution when they are under progressive compressive loading (58)(59).

In-situ microCT images were also used to characterize microstructure and internal damage in cement-based materials and then related to bulk splitting strength and fracture energy (60). This energy was measured using a first principles approach in which the bulk energy dissipated by fracture was normalized by the surface area created, which was evaluated in such a way that roughness, branching, and fragmentation could all be directly measured. Results showed that, for the specimens tested, aggregate surface roughness had little effect on strength but significant effect on fracture energy. So, 3D images allowed to explicitly represent microstructural features into computational models for material performance (60).

Even without the use of instrumentation during the test, the displacement can be measured by DVC. A study used a sequence of 3D microCT images to obtain the elastic modulus of concrete by DVC (59). In order to compare the elastic modulus, the first image (before any load) was used as input for finite element (FE) models. For this, the threshold-based segmentation separated the concrete into three distinct phases: aggregates, voids and paste. The results showed that microCT-image based FE models were successful, since the elastic modulus obtained was 24.2 GPa, which is close to the experimentally obtained 26.42 ± 3.20 GPa. This research proved that the combined use of advanced techniques as in-situ microCT, DVC and image-based modeling, offers highly-accurate, complementary functionalities for both qualitative understanding of complex 3D damage and fracture evolution and quantitative evaluation of elastic properties of multi-phasic composite materials such as concrete (59).

2.2.4
Digital volume correlation (DVC)

DVC is a technique that estimates full-field displacement and strain in 3D over the entire volume of the specimen by correlating imaging sub-volumes of the specimen in different loading states (6). DVC can be applied if there are at least two images presenting a change in micro or mesostructure. It is based on three main steps: acquisition of 3D images; pattern-matching correlation procedure to measure a displacement vector field; calculation of the strain field from the measured displacements (61)(62).

3D image acquisition needs to be non-destructive since it must not influence the mechanical test. So, in-situ microCT fits perfectly in DVC context. DVC can also be applied to images acquired in an ex-situ setup, but as in in-situ experiments the specimen is not removed from the specimen holder, results can be more accurate.

With the sequence of images of the material at different loading stages, the local displacement can be measured. For it, the user must determine a sub-volume in the non-deformed image and the code will search in the deformed image for the same sub-volume through pattern-matching correlation. This sub-volume will move across the 3D image at a step also set by the user. The result will then be vectors that start at the center of the sub-volume in the non-deformed image and end at the center of the sub-volume of the deformed image. These displacement vectors are then used to calculate the strain field, according to the size of the defined sub-volume.

DVC has already been used to investigate distinct types of materials (63)(64)(65)(66)(58). With the relevance of these results in scientific research of materials, DVC has gained ground as a strain mapping method of materials. Therefore, several codes and software have been developed and improved to support this demand (63)(67).

2.3
SHCC analyzed by microCT

Until recently, microCT has been used as a complementary technique in SHCC research. For example, in the study that investigated the mechanical behavior of SHCC under impact loading, microCT was performed in some specimens that were subjected to highly dynamic spall experiments using a

Hopkinson bar spall, see Figure 2.5. This result was analyzed qualitatively and showed that the cracks that were observed on the lateral surface also appear inside the material and the center of the concentric circular cracks are located along the longitudinal axis of the specimen (2).

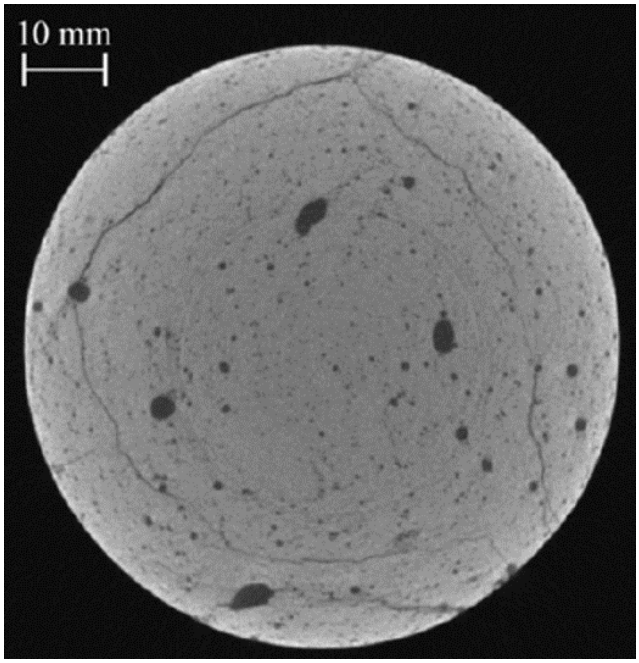

Figure 2.5: MicroCT image of a specimen submitted to a spall experiment (2)

In another study microCT was used for monitoring rust formation during accelerated corrosion of SHCC reinforcement, and subsequent cover cracking. A quantitative analysis was performed by four-phase segmentation. A manual thresholding was applied for determination of the boundaries between these phases: air voids and cracks, cementitious material, corrosion products, and non-corroded steel (Figure 2.6). They are displayed as white, black, red, and blue, respectively, in Figure 2.7.

MicroCT images were acquired during accelerated exposure to corrosion. A single vertical slice was selected to monitor this exposure, and from the first scan after the reference (second image in Figure 2.7) several cracks were clearly visible. Subsequent scans showed the formation of new cracks, without the formation of a single major crack. The rust layer around the steel bar had a relatively uniform thickness, with the exception of the contact with the large air void. These scans also suggest that the corrosion products penetrate into the air void, thereby relieving some of the pressure which would otherwise be exerted onto the surrounding material (68).

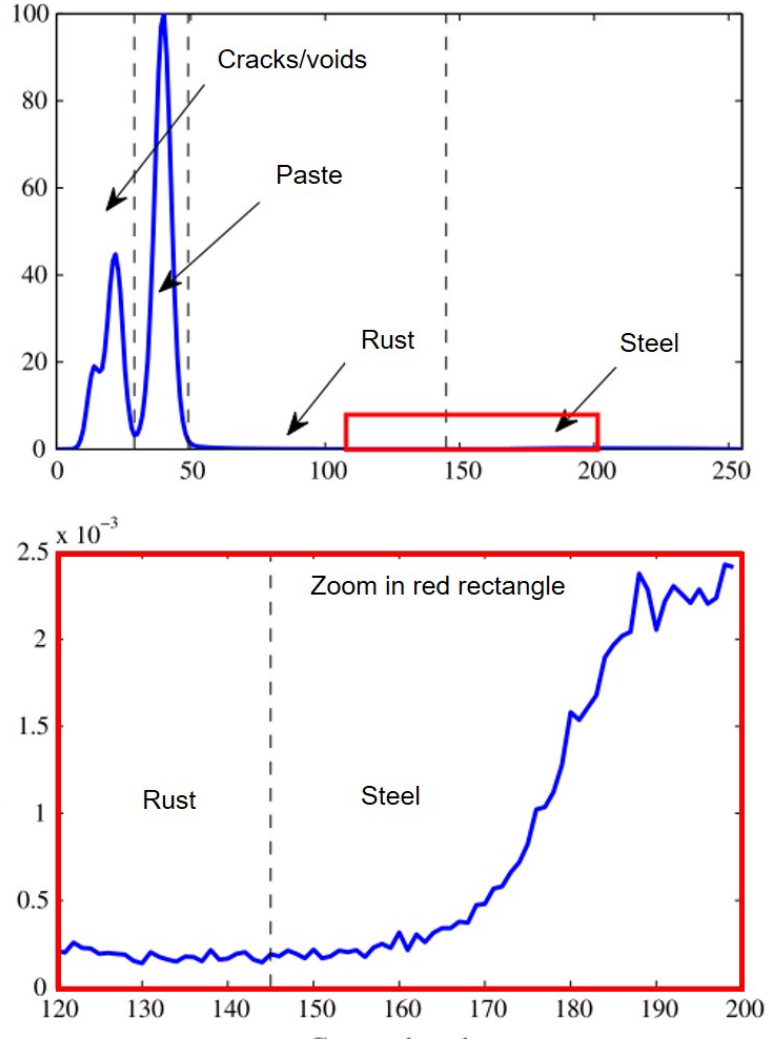

Figure 2.6: 3D image histogram of SHCC reinforced by carbon steel rod. Dashed lines indicate the threshold for segmentation of each phase (68).

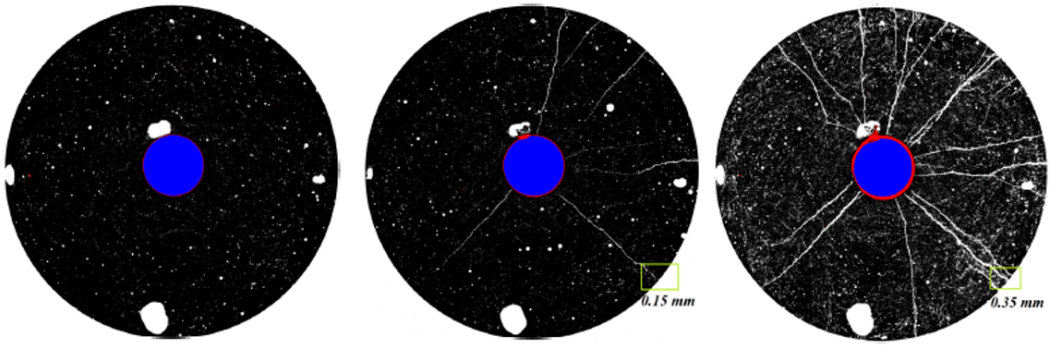

Figure 2.7: Monitoring of the SHCC corrosion process by segmented microCT images sequence (68).

In this work the voxel size was about 16 μm and in the histogram (Figure 2.6) it is possible to see that there is no peak that differentiates the fibers from the cement paste. So, in the image what they call paste, would be paste with fibers. This happens because of the small difference in density between these materials, requiring a higher resolution to maybe differentiate them in an image by thresholding.

From the works available in the literature only steel fibers could be distinguished from the cementitious matrix by intensity thresholding, since steel and cementitious material have enough density difference. Also, steel fibers commonly have larger sections and lengths than other fibers such as PVA and PE, making it easier to identify them for the same resolution. A study analyzed microstructural characteristics of hybrid (steel and PVA) fiber reinforced concrete through microCT images and correlated it with their mechanical properties (69). In this study only steel fibers were segmented, see Figure 2.8. Also note that the voxel size of 0.1 mm x 0.1 mm x 0.5 mm did not allow the visual distinction of the PVA fibers in the cementitious matrix.

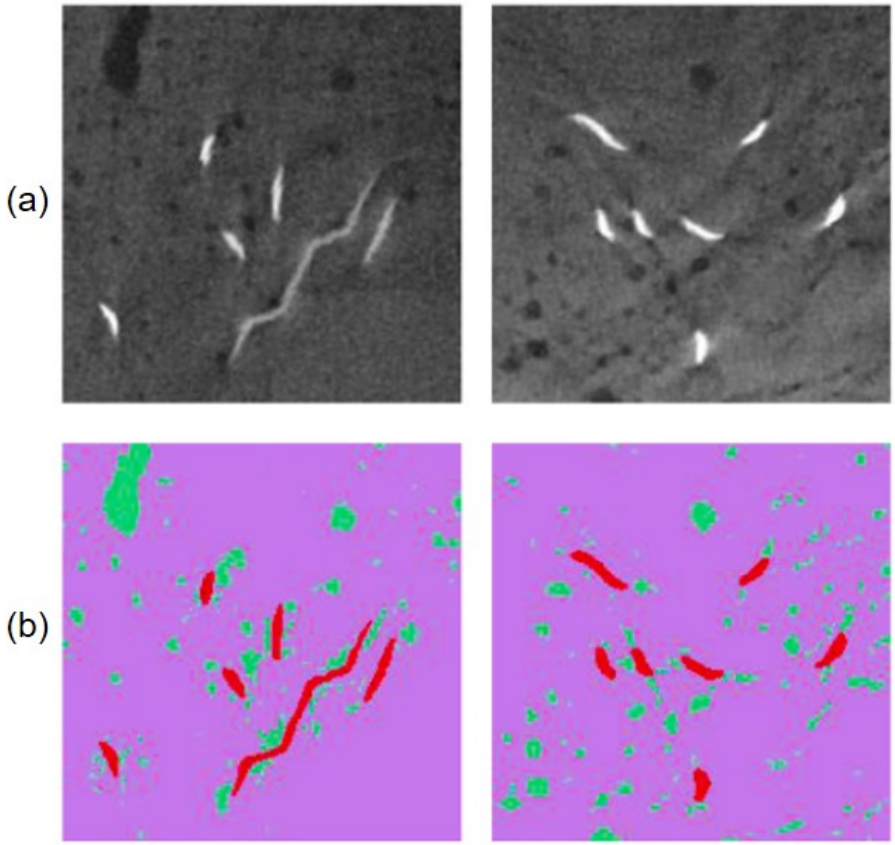

Figure 2.8: (a) 2D slices microCT image of steel-PVA fiber reinforced concrete; (b) segmented image (purple: matrix, green: pores, red: steel fibers) (69).

Until recently, fibers such as PVA and PE inside a cementitious matrix could not be analyzed quantitatively due to the limitations of segmentation techniques. Machine learning applied to image segmentation can be a solution to such limitation and this is one of the key points of this thesis.

3
The use of X-ray microtomography for microstructural characterization of PVA-steel fiber reinforced strain hardening cementitious composites

The mechanical behavior of SHCC is highly related to its micromechanical response and can be improved by fine-tuning its microstructure. Thus, the study of each constituent phase and the interaction between them is essential. Although the studies demonstrate the positive effect of hybridization of the SHCC, little is known about microstructural changes when steel fibers are introduced to replace part of the PVA. In order to obtain information regarding the material microstructure, imaging techniques are required. In this context, micro-computed tomography (microCT) appears as an efficient technique for 3D analysis of material microstructure (7)(21)(70) and internal damage (20)(71)(58). The resolution of the images obtained from this technique are typically on a meso scale and dependent on the diameter of the scanned specimen (72). Regarding SHCC microstructure, PVA fiber tiny size imposes the need of a suitable resolution for its 3D representation. Conversely, constituent phases such as macro pores and steel fibers can be readily discriminated with resolutions reached in specimens' sizes typical of laboratory tests (73)(74)(75)(76). It is also facilitated by the great difference in average density and atomic number of these phases chemical composition, resulting in different X-ray absorptions. The high density and atomic number of the steel fibers as compared to the surrounding cementitious matrix gives rise to distinct bright volumes. On the other hand, the air voids result in darker regions when compared to the matrix. In this way, the orientation of the steel fibers has already been analyzed in specimens of steel fiber reinforced concrete and has been correlated with behaviors such as post-cracking (77) or tensile response (78).

3.1
SHCC Composition and Mixing Protocol

This research investigated a normal-strength matrix reinforced with PVA and steel fibers. As dry materials, a high-early strength cement type CPV-ARI from LafargeHolcim and a fly ash from Pozofly were used. According to the

suppliers, they have densities of 3120 kg/m^3 and 2350 kg/m^3, respectively. A quartz river sand with particle sizes ranging from 75 to 212 μm and 2700 kg/m^3 density, was used as fine aggregate. A superplasticizer (Glenium 51) and a viscosity modifying agent (Mastermatrix UW410), both supplied by BASF, were used to adjust the rheological properties of the composites. Regarding the fiber reinforcement, a constant volume fraction of 2.0% was adopted. Hybrid compositions were produced by replacing PVA by steel fibers in 25%, 50%, 75% and 100% fractions. The PVA fibers used in this study were produced by Kuraray Co. They have a diameter of 40 μm, a cut length of 12 mm and a density of 1260 kg/m^3. The steel fibers were supplied by Ganzhou Daye. The fibers have a diameter of 120 μm, a cut length of 13 mm and a density of 7850 kg/m^3. Table 3.1 presents the nomenclature of the investigated SHCC with their respective compositions. The SHCC mixtures were prepared using a 5 L planetary mixer. First, cement, fly ash and fine aggregate were mixed for 1 min. Next, superplasticizer and water were added for 1 min. Then, the materials were mixed for 5 min until they reached the desired rheology. The polymeric and steel fibers were added to the matrix during the following 2 min. After the mixing procedure, the materials were placed into the molds and cured until they reached appropriate strength. The specimens were molded in the horizontal direction to prevent fiber segregation. After 24 h, the specimens were demolded and stored under constant temperature (21°C) and humidity (65%) for 14 days, before testing.

Table 3.1: Mixture composition of SHCC under investigation (kg/m^3).

Mix	**Cement**	**Fly Ash**	**Quartz Sand**	**Water**	**VMA***	**SP***	**Fiber Volume Fraction (%)**	
							PVA	**Steel**
P2.0	505	621	536	336	1.2	11.7	2.0	-
P1.5S0.5	505	621	536	336	1.2	11.7	1.5	0.5
P1.0S1.0	505	621	536	336	1.2	11.7	1.0	1.0
P0.5S1.5	505	621	536	336	1.2	11.7	0.5	1.5
S2.0	505	621	536	336	1.2	11.7	-	2.0

*VMA: viscosity modifying agent; SP: superplasticizer Glenium 51.

3.2 MicroCT and image processing

The microCT scanning and image processing protocol were performed in a Zeiss-Xradia 510 Versa. All specimens were imaged prior to shear testing, totaling ten microCT scans. Taking into consideration the analysis' region of interest and the desired resolution, the height of the scans was approximately 40 mm. Figure 3.1 (a) shows a specimen placed in the microCT test position highlighting the approximate scanned region of interest (ROI). The scans were approximately 2-hours long and the conditions were 140 kV voltage, 10 W power, 0.4X macro lens, 1601 projections images at 1-second exposure time. The reconstruction was done using the filtered back projection method and generated 3D images with a voxel volume of $(18.5\ \mu m)^3$.

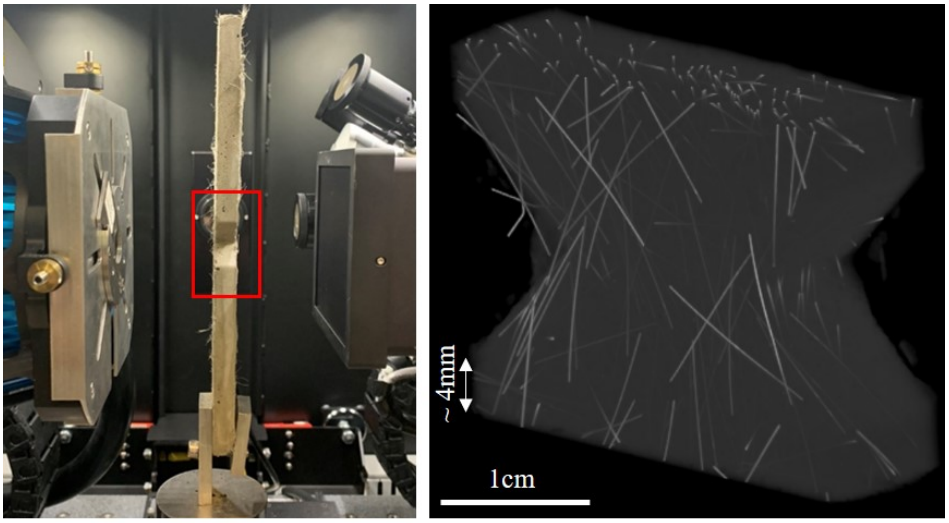

Figure 3.1: (a) SHCC specimen placed between X-ray source and detector, highlighting in red the scanned region and (b) X-ray scanned volume after cropping.

A systematic image processing workflow protocol was followed for all ten 3D images obtained. First, all images were carefully cropped to eliminate external regions and darker parts caused by the X-ray cone effect. After cropping, the ROI was set to approximately 4 mm above and below the notch, as shown in Figure 3.1 (b) for P1.0S1.0 scanned specimen. Then, the edge-preserving non-local means low-pass filter (79) available as a FIJI plugin (80), was applied in order to reduce image noise. Pores and steel fibers were segmented using the thresholding method. Thresholding segmentation is done by setting a range of gray shades in the image histogram for each phase of

interest. The pores and the background represent the darkest area of the image since it is the least dense part of the investigated specimen, the air. This means that in the image histogram, pores and the background are represented by the same tonal range. Thus, to discriminate the pores from the background, the matrix and steel fibers were initially segmented, the internal pores were filled, and then the pores were obtained by subtracting the 2 images (7). On the other hand, the good contrast between the steel fibers and the matrix allowed for direct thresholding segmentation.

The pores were studied in two different complementary steps. The first was intended to correlate porosity with the mixture composition of SHCC. In this step, segmented objects up to three voxels and/or with sphericity less than 0.3 were eliminated, since these objects do not correspond to pores, often resulting from segmentation problems at the edges. Sphericity is a function of the volume and of the surface area, in which spherical pores have sphericity close to 1 (7). From this segmentation the 3D porosity was determined and to verify the porosity distribution along the specimen, the 2D porosity of some axial slices were plotted. Once the crack patterns are influenced by the pores structure (81), the second step aimed to verify the influence of the largest pores on the fracture of the material. In this case, only pores with equivalent diameter > 1 mm were considered, and their position was compared with the 2D position of the cracks obtained by the DIC test in order to check possible crack nucleation or propagation trend points. All hybrid specimens had their pores larger than 1 mm plotted in 3D. The x and z axes were indicated for comparison with the images obtained from DIC. A separate scale was set for pores above 3 mm, avoiding concentration of pores of the same color on the scale.

Fiber orientation study was performed only on steel fibers. As the specimens are larger due to the shear test configuration, the achieved resolution is not enough to distinguish the PVA fibers. Moreover, the very bright steel fibers lead to a compression of the dynamic range in the dark range of the other phases (matrix, pores, PVA fibers), thus decreasing the contrast between them. Two steps were performed for the steel fibers: quantification of fiber dispersion and orientation. As the fiber content was set in the mixture composition and the scanned volume was around the notch, the fiber content obtained by image analysis should indicate whether there is a concentration of fibers near the notch. In the present work the fibers were mixed randomly, so two angles should be studied, phi (ϕ) and theta (θ), as shown in Figure 3.2. The z-axis is longitudinal to the specimen and the y-axis is the width of the specimen. The

orientation measurements were carried out with software Dragonfly (Object Research Systems, Montreal, Canada).

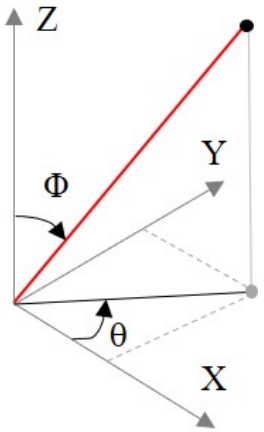

Figure 3.2: Phi (ϕ) and theta (θ) angle – schematic representation.

As the steel fibers have a diameter of 120 μm and the pixel size of an image section is 18.5 μm, this means that around six pixels define the steel fiber section diameter. To ensure that two or more fibers analyzed are not connected, a morphological operation of erosion was performed on large volume segmented objects. Thereunto, a systematic procedure was carried out: objects with a volume greater than 0.35 mm^3 were separated and erosion was applied to them. If fibers were still connected in the same object, the procedure was repeated. A meaningful number of pixels representing the fiber allowed that erosion was executed without eliminating the fibers, but only slightly shrinking and thinning them. Next, the analysis was done through the frequency distribution, such that the phi angle showed the relative frequency of each value within a bin range of 5°, starting at 0° and ending in 90°, and theta angle showed the percentage frequency of each value within a bin range of 5°, starting at 0° and ending in 180°.

3.3
3D images processing and analysis results

Table 3.2 shows the results obtained in the microCT analysis for each specimen tested. It presents the values obtained for the pore volume (mm^3), the steel fiber volume (mm^3), the entire analyzed volume (mm^3), the porosity (%) and the steel fiber content (%). From the results, it is possible to see that the porosity is greater the higher the percentage of steel fibers instead of

PVA fibers. Figure 3.3 shows the porosity along the ROI of specimens P2.0_1, P1.0S1.0_1 and S2.0_1. This result presented a random distribution, without a preferential position for pore concentration.

Table 3.2: Porosity and Steel fiber Content (%).

Mix	**Pore volume (mm^3)**	**Steel fiber volume (mm^3)**	**Analyzed volume (mm^3)**	**Porosity (%)**	**Steel fiber Content (%)**
P2.0_1	403.7	-	7446.3	5.4	-
P2.0_2	333.8	-	8039.2	4.2	-
P1.5S0.5_1	188.8	64.9	7711.3	2.4	0.8
P1.5S0.5_2	258.8	47.3	7139.5	3.6	0.6
P1.0S1.0_1	248.8	107.9	7819.9	3.2	1.4
P1.0S1.0_2	274.7	118.3	7334.4	3.7	1.6
P0.5S1.5_1	171.0	151.5	6495.9	2.6	2.3
P0.5S1.5_2	206.4	194.8	7454.6	2.8	2.6
S2.0_1	120.8	217.1	7696.6	1.6	2.8
S2.0_2	127.6	213.5	7861.8	1.6	2.7

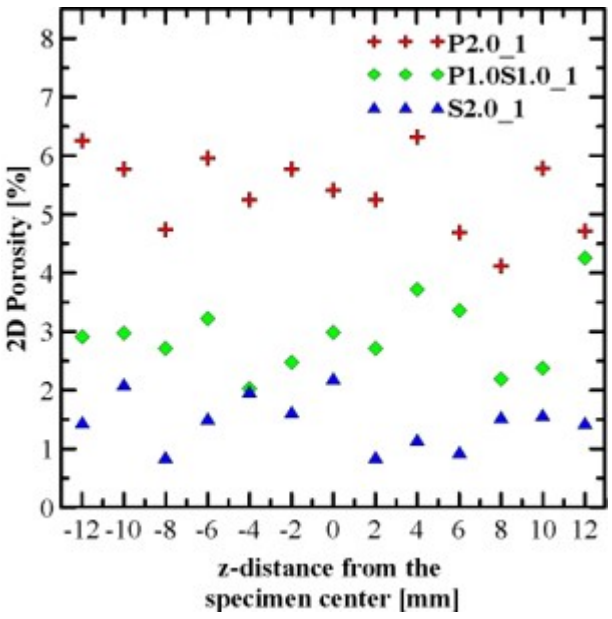

Figure 3.3: 2D porosity measured from 12 mm top to 12 mm bottom slices at 2 mm spacing.

By comparing the specimens P2.0_1 and S2.0_1, produced with 2.0% of PVA and steel fibers, respectively, the porosity decreases from 5.4% to 1.6%, a reduction of a factor greater than 3. Figure 3.4 shows the pore distribution

randomly colored of the mentioned specimens. The differences between the composites can be observed. Only the P1.5S0.5_1 (2.4%) specimen did not follow the porosity trend, which does not invalidate the conclusion since the porosity is affected by the material preparation.

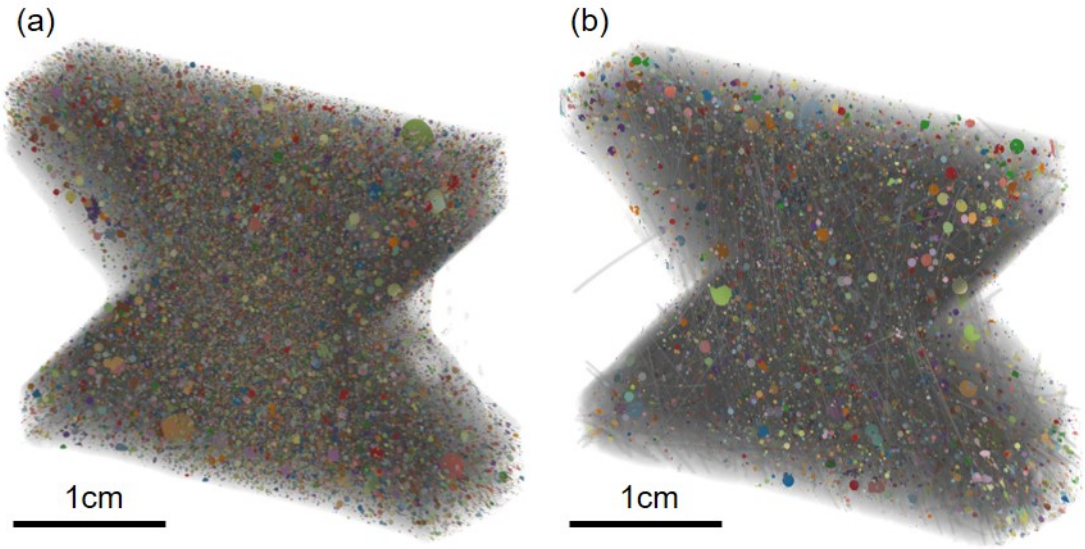

Figure 3.4: 3D representation of the segmented pores of the specimens (a) P2.0_1 and (b) S2.0_1.

Figure 3.5 shows the 3D representation of pores larger than 1 mm in diameter and the steel fibers distributed in each hybrid specimen studied. The three largest pores in the hybrid specimens were separated on a cyan color scale. The equivalent diameters of these pores are 3.0, 3.5 and 4.3, in the specimens P0.5S1.5_2, P1.5S0.5_1 and P1.5S0.5_2, respectively. No pertinent relation between the position of the macropores and the crack pattern was found.

This result was expected since the PVA fibers are smaller particles scattered in the matrix and for the same fiber contents (%) there is a meaningful greater number of fibers, being more conducive to the formation of voids. According to (82)(82), the use of micro polymeric fibers may increase the number of internal microdefects, which can affect both the multiple cracking behavior and the tensile strength of the composites. The results obtained in the present research confirm that PVA fibers increase the pore volume.

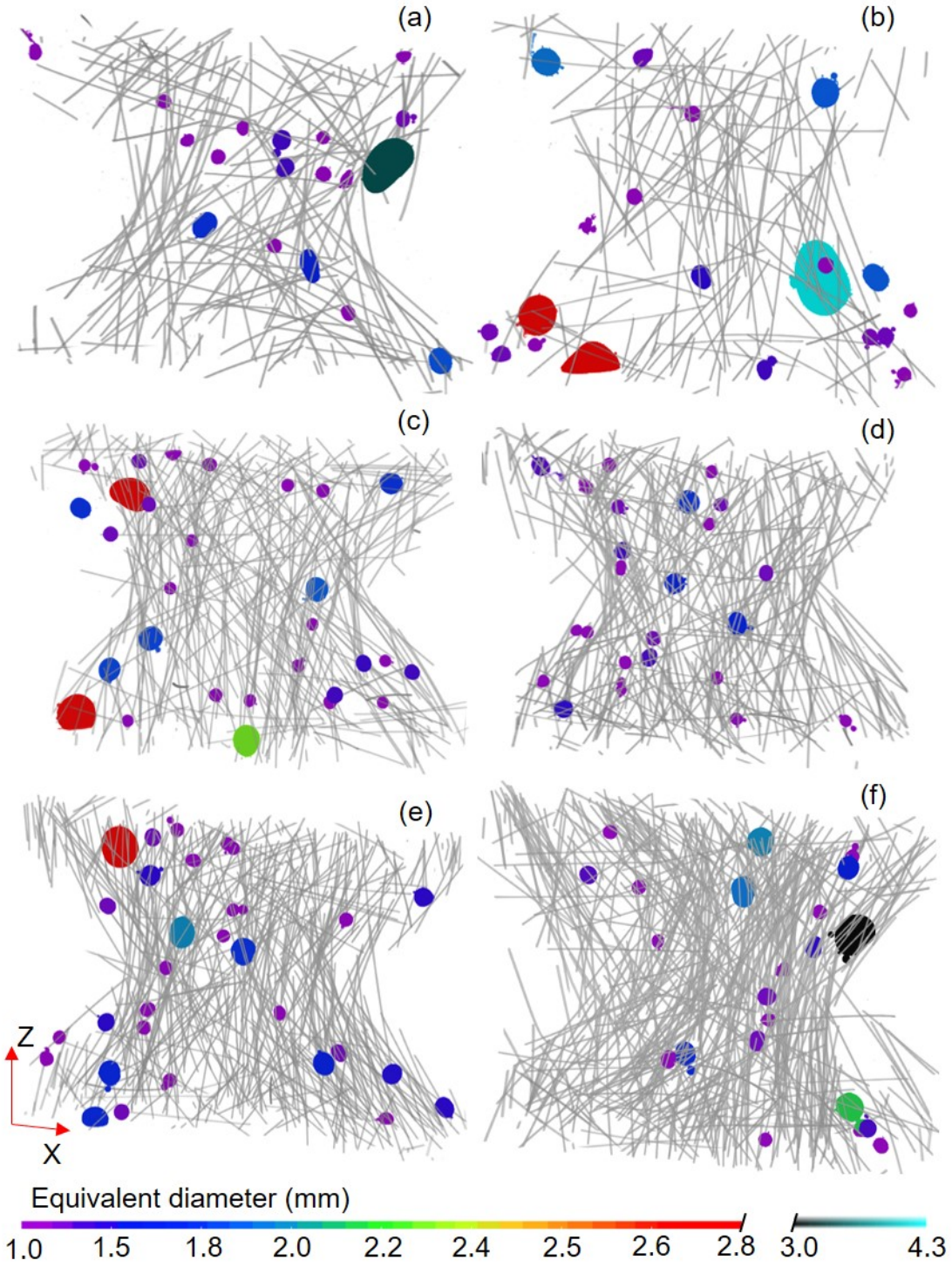

Figure 3.5: 3D pores larger than 1mm equivalent diameter in the hybrid specimens: (a) P1.5S0.5_1; (b) P1.5S0.5_2; (c) P1.0S1.0_1; (d) P1.0S1.0_2; (e) P0.5S1.5_1; (f) P0.5S1.5_2.

Table 3.2 also shows that the steel fiber content in the volume around the notch, obtained by image processing, is at least 20% greater than the steel fiber content inserted in the mixture, in some cases reaching more than 70%. The

steel fiber content obtained for the specimen S2.0_1 is 2.8%, for example, while the theoretical volume fraction is only 2.0%. The result obtained represents a 40% higher fiber volume fraction. For the hybrid specimen P0.5S1.5_2, a 73% higher fiber volume fraction was observed. The results may be associated to the reduced dimensions of the notch region (9.5 mm thickness and 18 mm width), which may affect the steel fiber distribution along the specimen. The results confirm the tendency of particle concentration in the cementitious matrix when a tapering in the structure occurs. In this sense, larger specimen's dimensions should be adopted in order to reduce the fiber concentration in the notch region, which can affect the test results.

Regarding the orientation of the fibers, the qualitative interpretation of the images in Figure 3.5 showed that they seem to be randomly distributed. On the other hand, the distribution of Figure 3.6 (a) presents a slight tendency for the steel fibers to be more axially oriented (Phi = 0°) the higher the percentage contents of steel fibers. As the PVA fiber content increases, however, the orientation of Phi angles tends to be higher. This corroborates with the recent study results on steel fiber orientation in steel-PVA fiber reinforced concrete (84). The results show that the percentage content of each type of fiber can influence their orientation and distribution in the cementitious matrix.

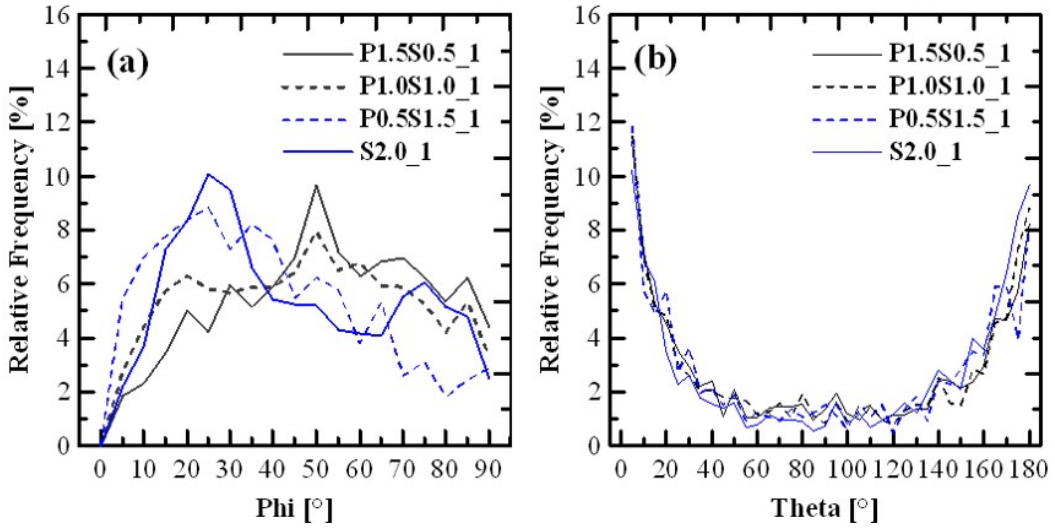

Figure 3.6: Phi (a) and theta (b) angle distribution as quantification of fiber orientation.

The orientation related to the theta angle shows a remarkable pattern, regardless of the steel fiber content, see Figure 3.6 (b). Theta is the angle from the X-axis of the fiber projection on the XY plane, and the distribution results showed that theta angle is preferably 0° or 180°. This means that the fiber

projection tends to be aligned with the larger side of the cross-section of the specimen. The results obtained can be explained by the tiny thickness of the specimen (9.5 mm), which tend to induce a 2D distribution of the fibers. In (84) study, the theta angle distribution was random, since the geometry of the specimen analyzed has a square cross-section.

3.4 Conclusions

The pore analysis showed that specimens made with PVA fibers have a likely tendency to higher porosity than those made with steel fibers. This result can be understood as the smaller particles dispersed in the matrix are conducive to the formation of pores. This justifies the increase in strength obtained in direct tensile tests when steel fibers are introduced to replace smaller fibers (82). Also, it may contribute to the gain in strain hardening behavior for higher percentages of PVA, since the higher number of pores may facilitate the formation of multiple fine cracks. On the other hand, the porosity influence was not observed in the shear response, in which the steel fibers specimens presented lower maximum shear stresses than hybrids and PVA fibers specimens.

It was also found that the largest pores do not affect the formation and propagation of cracks for this mechanical test configuration. Stating that the weaker zone for starting cracks is the notch.

The steel fiber content (%) around the notch obtained by image analysis seems to be evidence that there is a concentration of steel fibers in the notch, probably due to the taper during molding of the specimen. The fiber orientation in theta (θ) angle is controlled by the tiny thickness (9.5 mm) of the specimen. However, the fiber orientation in phi (ϕ) angle showed a pattern when the fibers are randomly mixed. The fiber orientation showed a pattern when the fibers are randomly mixed. A slight tendency towards axial orientation was observed when increasing the PVA replacement amount by steel fibers. However, it was not enough to impact the mechanical behavior of the material. For this purpose, at least further research including change in orientation during the manufacture process of the specimens is suggested.

4
Semantic segmentation of the micro-structure of strain-hardening cement-based composites (SHCC) by applying deep learning on micro-computed tomography scans

Renata Lorenzoni, Iurie Curosu, Sidnei Paciornik, Viktor Mechtcherine, Martin Oppermann, Flavio Silva.

DOI: 10.1016/j.cemconcomp.2020.103551

Abstract

Considering the multi-phase constitutive nature of strain-hardening cement-based composites (SHCC) and the decided influence of their micromechanics on overall material behavior, appropriate analytical methods are necessary for the representation of their microstructure and micro-kinematics. In this respect, micro-computed tomography (microCT) is an efficient, nondestructive technique, which can couple experimental testing with scale-linking numerical simulations. However, for a detailed analysis of microstructure, appropriate segmentation techniques must be applied which can accurately differentiate and represent the individual material phases and other features of interest. Given the small scale of analysis, the typical resolution of common computed tomography, and the small differences among the material constituents in terms of density and x ray absorption as well, the application of common segmentation techniques to SHCC is ineffective. In this work, a Deep Learning technique was applied to the microCT images of two different SHCC. The Deep Learning network parameters were analyzed and optimized on a high-strength SHCC and applied to the automatic segmentation of a typical normal-strength SHCC. The results obtained are highly promising and quantitatively in accordance with the composition of the samples analyzed. It was possible to segment the polymer fibers and the air voids from the cementitious matrices accurately, while the accuracy of the quartz-sand particles' segmentation imposed additional challenges and proved dependent on the properties of the surrounding hydrated phase.

Keywords: Segmentation; reconstruction; microstructure.; deep learning; x ray computed tomography; strain-hardening cement-based composite (SHCC).

4.1 Introduction

Strain-hardening cement-based composites (SHCC) represent a distinct type of fiber-reinforced concretes which yield controlled multiple cracking when subjected to increasing tensile loading (30). The multiple cracking in the strain-hardening phase results in remarkable tensile ductility before failure localization (softening) occurs. Furthermore, it ensures several positive features in terms of the mechanical performance and durability of elements made of or strengthened with SHCC (1)(3)(13)(14). Such superior properties are achieved by purposeful adjustment of the material composition, which targets a micromechanical balance between the cracking behavior of the fine-grained cementitious matrix and the crack-bridging behavior of the polymer microfibers (15)(16)(17).

The micromechanical "fine tuning" of SHCC compositions results in a high dependence of their mechanical behavior on various loading and environmental factors (14)(17)(18)(19). To understand and tailor the material response to various actions, appropriate micromechanical investigations such as single-fiber pullout and tension tests, are indispensable (14)(16)(85)(86). Besides the information delivered on the mechanics of SHCC at the constituent level, the micromechanical parameters obtained can be assembled in analytical (15)(16)(85) and/or numerical (87)(88)(89) models for scaling up and predicting the material behavior at the composite and structural scales.

However, the micromechanical tests on separate constitutive phases do not reproduce all the microstructural interactions in the composites. Furthermore, scaling down and reproducing thermal, dynamic and long-term loading conditions in micromechanical experiments is challenging and involves high levels of uncertainty. The active micromechanical mechanisms and damage processes in the composites can be assessed in dedicated testing configurations involving in addition non-destructive monitoring techniques such as Acoustic Emission (4)(90) or micro-computed tomography (microCT). The latter also enables an explicit representation of the decisive constitutive phases of SHCC, such as fibers, binder matrix, aggregates, and air voids, which can be coupled with detailed numerical modelling techniques (88)(89)(91)(92)(92)(94)(95).

MicroCT represents a powerful tool for coupled experimental-numerical analyses at the micro- and meso-levels since it can generate a 3D-representation of the material's microstructure (96)(97). With regard to cementitious composites, this technique was used to describe and quantify the internal damage mechanisms occurring under various actions at the fiber-level, for example, mechanical (22) or thermal (7). Moreover, in-situ microCT analyses make possible observation of the development of damage and deformations over time (20)(70), while the quantification of the corresponding kinematics, either global or local, can be done in the framework of Digital Volume Correlation (DVC) (98).

For the detailed reconstruction of the microstructure of fiber-reinforced composites, the specific material's constitutive phases must be differentiated and segmented based on objective criteria. The segmentation of steel fibers and air voids in cementitious matrices is relatively straightforward and is usually done based on the gray-values of the corresponding voxels in the microCT images (22). This is facilitated by the high density of the steel fibers as compared to the surrounding cementitious matrix and the resulting different x ray absorptions, thus giving rise to distinct bright areas. Conversely, the air voids result in darker areas when compared to the matrix. In the case of low density fibers they can also be resolved based on the grayscale of the image, such as polymer fibers (99). Although these fibers have dark tones as well as air voids, both can be differentiated by a shape criterion later.

In the case of SHCC, however, several challenges arise. First, the polymer microfibers and the fine aggregates in the cementitious matrices require high resolution for their detection and accurate morphologic representation. Usually this implies a compromise between the resolution of the scans and the size of the scanned specimen. Secondly, the low density of the polymer fibers does not allow their distinction from the air voids based on the gray values only. Similarly, the gray-value-based segmentation of the fine aggregates from the binder matrix is not possible due to their similar densities. Thus, more sophisticated segmentation techniques must be applied.

Manual segmentation by human operators is inefficient and involves significant uncertainties (23). On the other hand, machine learning is a method that uses algorithms which iteratively learn from data, allowing computers to formulate hidden insights without being explicitly programmed in respect of where to search (24). In other words, this technology uses a system to discover from raw data the representations needed to feature detection or classification automatically.

In this work a machine-learning-based segmentation method was applied to two different types of SHCC made of different fibers and cementitious matrices. The first composition studied consisted of a high-strength matrix and 6 mm-long, ultra-high molecular weight polyethylene (UHMWPE) fibers in a volume ratio of 2% (18). The other composition was a normal-strength SHCC made with 2% volume fraction of 12 mm-long polyvinyl alcohol (PVA) fibers (14)(42). These materials exhibited different morphologies at the micro-scale, resulting in distinct features of the microCT images.

To demonstrate the efficiency and potential of the Deep Learning (DL) segmentation technique, the high-strength SHCC was adopted as reference material for machine training. The segmented constituent phases were the air pores, fibers, and quartz sand particles. With the aim of showing that the same training can be applied to similar images, the trained network was directly applied to segment the normal-strength SHCC. Thereby it would be possible to confirm the suitability and high potential of this technique for describing the 3D micro-morphology of complex, multi-phase cementitious composites, such as SHCC.

4.2 Deep Learning technique and segmentation parameters

The Convolutional Neural Network (CNN) technique involves machine-learning which has performed excellently at tasks such as hand-written zip code digit classification (48) and face detection (49). In recent years, several works have shown that they can be also applied to more challenging visual classification tasks (50), such as in materials with complex microstructures (23)(26)(51)(52)(53)(54)(55)(56). These applications make increasing use of a class of techniques called Deep Learning (DL).

In DL, multiple levels of representation are obtained by composing non-linear modules that transform the representation at one level into a representation at a higher, slightly more abstract level. For classification tasks, higher layers of representation amplify aspects of the input that are important for discrimination and suppress irrelevant variations (57). The networks require as input a training set defined by the user upon the images. The network is trained until its outputs match the desired object classes within a certain error criterion. The trained network can be checked for satisfactory accuracy on a set of reference images and is then ready to be applied to other images.

For purposes of this work, CNN were developed within the Dragonfly software platform, which uses the popular DL TensorFlow engine in a user-friendly image processing environment. TensorFlow is a machine-learning system that operates on large scale and in heterogeneous environments such as image classification (100). In Dragonfly, TensorFlow was adopted along with Keras-format, Python-encoded CNN (101). It applies CNN in providing the users with an interface for connecting inputs and outputs, tuning parameters, iterating training, and inferring final results from new inputs (102).

There are several architectures for Deep Learning networks. The differences among them lie in the combination of convolution and pooling made from the input image. In this study the U-NET architecture was employed (103). This network has been shown to be efficient in segmenting biomedical images, in which very few annotated images were required for training.

The network takes the pixel intensities as input and the number of outputs is given by the number of phases to be segmented; additionally, there is an extra phase representing all the remaining image pixels not specified for training. In this project three phases of the material were segmented: fibers, sand particles and air voids.

A training set is prepared by manually marking objects of the different classes. Normally, for a typical 3D image with 1000 to 2000 layers, reasonable results can be achieved by training with just 10 to 20 training layers.

The training requires the optimizing of some parameters for better performance of the network. In the Dragonfly platform six parameters are required: patch size, stride-to-input ratio, number of epochs, batch size, optimization algorithm, and loss function.

The input images are divided into windows, sequentially scanned, and provided to the network. The patch size is expressed by the size of this window. The stride-to-input ratio is the displacement step of the analysis windows. The input pixel values go through a sequence of convolution and pooling operations until a final output is calculated. The result is then propagated backwards through the network and an error is calculated.

An epoch corresponds to one forward and backward propagation through the network. In each pass the error is reduced by adjusting the internal network weights using an optimization algorithm. As the number of parameters that must be optimized in an epoch is many times too big to feed to the computer GPU, it is divided into several smaller batches. The batch size is the number

of training samples in one forward and one backward pass. The loss function is a method for evaluating how well an algorithm models the given data. The loss function results in a large number if the predictions deviate too much from reality. However, in the learning process the loss function reduces the error in prediction. After a suitable number of epochs, the error reaches a predefined minimum value and the training stops.

4.3 SHCC compositions

The SHCCs analyzed in the current work represent typical compositions for their strength classes and have been comprehensively investigated by the authors in previous works (14)(42)(104). The SHCC mixtures were named according to the corresponding combinations of matrix and fibers, in which the normal-strength and the high-strength matrices were given the indices M1 and M2, respectively.

The high-strength SHCC matrix (M2) was specifically designed for an effective composite action with hydrophobic microfibers made of ultra-high molecular weight polyethylene (UHMWPE), produced under the brand name Dyneema SK62 by DSM (the Netherlands). These fibers, which will be abbreviated as PE in this paper, have an average diameter of 20 μm, a cut length of 6 mm and a density of 970 kg/m^3. Their volume ratio in M2-PE is 2%.

To ensure proper anchoring of the short, hydrophobic microfibers, the cementitious matrix should exhibit high strength and packing density. For this reason, the M2 matrix has a high cement content and a low water-to-binder ratio of 0.18. Silica fume (SF) was added in a moderate amount as a partial cement replacement to improve the frictional bond between the fiber and the matrix further; see Table 4.1. The micromechanical criteria for strain-hardening and multiple cracking in SHCC as well as the geometric nature of the polymer microfibers do not allow for the use of common aggregates since they increase the toughness of the matrix and negatively affect the distribution of the fibers (30)(1)(13)(14)(3)(15)(16). However, a small amount of quartz sand was added to ensure a certain stiffness and to avoid exaggerated shrinkage.

The PVA fibers used in the normal-strength SHCC (M1-PVA) are Kuralon REC-15 fibers produced by Kuraray, Japan. Their diameter is 40 μm; the cut length is 12 mm while their density is 1300 kg/m^3. As opposed to the PE fibers, the PVA fibers are highly hydrophilic and as such develop a

Table 4.1: Mixture compositions of SHCC under investigation.

	M2-PE kg/m³	**M1-PVA kg/m³**
CEM I 42.5 R-HS	-	505
CEM I 52.5 R-SR3/NA	1460	-
fly ash	-	621
silica fume	292	-
quartz sand 0.06 – 0.2 mm	145	536
PCE superplasticizer	25	10
PVA fibers	-	26
UHMWPE fibers	20	-
water	315	338
viscosity modifier	-	4.8

strong chemical bond with the cement-based matrices. To limit bond strength and avoid premature fiber rupture during crack formation, the cementitious matrices in PVA-SHCC are to have moderate strength and density. This is usually achieved by replacing a high portion of cement with fly ash, as shown in Table 4.1. Given the larger diameter of the PVA fibers in comparison to the PE fibers, and the large amount of fly ash used, a higher amount of quartz sand could be used in M1 without compromising its ductility.

The sand particles have different mechanical properties in comparison to the surrounding cementitious matrices, and their segmentation is interesting for micro-scale numerical simulations as well as for the general purpose of automatic aggregate segmentation in concretes and mortars. According to the mixture design, the volume ratio of quartz sand in M2-PE is approximately 5.3%, while in M1-PVA it is 19.5%. The particle size distribution of the quartz sand was measured using a laser diffraction particle size analyzer; it will be presented in sub section 5.5.2.1.

4.4 Specimen preparation and 3D-image acquisition

In the context of numerical modelling of SHCC with discrete fiber representation (104), dumbbell-shaped specimens were produced with a small thickness in the gauge length, see Figure 4.1. The small thickness of approximately 3.5 mm was intended to facilitate a proper experimental basis for 2D simulations, in which specific constraints regarding fiber orientation and distribution were encountered (104).

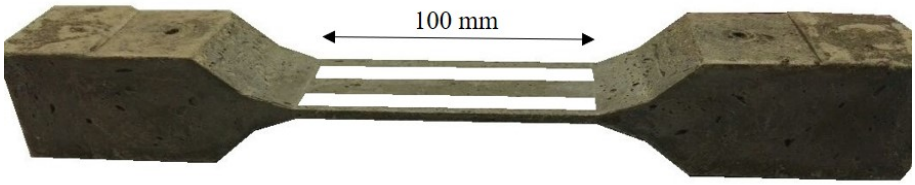

Figure 4.1: Original dog-bone specimen with a 3.5 mm thickness in the gauge length from which the SHCC strips for microCT investigations were extracted.

The small thickness of the specimens was achieved by pressing a horizontal plate into a prismatic mold filled with SHCC until the spacers arrested further displacement, see Figure 4.2. The applied pressure squeezed the fresh SHCC outward toward the open ends of the molds, which formed the thick end blocks for specimen fixation in the testing setup. The displacement of the fresh SHCC toward the end of the mold led to a longitudinal orientation of the fibers, which was a desired aspect both with regard to the numerical simulations and microCT scanning. Note here that the fiber orientation generally depends on the extent of the induced flow and the rheological properties of fresh SHCC.

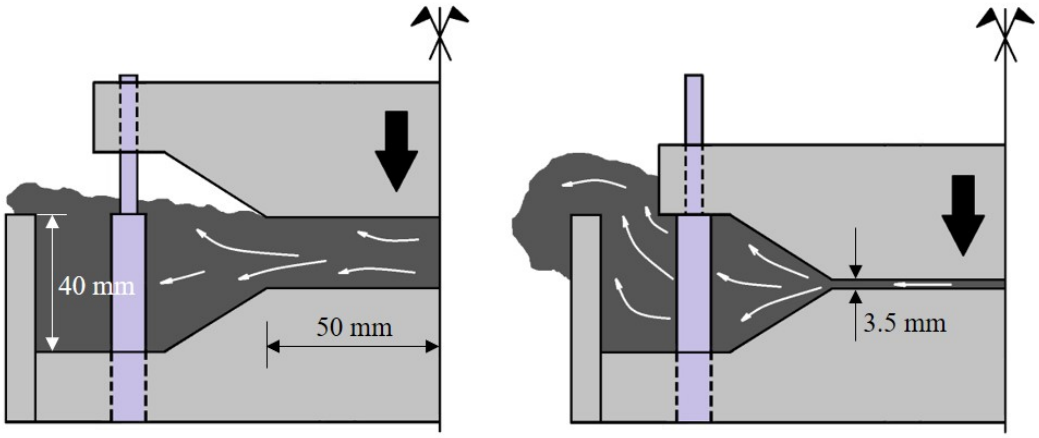

Figure 4.2: Schematic representation of a longitudinal section through the mold showing the imposed flow of fresh SHCC through applied pressure. Note that the excess material was already removed during the production process.

The dumbbell-shaped specimens were demolded after 24 hours of sealed curing in the molds. The mold elements were made of polyvinyl chloride (PVC), which is a hydrophobic polymer. Thus, the casted specimens had no moisture loss. After extraction from the molds, the specimens were stored in sealed plastic bags for 26 days under constant temperature (22°C) and relative humidity

(65% RH). Given that the microCT scans require comparable dimensions of the scanned cross-section in order to avoid beam hardening/attenuation effects, smaller SHCC stripes were subsequently cut longitudinally from the middle of the SHCC plates as shown in Figure 4.1. The miniature specimens scanned in the microCT represented thin strips of 100 mm length, 10 mm width, and 3.5 mm thickness. Besides the purpose of microstructure segmentation, these specimens facilitated in-situ tension tests accompanied by microCT analyses, which will be the subject matter of a future study. Note that the testing age of the specimens for numerical simulations as well as for in-situ microCT was 28 days, which is a standard age for determining the mechanical properties of cementitious materials.

The microCT scans were performed using a Nanotom X ray computer tomograph, which has an open high-power nano focus X ray tube transmission with a diamond target and a target material for X ray generation is wolfram (tungsten)(106), rotating sample holder and detector setup. The specimen was fixed vertically about the specimen's longitudinal axis; see Figure 4.3. The area of observation in the middle of the thin SHCC stripes was approximately 10 mm x10 mm.

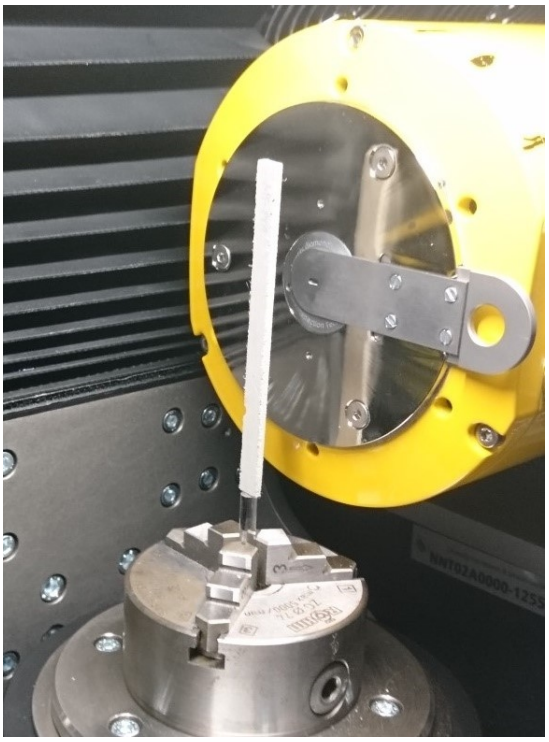

Figure 4.3: SHCC specimen fixed in the sample holder in front of the x ray source.

The scan parameters for the M2-PE specimen were: 100 kV voltage, 100 μA current and 1441 projections. A 16 bits image reconstruction is normalized according to the attenuation coefficients of the material phases, in which the 0 intensity of the image histograms is the least attenuating phase, while the highest intensity (65535) refers to the most attenuating phase, that is, the densest of the specimen. After reconstruction 1333 slices were obtained and each slice had 2212 by 1276 pixels. The voxel volume was (4.0 μm)^3. The scan parameters for the M1-PVA specimen were: 90 kV voltage, 100 μA current and 1441 projections. After reconstruction 1384 slices were obtained and each slice had with 1753 by 940 pixels. The voxel volume was (4.8 μm)^3.

The voxel size is determined by 1) ratio of distance between source and specimen to distance between specimen and detector, and 2) size of the volume to be scanned. The positioning of the sample between x-ray source and detector can be adjusted to ensure a desirable geometrical magnification of the scanned volume. Furthermore, there are several parameters, such as power, voltage, exposure time etc., that should be optimized in order to ensure an appropriate image quality.

4.5 Results and discussion

Figure 4.4 shows the scanned volumes of each sample.

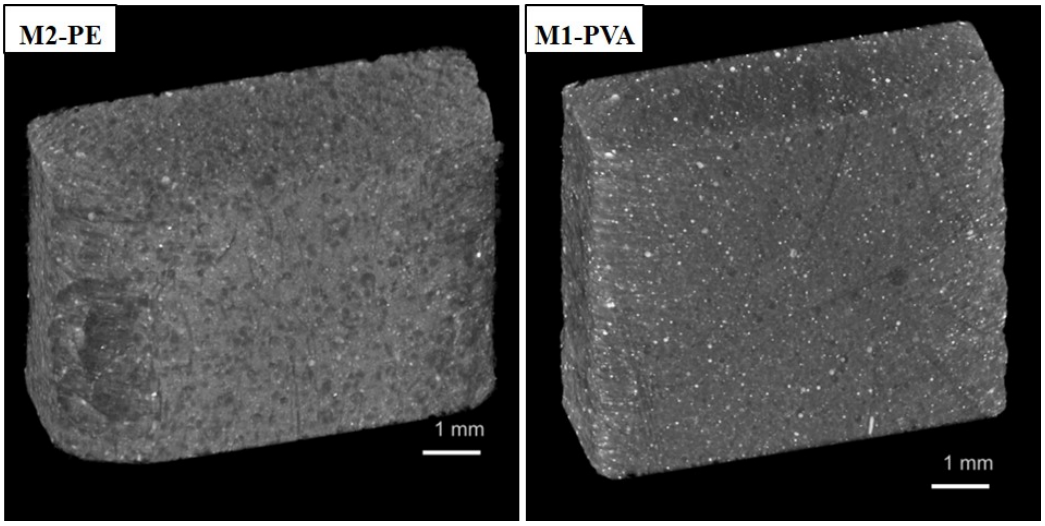

Figure 4.4: X ray scanned volumes from the M2-PE and M1-PVA specimens.

Although the focus of this work is the deep learning segmentation technique, a pre-processing sequence needed to be applied in the images. Pre-processing is a typical procedure for microCT images which mainly aims to improve image visualization and make further steps, such as segmentation, easier. In this work, pre-processing made it easier for the user to detect the phases for network training. It has also been found that deep learning shows better results in preprocessed images. A flow chart with the used software for each step is shown in Figure 4.5 for a better follow up of the next sections.

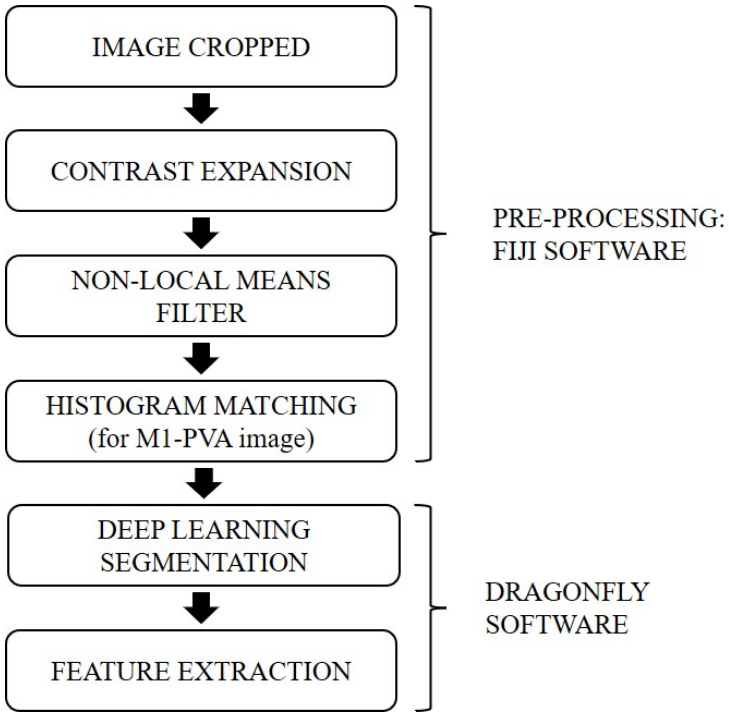

Figure 4.5: Image processing sequence with the corresponding software.

Even though the bulk density of M2 is higher than that of M1 (14), the dense sand particles are relatively well distinguishable in M2-PE images; see Figure 4.6. This is not the case for the M1-PVA image; see Figure 4.7. Hence, the methodology of this work was to create a network to identify pores, fibers, and sand in M2-PE and then use the same network to identify pores and fibers in M1-PVA images.

4.5.1 Image processing

First, both images were carefully cropped to eliminate the external regions. An automatic contrast expansion was applied to improve the visibility of the phases. As a positive side effect, this also reduced contrast differ-

ences between the several image layers, which can arise during image acquisition/reconstruction. The non-local means filter, an edge-preserving low-pass filter (79) available as a FIJI plugin (80), was applied to reduce noise. The result of its application with automatic sigma estimation is exemplified by a 2D slice of M2-PE image in Figure 4.6 The edges between the phases are considerably sharper in comparison to the unfiltered images, thus making manual delineation for training much easier. It was also verified that noise reduction was critical for the DL method, especially in the identification of the sand phase.

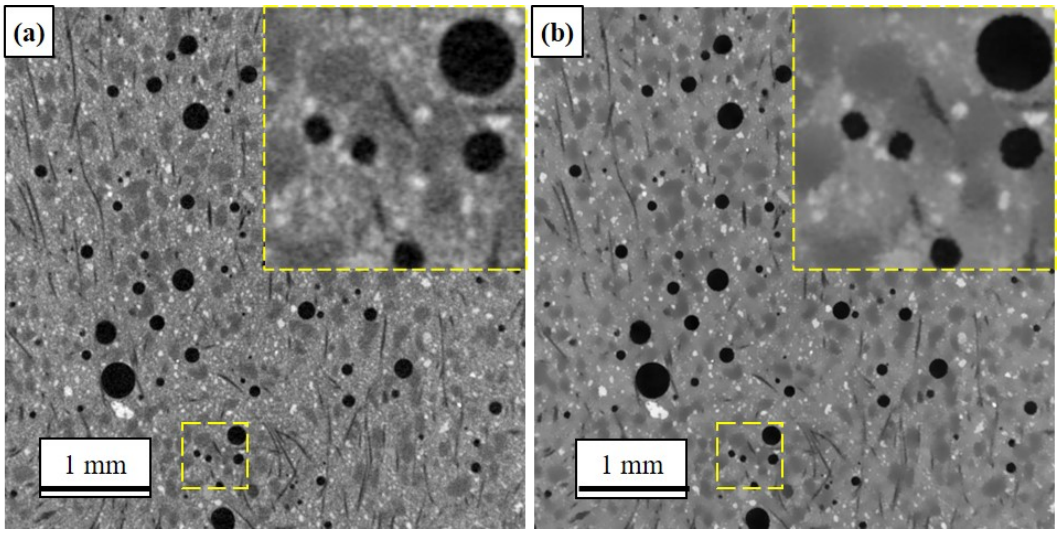

Figure 4.6: Noise reduction M2-PE image: (a) before and (b) after the application of the 2D non-local means filter.

Besides the air voids and the fibers, three material phases can be distinguished in the microCT slices in Figure 4.6b. The round, dark-gray areas are the sand particles. These are surrounded by the light-gray hydrated binder phase and by bright areas, which most probably represent unhydrated cement particles and clumps of SF particles. The relatively high amount of unhydrated cement is normal for high-strength cementitious matrices due to the low water-to-binder ratio. As for the possible presence of SF clumps: the small amount of very fine aggregates does not allow for sufficient internal shear action for breaking all clumps of fines during the mixing process.

In M1-PVA the fibers have larger diameter and length and the air void content of the binder matrix is lower. The contrast of the image is different due to the different densities of the matrices of the two types of SHCC under investigation. It was verified that this difference in the quantity and size of

voids and fibers did not influence the generalization of the network. However, applying a network to images with different contrast ranges showed that the network was very sensitive to that feature and did not work well.

As a solution for that, a technique called histogram matching was applied (107). This technique can be used to normalize two images or normalize layers of the same image based on the histogram of a reference input image. Thus, an image used as input to train the network was also used as a reference to normalize the histogram of the images to which the network was applied. Figure 4.7 shows an original M1-PVA image and the same layer after histogram matching was applied based on an M2-PE image as reference.

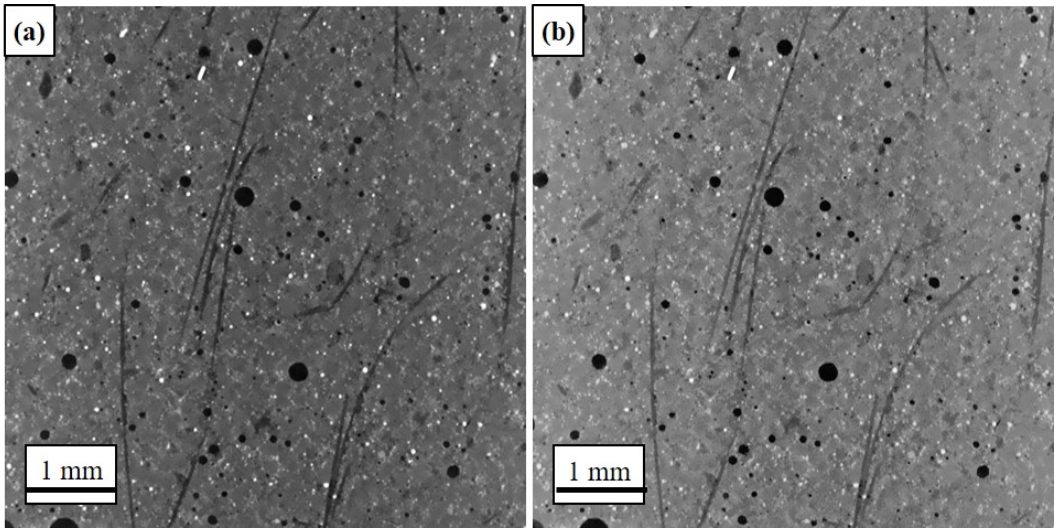

Figure 4.7: Histogram matching: (a) original M1-PVA image and (b) the same layer after histogram matching based on an M2-PE reference image.

4.5.2 Segmentation of SHCC's constituents

A standard way of segmenting different phases of a material in an image is to choose a cut-off on the gray-value range of the pixel intensity histogram (thresholding). However, this is only possible in cases where the different phases have different peaks in the histogram.

The histograms of all 2D slices of the M2-PE and M1-PVA images are shown in Figure 4.8. An assessment before and after application of non-local means was made, showing that the noise reduction filter concentrates the peaks in a lower range of gray value. In the case of M2-PE, better separation between the peaks for sand and matrix was observed.

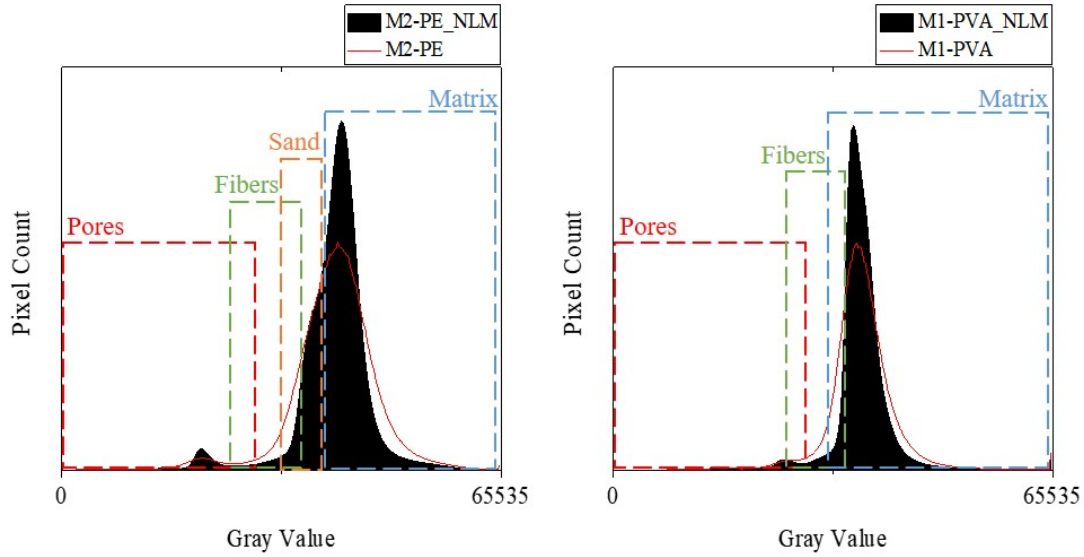

Figure 4.8: Histograms for all layers of the 3D image: M2-PE and M1-PVA; the red curves correspond to the original image; the black filled curves correspond to the images filtered with the non-local means filter.

The first peak in both cases can be attributed to air voids, which are represented by the darkest pixels in the image. However, there is some overlap between the intensity ranges of pores and fibers, and thus a simple thresholding cannot be used. Shape criteria could in principle be used to discriminate among them. However, the fibers also share intensity ranges with sand particles in M2-PE and with the matrix in M1-PVA. Additionally, as in the case of the fibers, resolution is a limiting factor in segmenting smaller particles, i.e. particles with diameters comparable to the voxel size. Thus, the quantification of the phases of interest requires the use of another technique, such as Deep Learning.

4.5.2.1 Deep Learning training and segmentation

The training database for each present class is determined by regions of interest (ROI's) delineated manually from a subset of 2D slices. First, the training database was prepared in 10 slices from the M2-PE image as shown in Figure 4.9, where the delineated voids, fibers and sand are shown in blue, red and green, respectively. These ROI's are then provided as output to train the network, and the original image (Figure 4.9a) is used as input. The training was subsequently performed with the parameters shown in Table 4.2. Once trained, the network can be applied to all slices and/or other images of the same type.

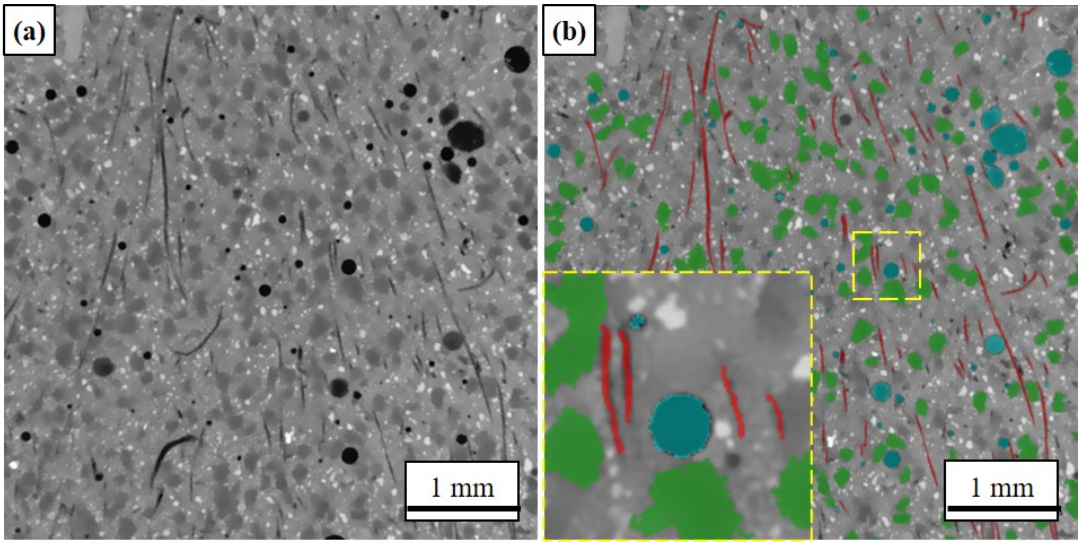

Figure 4.9: Phase drawing for network training: (a) original M2-PE image and (b) image with drawn samples of voids (blue), fibers (red) and sand (green). Please refer to the digital version of the manuscript for color clarification.

Table 4.2: Deep learning parameters.

Input (patch) size (pixels)	128
Stride to input ratio	1
Epochs number	50
Batch size	64
Loss function	Categorical cross entropy
Optimization algorithm	Adam

The network result applied to the M2-PE image is shown in Figure 4.10. The 3D images display each segmented phase, i.e. voids in blue, fibers in red and sand in green.

Initially, a segmentation of voids by thresholding in M2-PE image was carried out in order to compare with the results obtained by Deep Learning. A threshold intensity of 27000 was used in the histogram, which resulted in the segmentation of some fibers as well. To eliminate segmented fibers, the sphericity parameter was used. Sphericity is a function of the volume and of the surface area of a void (7); objects of sphericity less than 0.2 were eliminated. By this method the porosity was 2.8%, while the porosity according to DL was 3.0%. These values are very similar, i.e. less than 10% difference, but visually the result of the DL is better since separation by shape leads to some errors.

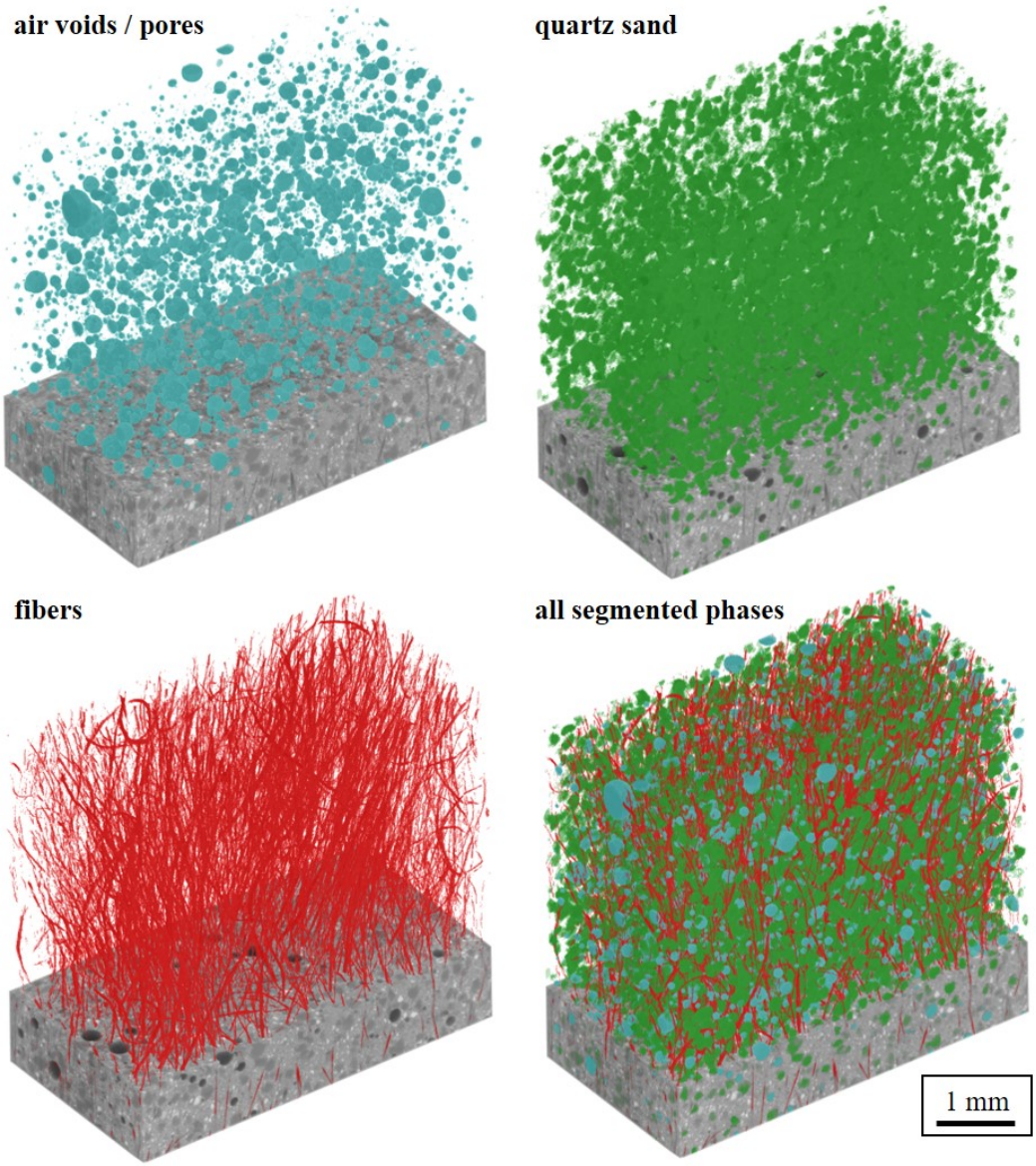

Figure 4.10: 3D images of M2-PE segmented by Deep Learning: voids, sand, fibers and all phases together. Please refer to the digital version of the manuscript for color clarification.

The fiber volume fraction obtained by DL was 1.7%, slightly lower than the fraction actually used when producing the SHCC samples (2%). A possible reason for this relates to the small fiber diameter of approximately 20 μm which, with a voxel size of $(4\ \mu\text{m})^3$, leads to an inaccurate geometrical representation of the fiber cross-section and, as a result, of the fiber volume. A more accurate method involves counting the fibers in the microCT slices and considering their real diameters to calculate their surface and/or volume ratio. Using this method, the resulting volume fraction of fibers is 2.4%. The deviation from the design value can be related to the non-uniform fiber distribution in the donor specimens.

Figure 4.11 compares the nominal particle size distribution of the quartz sand, as measured using a laser diffraction particle size analyzer, to the particle size distribution yielded by image analysis of the DL segmented objects. Note that nominal distribution characterizes the quartz sand as bulk and not in SHCC. Due to the difficulty in determining the boundary between the sand and the surrounding hydrated phase, the segmentation of the sand particles did not show sharp boundaries. That is why the evaluated sand content by volume in M2-PE was not close to the percentages given by the mixture composition, 8.2% vs 5.3%, respectively. The particle size distribution yielded DL is given by the Max Feret Diameter, which is the longest distance between any two points along each object boundary at an arbitrary angle. Despite the obvious difference, the estimation can be regarded as reasonable. In future research, the authors will considerably extend the number of samples taken from each SHCC plate specimen produced, so that a representative statistical evaluation can be performed. In the presentation at hand, however, the authors have focused on the image processing methodology as such.

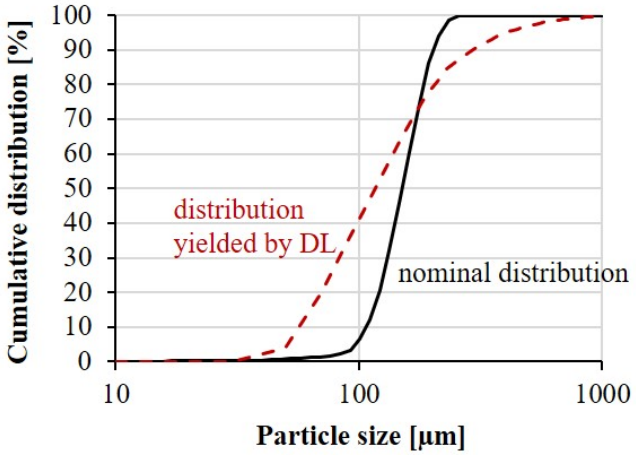

Figure 4.11: Comparison between the nominal particle size distribution of the quartz sand and the distribution yielded by image analysis based on the DL segmented sand in M2-PE.

The same network was eventually applied to the M1-PVA image and the result is shown in 3D in Figure 4.12. The porosity in this case was 2.4% and the deduced fiber volume fraction was 1.4%. By counting the number of fibers crossing different slices and dividing their real cross-section by the surface area of the respective slice, the resulting volume fraction of fibers is 1.8%. Similarly, for M2-PE a higher resolution is needed for a more accurate representation of the fiber volume.

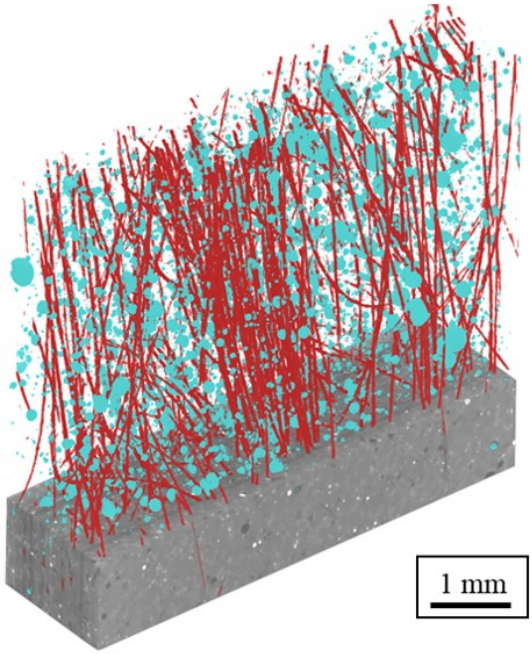

Figure 4.12: Segmented 3D voids (blue) and fibers (red) in M1-PVA image by Deep Learning. Please refer to the digital version of the manuscript for color clarification.

Note that a successful segmentation represents an essential step for further analytical, nondestructive investigations of the constitutive structure of the materials under study. The quantification of pore size distribution, aggregate content and particle size distribution, fiber volume fraction, and orientation etc. with traditional techniques (such as microscopy, mercury intrusion, etc.) involves considerably higher efforts and sample destruction (5)(108). The 3D-fiber segmentation using Deep Learning can yield a more accurate and efficient quantification of these parameters (109).

4.6 Conclusions and outlook

Micro-computed tomography applied to SHCC is an extremely valuable tool in analyzing their microstructure and potentially in assessing the damage developing in such materials due to various actions. An objective quantification of the material morphology and damage requires an accurate segmentation of the relevant constitutive phases and of cracks. In this context, SHCC represent a challenging class of materials because of the imposed scale of observation and physical properties of typical constituents.

The Deep Learning technique is a novel method with a high potential for an accurate and efficient segmentation of complex microstructures, which cannot be performed by applying common methods such as the gray-value thresholding. When a good training basis is developed, it can be applied in the automatic segmentation of other similar images. This principle was demonstrated in the current work on two different types of SHCC. The training set was developed based on a high-strength SHCC made with Dyneema fibers, in which polymer fibers, voids and quartz sand particles were distinguished. The same set was applied to a normal-strength SHCC made with PVA fibers. The automatic segmentation was successful in the case of fibers and air voids, while quartz sand particles could not be differentiated because of their corresponding gray-value range being heavily overlapped with that of the surrounding hydrated cement phase. To elucidate this issue, the morphology of M1 will be characterized by the authors with complementary methods, such as ESEM, EDX etc. and solutions will be proposed for a more detailed microCT segmentation of matrices similar to M1, e.g. with contrast enhancing agents.

The in-situ experimental testing of SHCC specimens represents the next step for a coupled experimental-numerical analysis of SHCC at the micro-scale. Crack formation and propagation depending on the loading mode and material morphology represent the declared goal for future studies. In this context, the quantification of the global and local deformations in the framework of Digital Volume Correlation (DVC) is a challenging but highly interesting task.

5
Combined mechanical and 3D-microstructural analysis of strain-hardening cement-based composites (SHCC) by in-situ X-ray microtomography

Renata Lorenzoni, Iurie Curosu, Fabien Leonard, Sidnei Paciornik, Viktor Mechtcherine, Flavio Silva, Giovanni Bruno

DOI: 10.1016/j.cemconres.2020.106139

Abstract

The paper presents the results of a series of combined mechanical and in-situ morphological investigations on high strength strain-hardening cement-based composites (SHCC). Tension and compression experiments were performed in a CT scanner employing a dedicated mechanical testing rig. The in-situ microtomographic scans enabled correlating the measured specimen response with relevant microstructural features and fracture processes. The microstructural segmentation of SHCC was performed in the framework of Deep Learning and it targeted an accurate segmentation of pores, fibers and aggregates. Besides their accurate volumetric representation, these phases were quantified in terms of content, size and orientation. The fracture processes were monitored at different loading stages and Digital Volume Correlation (DVC) was employed to spatially map the strains and cracks in the specimens loaded in compression. The DVC analysis highlighted the effect of loading conditions, specimen geometry and material heterogeneity at the mesolevel on the strain distribution and fracture localization.

Keywords: SHCC; in-situ X-ray microCT; microstructure; Deep Learning; Digital Volume Correlation

5.1
Introduction

Strain-hardening cement-based composites (SHCC) are fiber-reinforced cementitious materials that can withstand considerable tensile stresses over a significant deformation range before failure localization (30). Such a tensile behavior is a result of the formation of multiple cracks in the strain-hardening

phase, ensuring additionally a marked crack control at large deformations (1). These features make SHCC suitable for retrofit and strengthening applications as well as for new structural elements aiming enhanced durability, damage tolerance and energy dissipation (1)(31)(42)(43)(44)(19)(38)(39).

The superb tensile behavior of SHCC is achieved through micromechanical fine-tuning of the matrix composition according to the employed fibers, targeting a balanced relation between the fracture toughness and strength of the cementitious matrix, mechanical and geometric properties of the fibers and fiber-matrix interaction (16)(110)(111). Various analytical models have been developed for predicting the crack opening and multiple cracking behavior of SHCC under tension (112)(113)(86) and shear (114)(115). These models rely on data from micromechanical experiments, such as single-fiber pullout and tension tests (116), and on analytical and statistical assessments of fiber orientation and distribution (117)(118) and flaw size distribution (119)(120). Besides enabling a performance-based material design, these models represent a handy tool for predicting and interpreting such phenomena as strain rate sensitivity (121)(17)(122), assess the effects of different mechanical and surface properties of the fibers (123), and can deliver input constitutive laws for numerical simulations at larger scales (123). However, the assembly of the experimentally determined micromechanical parameters into analytical and phenomenological models can only roughly approximate the composite behavior. Furthermore, these models do not consider various effects which accompany the experimental upscaling, such as the effect of size on crack formation and propagation, effect of fiber content on porosity and on the effective fiber anchorage (125), etc. Thus, there is a need for an intermediate assessment scale, which would involve a realistic and discrete consideration of the material morphology to assess the composite response under various loading and exposure conditions. Furthermore, a combination of experimental and numerical investigations at this scale of observation would enable the definition of sound constitutive laws for SHCC, involving basic micromechanical and fracture mechanical parameters.

Traditional methods for morphologic assessment, such as microscopy, involve destructive specimen preparation techniques and deliver only limited information about the spatial distribution of the analyzed components (108). On the other hand, X-ray computed tomography (microCT) represents an effective non-destructive method for a 3D representation of the material constitutive structure (126). Furthermore, this technique can be used to analyze the internal damage extent in cementitious materials due to mechanical loading,

thermal exposure or delayed chemical reactions (127)(71)(128)(7). For a comprehensive experimental scale-linking, the X-ray computed tomography should be coupled with real-time deformation and damage processes. In-situ microCT investigations can enable an accurate damage assessment (27)(129)(59) and relate it to the relevant microstructural features of the material (130). Moreover, the analysis of active deformation and damage processes can be complemented by Digital Image Correlation (DIC) in 2D or by Digital Volume Correlation (DVC) in 3D (28)(29)(58)(129). Besides enabling a detailed assessment of the origin and type of fracture, this could also facilitate a coupled experimental-numerical analysis at the meso-level.

In a previous work by the authors (9), microCT was employed to volumetrically map the microstructure of two different types of SHCC. However, the pronounced overlap of the gray value spectra (21)(131)(109)(95)(23)(52)(54) of the individual constitutive phases in the X-ray scans restricted the use of traditional methods for the microstructural segmentation. This served as incentive to perform the segmentation in the framework of Deep Learning (DL) (51), which enabled an accurate segmentation of fibers, pores and fine sand particles, as well as the quantification of their size distribution, volume fraction and orientation.

The successful segmentation of SHCC's microstructure facilitates a coupled mechanical-microstructural analysis of the composites, as presented in the paper at hand. A high-strength SHCC was investigated, consisting of a fine-grained cementitious matrix and ultra-high molecular weight polyethylene (UHMWPE) microfibers. The in-situ microCT analysis consisted of tension and compression tests on miniature SHCC specimens. The scans were performed prior to load application as well as at different pre-peak and post-peak loading stages. Another novelty of the presented research is that the essential microstructural features of the loaded specimens (including fibers) were not only visually presented, but also explicitly segmented using DL, and quantitatively analyzed in terms of orientation, size and content. Furthermore, the fibers and pore analysis could be directly related to the measured load-deformation histories, as well as to the strain distribution and crack formation in the specimen by means of DVC. The paper focuses on the testing and evaluation methodologies based on a small but representative experimental series. A detailed analysis of the material behavior at the meso-scale will be a matter of more extensive upcoming studies.

5.2 Materials and experimental investigations

5.2.1 SHCC composition

The high-strength SHCC analyzed in the current work consists of a high-strength cementitious matrix, which was purposefully designed for an effective composite action with hydrophobic UHMWPE micro-fibers (42)(18)(14). This composite was extensively investigated at different scales of observation in previous works (18)(132)(133) and its microstructure was successfully segmented in the previous work using DL (9). The high-strength SHCC shows a high ductility under quasi-static tensile loading at common observation scales (18), making it interesting to analyze the multiple cracking and fracture processes also at the micro- and meso-scales.

The cementitious matrix of the investigated SHCC had a high cement content and a low water-to-binder ratio of 0.18. Silica fume was added in a moderate amount as partial cement replacement, see Table5.1. Given the micromechanical requirements for strain-hardening and multiple cracking, only a limited amount of aggregates was added in form of fine quartz sand with a maximum particle size of 200 μm. A higher content or size of aggregates would increase the fracture toughness of the matrix and negatively affect the fiber distribution, both effects being undesirable with regard to steady-state and multiple cracking (131).

Table 5.1: Composition of the high-strength SHCC under investigation.

Components	**Content in kg/m^3**
CEM I 52.5 R-SR3/NA	1460
Silica fume	292
Quartz sand 0.06 – 0.2 mm	145
Superplasticizer	25
UHMWPE fibers (2% by vol.)	20
Water	315

The UHMWPE (PE, for short) fibers are produced by DSM, The Netherlands, under the brand name Dyneema SK62 (134). According to the information provided by the producer, the fibers have an average diameter of 20 μm, a cut length of 6 mm and a density of 970 kg/m^3. Their tensile strength is 2500 MPa, while the Young's modulus is 80 GPa (134).

In a previous study by the authors, this high-strength SHCC was investigated on its tensile behavior using dumbbell-shaped specimens with a cross-section of 24 mm x 40 mm in the gauge portion and a gauge length of 100 mm. The compressive strength was measured on cubes with side length of 100 mm. Both the tension and compression experiments were performed at an age of 14 days. The average first crack stress was 3.8 MPa, the tensile strength was 7.6 MPa with the strain at peak load (strain capacity) of 3.9% in average, while the compressive strength was 134 MPa (18).

5.2.2 Specimens for tension experiments

The mechanical investigations in the current work were part of a wider framework involving numerical simulations of SHCC with discrete fiber modelling at the micro- (92) and meso-scales (104). The numerical investigations at the micro-scale are aimed at formulating a consistent two-scale homogenization framework to simulate SHCC under dynamic loading, while the meso-scale model should allow a detailed analysis of the composite behavior depending on material morphology and micromechanical properties. Finally, both approaches aim at defining representative volume elements for an efficient and reliable modelling of SHCC at the macro-scale (132). In previous works, dumbbell-shaped specimens with novel geometrical features were produced and tested for an appropriate experimental basis for 2D numerical investigations (104), see Figure 5.1. A detailed description of the specimen production technique was presented in (9). This specimen shape was attained by pressing a horizontal plate into a special mold filled with fresh SHCC until the specimen got the desired thickness. The applied pressure squeezed fresh SHCC outward towards the open ends of the molds, in this way inducing a unidirectional fiber orientation.

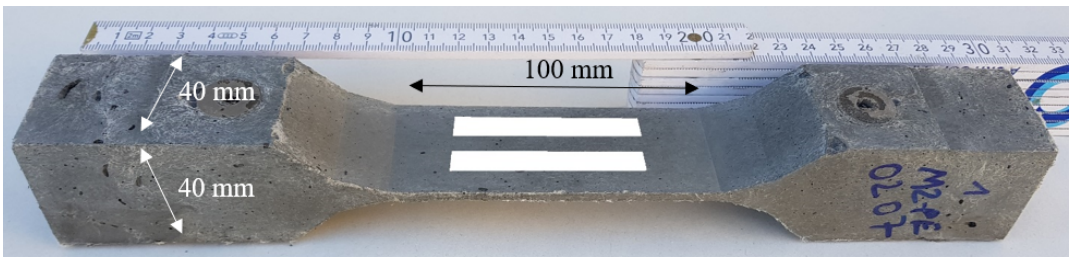

Figure 5.1: Dumbbell-shaped SHCC specimen from which the miniature tensile specimens were extracted for the in-situ microCT investigations.

However, in the current work the in-situ testing rig and the specimen gripping principle imposed spatial and geometrical constraints, respectively, which only allowed testing specimens with dimensions considerably smaller than those presented in Figure 5.1. For this reason, miniature plate-like specimens were extracted from the specimens in Figure 5.1 and tested in tension. Similar to the previous work by the authors (9), the specimens for the tension tests were extracted from the 3.5 mm-thick gauge portion of the dumbbell-shaped specimens, as indicated with white stripes in Figure 5.1. The miniature specimens were cut as 10 mm-wide stripes in the longitudinal direction of the samples using a 1.5 mm-thick disc saw. They had a length of 60 mm and, in order to localize failure in the observation zone of the microCT, notches were cut on both specimen sides with an approximate depth of 2 mm; Figure 5.2. The total length of 60 mm allowed for a free specimen length of 35 mm, their ends being clamped in the 12 mm-wide gripping jaws of the testing rig.

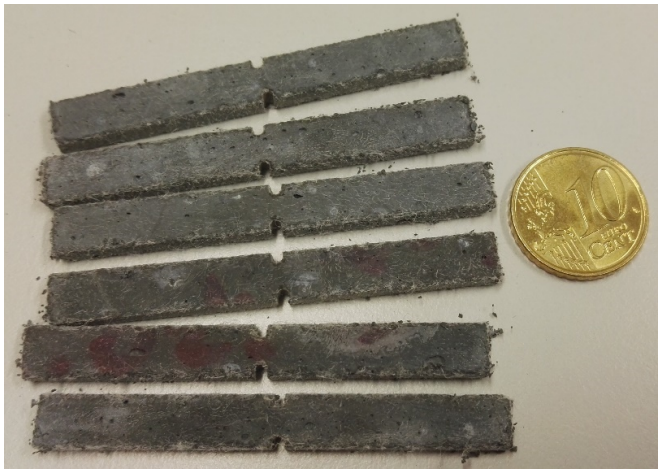

Figure 5.2: Miniature SHCC specimens for tension experiments.

These specimen dimensions also facilitated a relatively small voxel size in the 3D reconstructions (or pixel size in the 2D slices). Ensuring a voxel size smaller than the dimensions of the features of interest, e.g. fiber diameter, is important for allowing their semantic segmentation.

For specimen preparation, the freshly cast dumbbell-shaped samples were cured in sealed molds for 24 hours. The subsequent curing after specimen extraction was done in sealed plastic bags in a climatic chamber with constant temperature of 20°C and relative humidity of 65% for 26 days. Subsequently,

the thin stripes were cut and stored again in sealed plastic bags for approximately 2 months. Due to logistical constraints, the specimen age at testing was approximately 3 months.

5.2.3 Specimens for compression experiments

From previous studies it was known that the compressive strength of the investigated SHCC at an age of 14 days ranges between 130 and 140 MPa (18)(14). effects and the specific boundary conditions, a maximum specimen cross-section of 30 mm^2 was preliminary imposed. The compression samples were not produced from the plate-like elements described above, since with cross-section dimensions of 3.5 mm the specimen height should have been inadequately small, in order to avoid stability issues in compression. Note that a small specimen height would lead to extensive image quality problems due to X-ray scattering from the metallic loading elements at the top and bottom boundaries of the specimens. Because of this, the compression specimens were extracted from larger dumbbell-shaped SHCC specimens commonly used in uniaxial tension tests and described in detail in previous studies; see e.g. (18). The same curing conditions and testing age were adopted as for the tensile specimens. The miniature specimens had square cross-sections with side dimensions of 5 mm, while their height was 15 mm; see Figure 5.3.

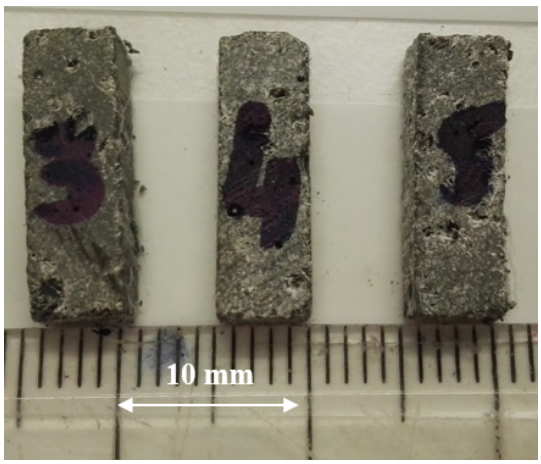

Figure 5.3: Miniature SHCC specimens for compression experiments.

For a detailed demonstration of the range of parameters which can be investigated with the help of in-situ microCT tests, the miniature compression specimens were extracted both longitudinally and transversally from the

dumbbell-shaped samples. Given that the primary (i.e. donor) dumbbell-shaped specimens were produced intending a longitudinal fiber orientation, the miniature compressive specimens featured predominantly uni-directional fiber orientation either in the longitudinal or transversal direction.

5.2.4 Scanning device and in-situ testing configuration

The in-situ microCT tests were performed in the facilities of the Federal Institute for Material Research and Testing (BAM) in Berlin, Germany, using an industrial GE VTomeX CT scanner. The scan conditions were 70 kV and 160 μA and each scan had a duration of 1 hour. After reconstruction, 2024 slices with 750 x 1250 pixels were obtained with a voxel size of (13 μm)^3. In the previous study by the authors, the segmentation of two types of SHCC was carried out on microCT scans with a voxel size of (4 µm)3. It will be shown in this study that, despite the fiber diameter of around 20 μm, a voxel size of (13μm)^3 is appropriate for the detection and segmentation of the fibers using DL.

The mechanical testing stage CT5000 produced by Deben, UK, is presented in Figure 5.4. The testing rig limited the proximity of the specimen to the X-ray source, thus limiting also the extent of geometric magnification. It has a load capacity of 5 kN both in tension and compression, and a maximum stroke of 10 mm. The maximum specimen length for tension tests is 70 mm while for compression the maximum height is 49 mm. Since the compression specimens were only 15 mm high, cubic aluminum elements with side dimensions of 10 mm were used to induce the load and enable the operation of the compression testing rig in its middle stroke range. Aluminum was chosen instead of steel because of its relatively low density and limited negative effects on the X-ray scans at the specimen ends. The displacement rate in the tension experiments was 0.1 mm/min, while in the compression tests it was 1 mm/min. Given that the loading processes were stopped for each CT scan in the in-situ tests, the displacement rate played only a secondary role, as it will be discussed in the next sections.

Figure 5.4b presents an exposed tensile specimen clamped in the testing device. After specimen fixation in the gripping elements, a vitreous (glassy) carbon support tube was installed on the stage over the specimen, as shown in Figure 5.4a. The thickness of the tube wall was 3 mm, its height was 285 mm and the diameter was 117 mm. The role of the tube is that of a stiff frame

around the specimen, which ensures the load transfer and specimen support, at the same time being transparent to X-rays. In tension tests the tube works in compression, while in compressive tests it works in tension. Prior to testing, the steel gripping element on the top of the specimen is tightened to the cap of the glass tube and the vertical steel rods connecting the top and bottom jaws are removed. In compression, the sample's height is measured accurately, and the rig jaws spaced accordingly (spacing slightly larger than the sample's height). The sample is placed between the jaws, the rig is then closed and the jaw placed into contact with the sample (loading force of 10 N). The force and displacement are then reset to zero and the compression test is started.

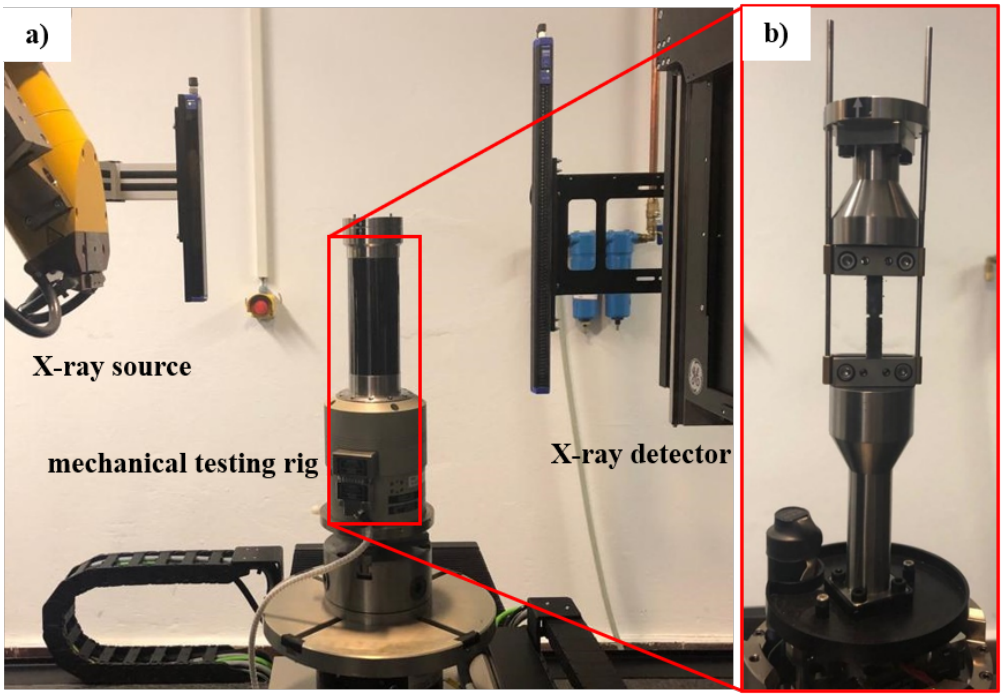

Figure 5.4: a) In-situ testing rig installed in the CT scanner and b) exposed tensile specimen clamped in the testing device (without the support tube).

Prior to the in-situ tests with X-ray scans, preliminary mechanical tests were performed accompanied by 2D radiography with a sampling rate of one image every two seconds. These experiments were aimed at assessing the mechanical response of the samples in order to define the force and/or the displacements at which the loading should be stopped for the X-ray scans in the subsequent in-situ tests. These 2D radiographic scans were only performed in one direction, i.e. they did not involve stage rotation. Although not discussed in detail in the current work, the 2D scans present a certain potential with regard to a statistical assessment of the distributed fracture process, as well

as for the observation of damage development and structural changes with a considerably higher time resolution compared to the 3D microCT scans.

5.2.5 Image processing and Digital Volume Correlation (DVC)

A pre-processing intended to reduce noise was applied to all reconstructed microCT images using the non-local means filter (79), which is an edge-preserving low-pass filter available as a FIJI plugin (80). Image processing and analysis, including traditional and DL segmentation, as well as volume, shape and orientation measurements were carried out with Dragonfly (Object Research Systems, Montreal, Canada), similar to the previous study by the authors (9).

To map and quantify the strains in the compressed specimens, DVC evaluation was performed with the software VIC-Volume (Correlated Solutions, North Carolina, USA). For this purpose, the software locates a specific sub-volume in two or more sequences of images and performs image matching with optimal accuracy. The optimal matching is performed through minimization or maximization of a metric function that quantifies the level of similarity in sub-volumes between the reference and deformed volumetric images. In order to reduce the computation time that is accrued for the large volumetric images, the least square form is used as metric function (135).

The sub-volume size must be set by the user through a parameter called "subset size" in a way that each of the sub-volumes contains a pattern of sufficient contrast. Thus, the subset was chosen such that it has one or more phases within it. Figure 5.5 presents a scheme of the arrangement of voxels, subset and the entire analysis volume. The amount of analyzed sub-volumes depends on the defined "step size", so that large step sizes result in smaller output data but run faster. This parameter should not be too large so that image information is not lost, and not too small so that the computer can process efficiently. All sub-volumes can have the same weights by choosing the uniform weight or can follow a Gaussian influence. The user must also choose the order of the interpolation, with higher orders offering more accurate results. Three variations of the least square form are offered by the software as a correlation criterion: square differences, normalized square differences and zero-normalized square difference. Finally, the multi-processor parameter indicates the number of used parallel threads (136). The DVC parameters used in this work are summarized in Table 5.2.

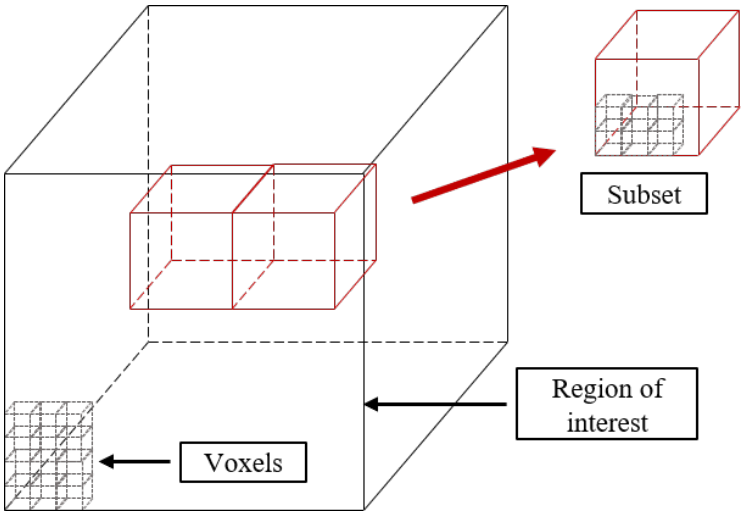

Figure 5.5: Schematic with object volume, sub-volumes and voxel elements.

Table 5.2: Correlation parameters for DVC.

Subset size	25
Step size	10
Subset weights	Gaussian weights
Interpolation	Optimized 6-tap
Criterion	Normalized squared differences
Multi-processor	24

5.3 Results and discussion

5.3.1 Tension experiments with in-situ 2D X-ray scans

The reference tension experiments were accompanied by 2D X-ray (radiographic) scans instead of 3D X-ray tomography. In these tests the loading process was continuous, which enabled defining the reference range of force and deformation attained by the SHCC specimens, in order to determine the load stages at which the X-ray scans should be performed in the 3D in-situ investigations. Furthermore, the radiographic scans were performed also prior to load application for assessing the presence of micro-cracks, which were not visible by visual inspection and which could possibly be induced during specimen clamping or even during specimen preparation. Actually, initial cracking was an issue in the performed testing series, which was traced back to the bending and torsion efforts generated in the specimens during the tightening

of the top gripping elements to the carbon casing. This issue is related to the gripping configuration, to the small specimen cross-section and to the presence of notches.

Nevertheless, the presence of micro-cracks (usually one single crack) prior to load application did not hinder the combined evaluation of the material morphology and mechanical behavior, since failure localization occurred elsewhere after a pronounced multiple cracking phase, as shown in Figure 5.6 and Figure 5.7. The representative stress-displacement curve of a notched high-strength SHCC specimen presented in Figure 5.6 shows a non-linear ascending branch before the first stress drop at 14 MPa. This is a result obtained with an initial crack induced during specimen clamping, see first scan in Figure 5.7. The stress was calculated according to the reduced cross-section in the notched region of the sample. The equivalent peak force in the presented curve is approximately 300 N.

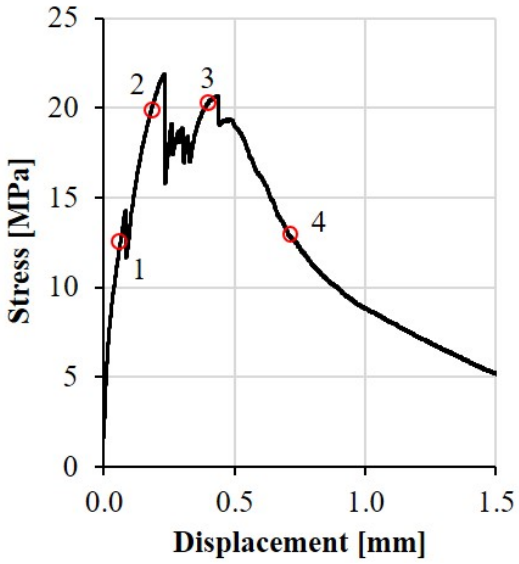

Figure 5.6: Tensile stress-displacement curve corresponding to a preliminary tension test accompanied by 2D X-ray scanning. Numbers 1 to 4 correspond to specific values for which radiographic images were acquired; see Figure 6.7.

Note that the attained tensile strength is considerably higher compared to the results obtained on specimens of common dimensions and geometries (42) (18). One of the reasons for the high tensile strength is the unidirectional fiber orientation in the miniature specimens, as it will be demonstrated later in this section. Also, the small specimen cross-section facilitated steady-state cracking and a uniform crack opening at failure localization, in this way exploiting the

crack bridging capacity of the fibers uniformly along the entire crack length, as shown in Figure 5.7. Finally, the presence of notches usually leads to an enhanced tensile strength in SHCC (42)(122)(14), which can be traced back to the fact that the notches impose failure in predefined locations, which do not necessarily coincide with the weakest cross-sections in the specimens from the material point of view, e.g. due to larger flaws.

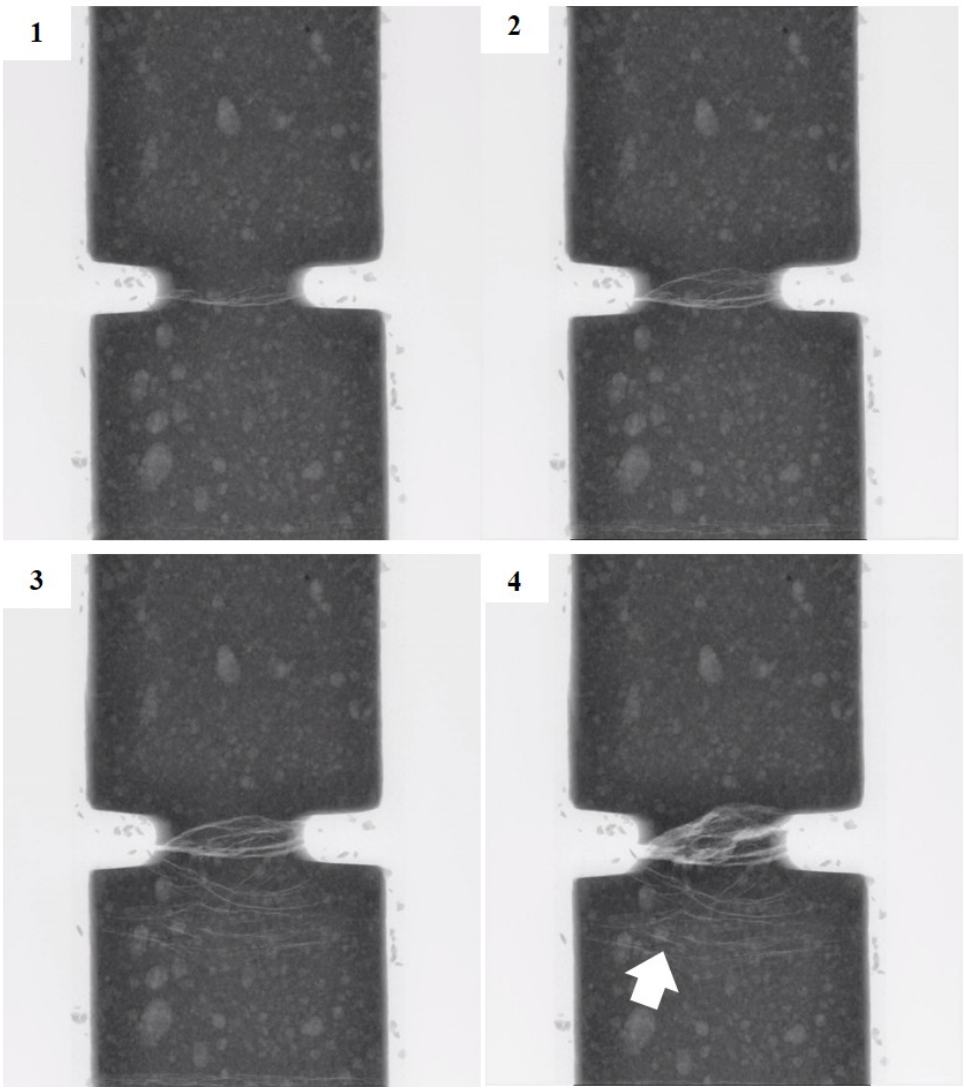

Figure 5.7: Selected 2D X-ray images acquired during a reference tension experiment corresponding to the numbers show in Figure 5.6.

5.3.2
Tension experiments with in-situ microCT scans

The stress-displacement curve of a representative tensile test is presented in Figure 5.8 and 2D slices from the corresponding microCT scans are presented in Figure 5.9. Similar to the specimen presented in Figure 5.6 and Figure 5.7, a micro-crack was detected prior to load application, which explains the shallow initial ascending branch in the stress-displacement curve. However, as in the reference specimen presented in Figure 5.7, the initial crack did not cause failure localization.

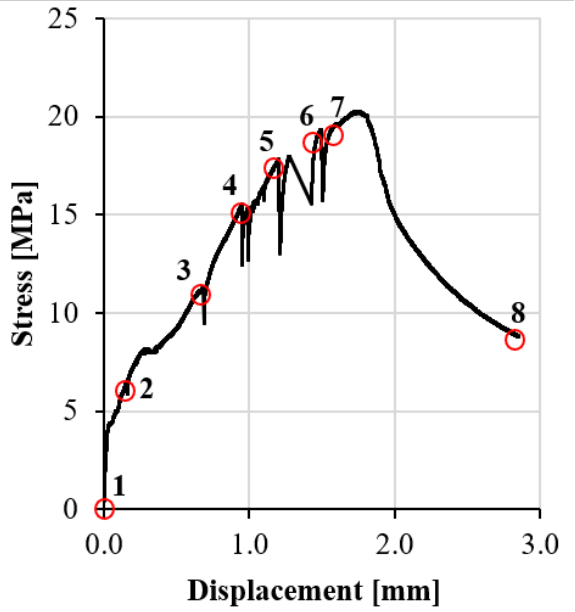

Figure 5.8: Tensile stress-displacement curve of an in-situ microCT test indicating the displacement stages at which the microCT scans were performed. Numbers 1 to 8 correspond to values for which complete tomographic scans were acquired.

The load stages at which the CT scans were performed are numbered and indicated with red circles corresponding to the 2D slices presented in Figure 5.9. The microCT scans were usually performed immediately after crack formation in order to reduce the chance of new crack occurrence during the scanning process. Note that the stress drops included in the red circles do not necessarily indicate crack formation. According to the 2D slices presented in Figure 5.9, new cracks formed only between stages 3-4 and 4-5. Thus, the stress drops corresponding to the red circles result from specimen relaxation during the scanning processes, which took approximately 1 hour each. Despite reaching the same tensile stress as in the reference experiment, the effective deformation of the sample seems to be significantly affected by the loading interruptions.

A DIC or DVC analysis could compensate for this drawback and could as well facilitate the assessment of the stress-opening histories of individual cracks. However, in this paper the potential of DVC will be demonstrated only based on compressed specimens.

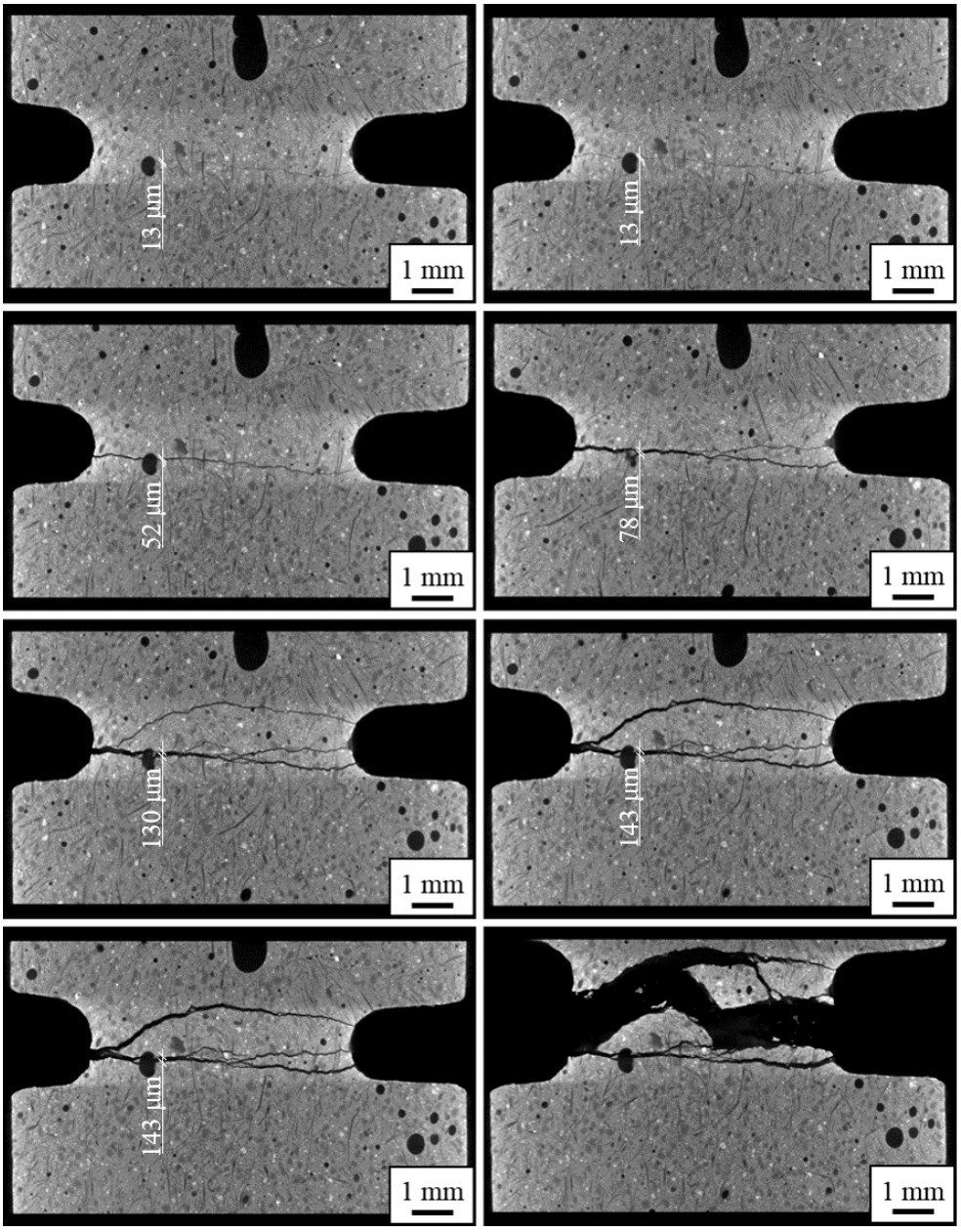

Figure 5.9: Longitudinal 2D slices from 3D tomographic scans of the in-situ tested specimen, showing the crack pattern and growth at different loading stages according to the curve in Figure 5.8.

Besides the analysis of crack pattern and crack growth, the sequence of 2D slices in Figure 5.9 facilitated the estimation of crack openings at specific load stages. Crack opening was derived by counting pixels in the crack at a

certain location by FIJI software. Note, however, that the accuracy is limited by the pixel size of $(13\mu\text{m})^2$. Figure 5.9 shows the crack widths at an arbitrary selected location. An accurate derivation of crack width should be performed by means of Digital Image (or Volume) Correlation. This was, however, beyond the purpose of this study.

A cut-off value was selected on the gray-value range of the pixel intensity histogram (threshold) for segmenting the voids (pores, cracks and background), since these are considerably different from the matrix and sand particles in terms of density and X-ray absorption, as shown in Figure 5.10. The background was eliminated from pores and cracks by performing a subtraction operation of the denser specimen phases from the entire specimen volume/envelope (7).

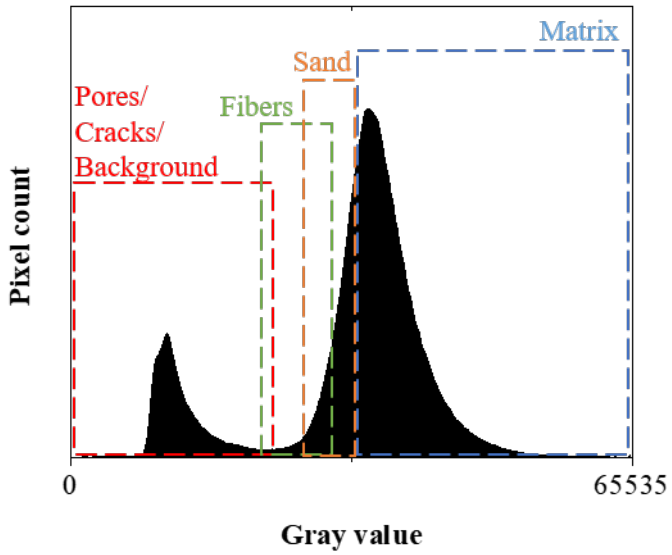

Figure 5.10: Histogram of a 2D slice from a tensile specimen with the pixel intensity range of each phase. The spectrum corresponds to scan nr. 5 in Figure 5.9.

The cracks were represented as a single object, which could easily be separated from the pores. However, since the pixel intensity range referring to voids presents a slight overlap with the range referring to fibers, see Figure 5.10, a few fibers were initially segmented together with the pores, but were subsequently eliminated using shape criteria. The segmented pores and cracks are presented in Figure 5.11. It can be assumed that in the tensile specimens the notches defined to a large extent the fracture processes, the pores having only a secondary role.

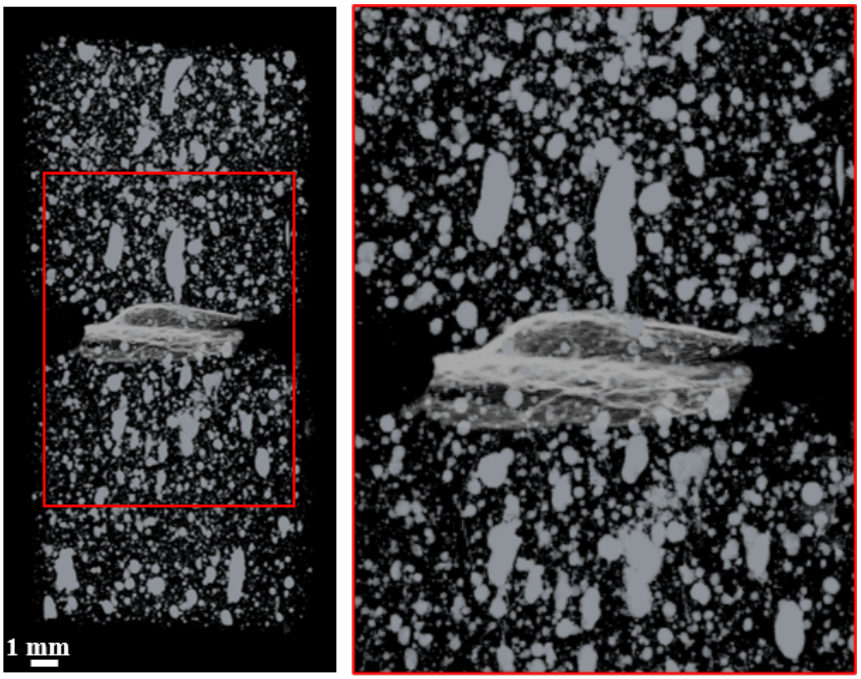

Figure 5.11: Segmented pores and crack in the tensioned specimen at loading stage 5.

The detection and segmentation of pores was carried out in the size/volume range enabled by the resolution of the reconstructed volumes. The voxel size of $(13\mu\text{m})^3$ defined the bottom limit of the segmented pores, meaning that the capillary pores in low micrometer and sub-micrometer ranges cannot be distinguished in these images. While few pores of this kind caused some image noise, pores with equivalent diameter larger than 0.05 mm were considered for pore volume distribution analysis in Figure 5.12. The equivalent diameter was calculated considering the pore as a sphere. The quantitative evaluation indicates that more than 85% of pores were smaller than 0.15 mm, while the largest pore was approximately 1.20 mm in diameter. The calculated volume fraction of pores was 1.8%.

Given that the intensity ranges of fibers are partly overlapped with those of sand particles, it was necessary to apply additional criteria and DL to discriminate fibers and sand. The 3D segmented sand particles and cracks are presented in Figure 5.13, while the 3D segmented fibers are presented in Figure 5.14.

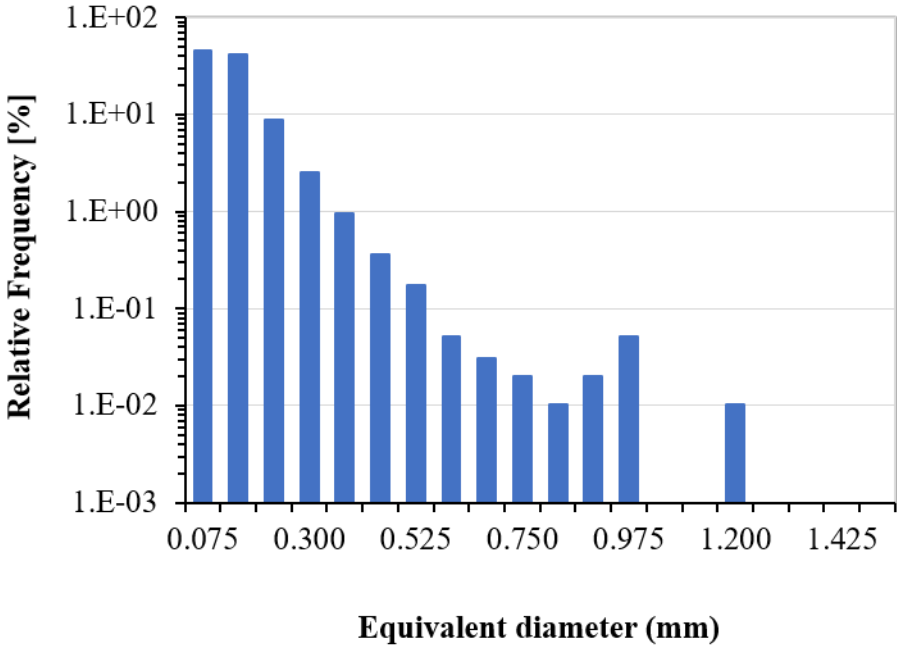

Figure 5.12: Pore volume distribution in the tensile specimen tested in-situ.

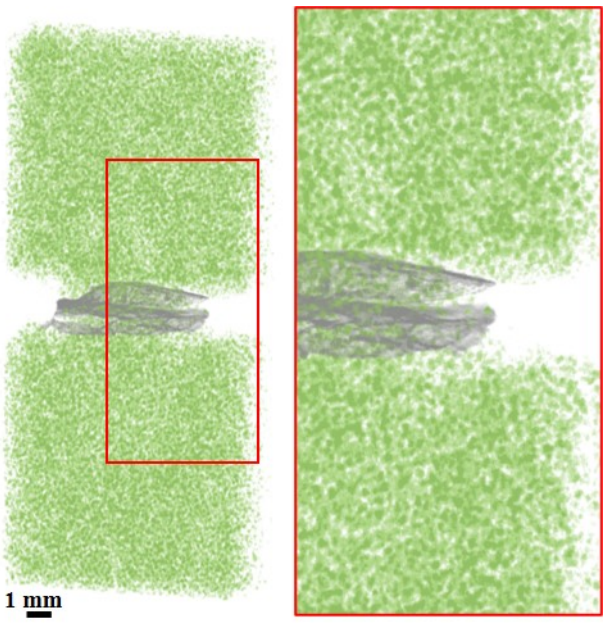

Figure 5.13: Segmented sand particles and cracks in the tensioned specimen at loading stage 5.

The calculated fiber volume fraction in the presented specimen is 2.4%. Note that this derived volume fraction is not representative for the entire donor

specimen but only stands for the local fiber content, which slightly differs from the nominal volume fraction of 2.0 %. Once segmented, each fiber is treated as an object that can be analyzed regarding its orientation. This orientation is given by the angle between the major axis of an object (i.e. fiber) and the transversal XY plane of the specimen, see angle phi – ϕ in Figure 5.15. The z-axis is longitudinal to the specimen and the y-axis is the width of the specimen.

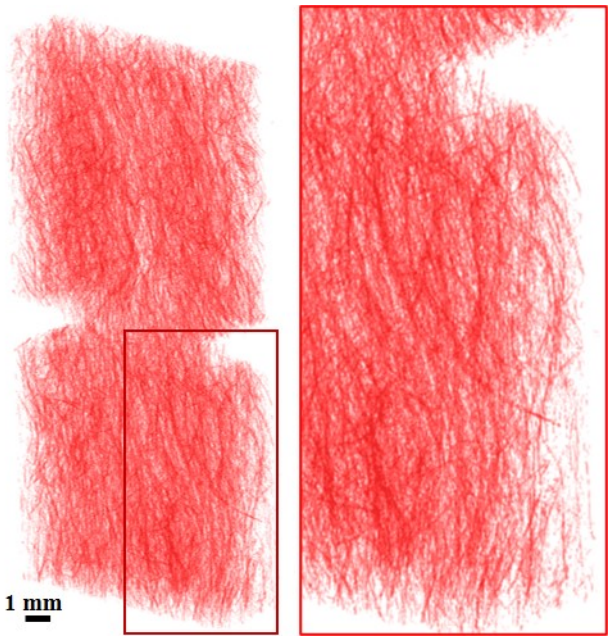

Figure 5.14: Segmented fibers in the tensile specimen at loading stage 5.

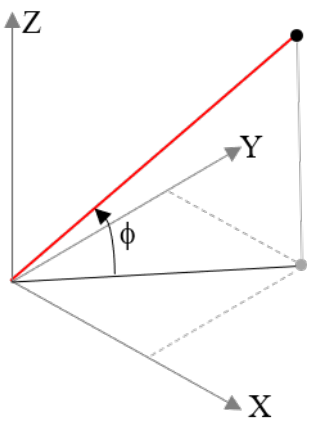

Figure 5.15: Phi angle – schematic representation.

The results from the analysis of the inclination angle are presented in Figure 5.16. The relative frequency is represented by the blue bars and the cumulative frequency is represented by the orange line. Obviously, the fibers show a predominantly longitudinal orientation with regard to the loading direction (Z axis), which is a result of the production technique of the thin specimens, as described in the previous work (9).

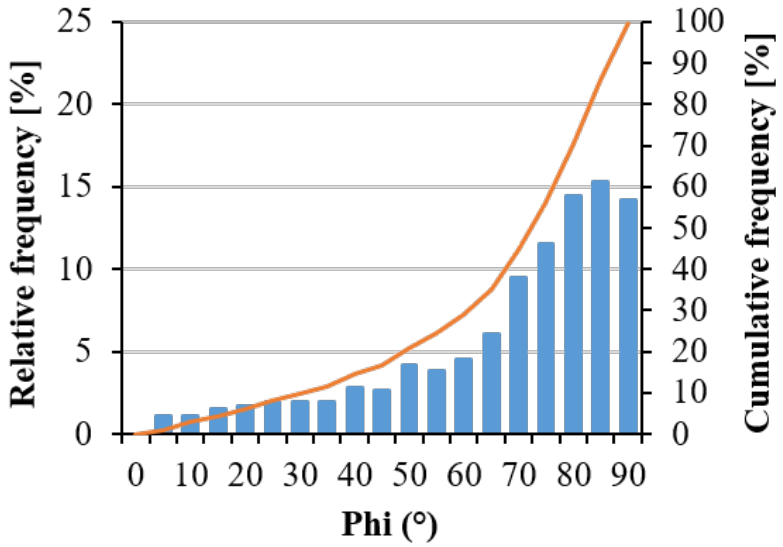

Figure 5.16: Phi angle distribution as quantification of fiber orientation in a tensile SHCC specimen.

5.3.3 Compression experiments with in-situ 3D X-ray scans

The segmentation methodology of the constitutive phases in the specimens intended for compression tests was identical as for the tensile specimen. Figure 5.17 shows the scanned volumes of two specimens intended for compression tests. One specimen was extracted in the longitudinal direction from the original dumbbell-shaped specimen (M-PE-Long), while the other was extracted in the transversal direction (M-PE-Trans). Without a quantitative evaluation of fiber orientation, it is obvious that the fibers exhibit mainly a unidirectional orientation. Depending on the extraction direction, in the first specimen they are oriented longitudinally according to the loading direction, while in the second specimen they are oriented transversally.

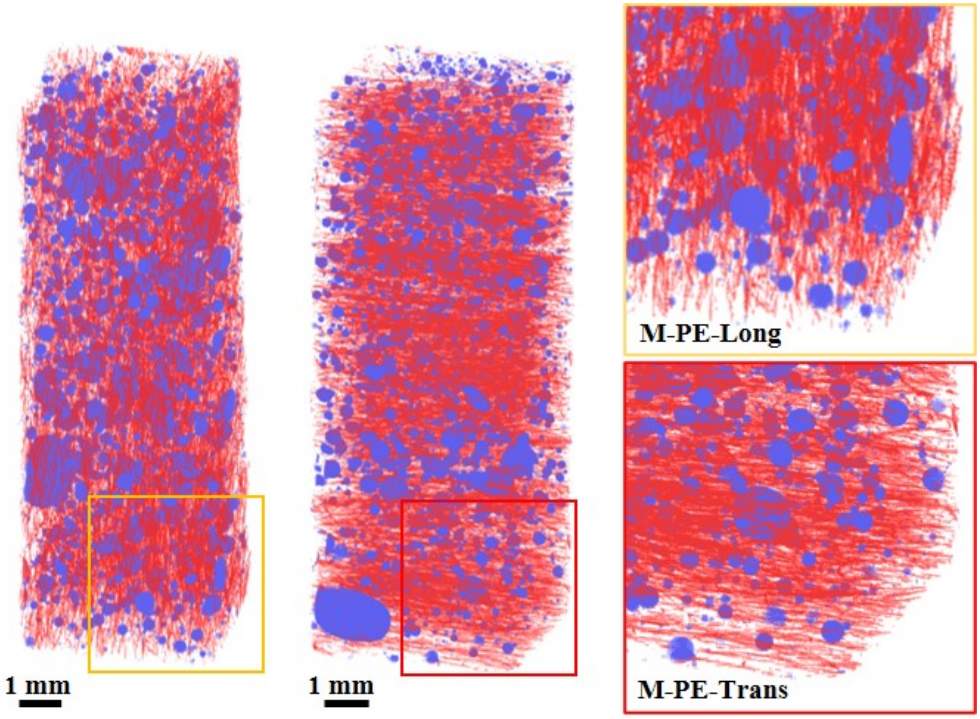

Figure 5.17: Segmented pores and fibers in two compression specimens with different fiber orientation.

As in the case of the tensile specimen, the fiber orientation was quantified according to the angle ϕ (i.e. relative to the transversal plane in the specimens). Figure 5.18 shows that the fiber orientation in the compression specimens is even more unidirectional than in the tensile specimens. The fiber volume content in M-PE-Long was 1.8 % while in M-PE-Trans it was 2.4 %. Same as for the tensile specimen, the different values of fiber content indicate a non-uniform fiber distribution in the donor specimens.

A simple visual inspection of the images in Figure 5.17 suggests that the amount of larger pores in M-PE-Long is apparently higher than in the M-PE-Trans specimen. This is confirmed by the pore size distributions presented in Figure 5.19. In both cases more than 90% of the pores are smaller than 0.15 mm diameter. However, in M-PE-Trans the maximum pore diameter reaches a value of 0.83 mm, while in M-PE-Long the pore diameter reaches maximum values of 1.43 mm^3. Nevertheless, M-PE-Trans yields a higher porosity compared to M-PE-Long, 3.1% versus 2.7%. Note that these miniature specimens were extracted from the same donor specimen and the differences in porosity and fiber content among them only indicate the variation of these parameters throughout the larger specimens.

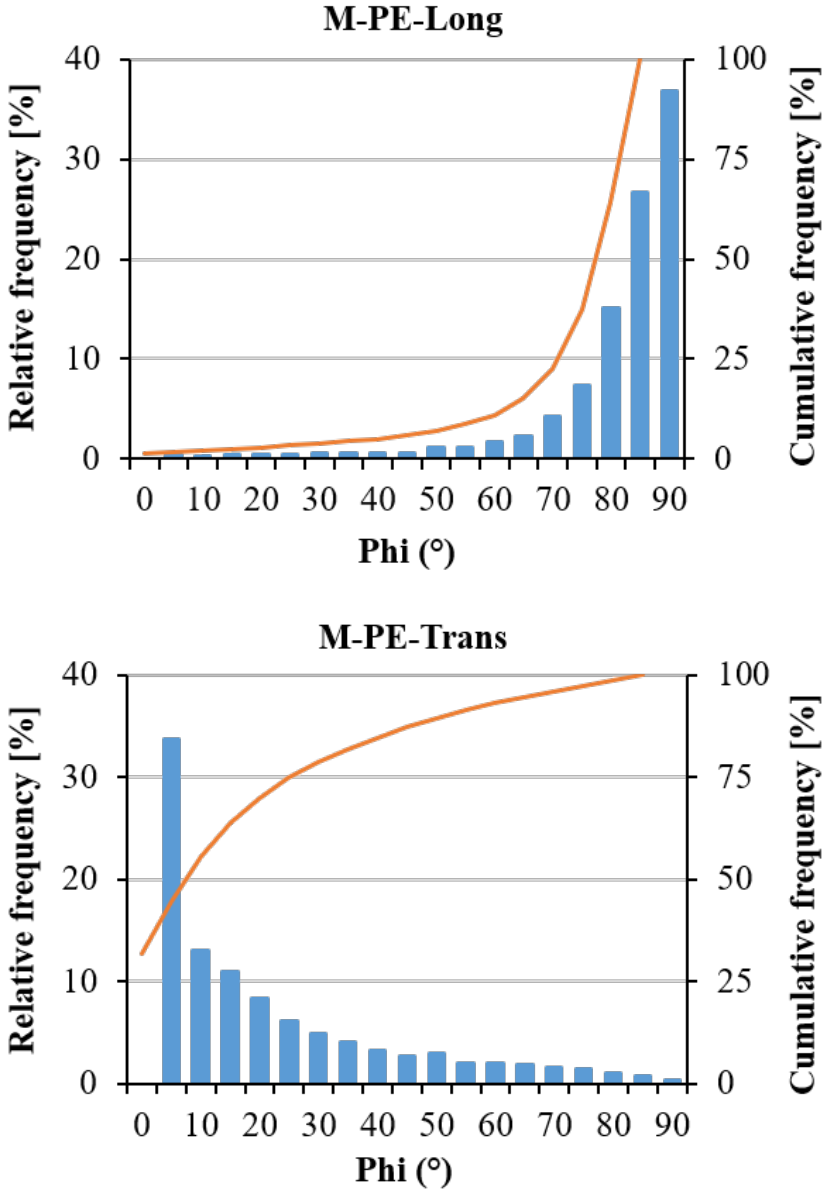

Figure 5.18: Phi angle distribution representing fiber orientation in the M-PE-Long and M-PE-Trans specimens relative to their transversal planes.

In the mechanical experiments, the force-displacement histories were provided directly by the testing rig. The compressive stress-displacement curves are presented in Figure 5.20. The curves correspond to M-PE-Long and M-PE-Trans specimens indicating also the load stages at which the displacement increments were stopped for performing the X-ray scans, which took approximately one hour each. The equivalent peak forces in the presented experiments were approximately 2.6 kN. Given the relatively high loads sustained by the compressed specimens, the compliance of the testing device had a significant influence on the apparent specimen deformation, given that the peak load was attained at a displacement of 0.4 mm. Furthermore, similar

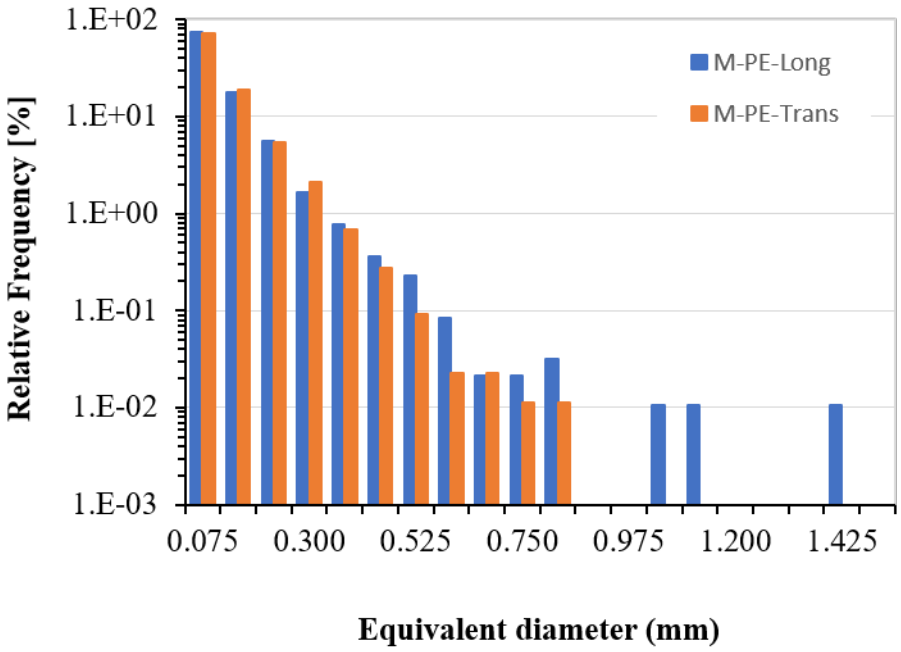

Figure 5.19: Pore size distribution in M-PE-Long (blue) and M-PE-Trans (orange).

to the tension experiments, pausing the loading process at certain load levels resulted in progressive load drops until displacement re-initiation, which is especially clear in the ascending branches of the curves. Nevertheless, the miniature specimens yielded a compressive strength of approximately 110 MPa, which have the same order of magnitude as the values obtained on large cylindrical (140 MPa) (14) and cubic specimens (134 MPa) (18). Note that the performed experiments do not form a representative statistical basis for an accurate evaluation of the mechanical properties of the composites under investigation. However, it will be shown further in this section that certain geometric features of the specimens and the strong effect of the pores at this small scale could be the main reasons behind a somewhat lower compressive strength values as in the previous studies on the same SHCC.

Representative 2D slices from the tested specimens corresponding to the loading stages indicated in Figure 5.20 are presented in Figure 5.21. Four 3D scans were performed during each experiment, the first scan being performed prior to load initiation – Step 0, while the second was performed during the ascending stage – Step 1, see Figure 5.20. Already at Step 1 at an approximate stress level of 70 MPa, multiple micro-cracks formed over a significant height.

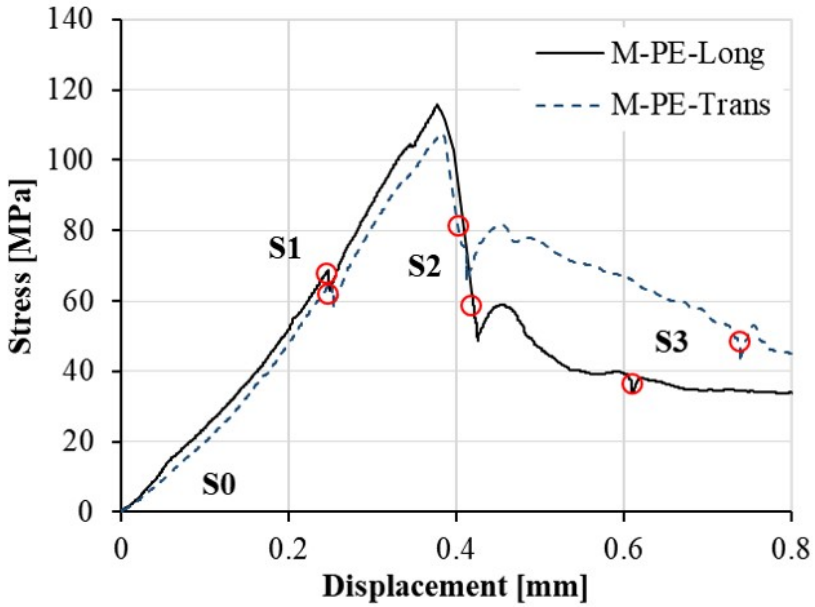

Figure 5.20: Stress-displacement curves from the compression experiments indicating additionally the stages at which the microCT scans were performed.

Despite this, both specimens could be further loaded until approximately 110 MPa. The scans in Step 2 were performed immediately after the peak. At this stage, not only the crack length but also the crack openings are significant. More than that, the post-peak region is characterized by mixed crack opening with a significant shear component in the crushing zone.

Digital Volume Correlation (DVC) was performed using the Vic-Volume software. Given the low time resolution of the performed scans and the rapid and pronounced damage development starting with Step 1, the evaluation on both specimens was only performed based on Steps 0 and 1. The entire volume of the specimens was selected as an area of interest in the DVC analyses.

The results of the DVC evaluations are presented in Figure 5.22. The 2D image used to present these results was the same slice presented in Figure 5.21 (S0). The compressive strains along the Z-axis are represented in the top images, all with negative sign. The bottom images present the positive transversal strains. The DVC evaluations captured clearly the strain concentrations around the pores, which subsequently led to fracture localization.

Note that the displacements at Step 1 were approximately 0.25 mm; see Figure 5.20, which should correspond to an equivalent strain of 0.017 [-]. However, the highest strains yielded by the DVC in the longitudinal direction were approximately 0.010 [-], indicating the considerable compliance of the testing device and the adjacent assembly, such as the load inducing elements.

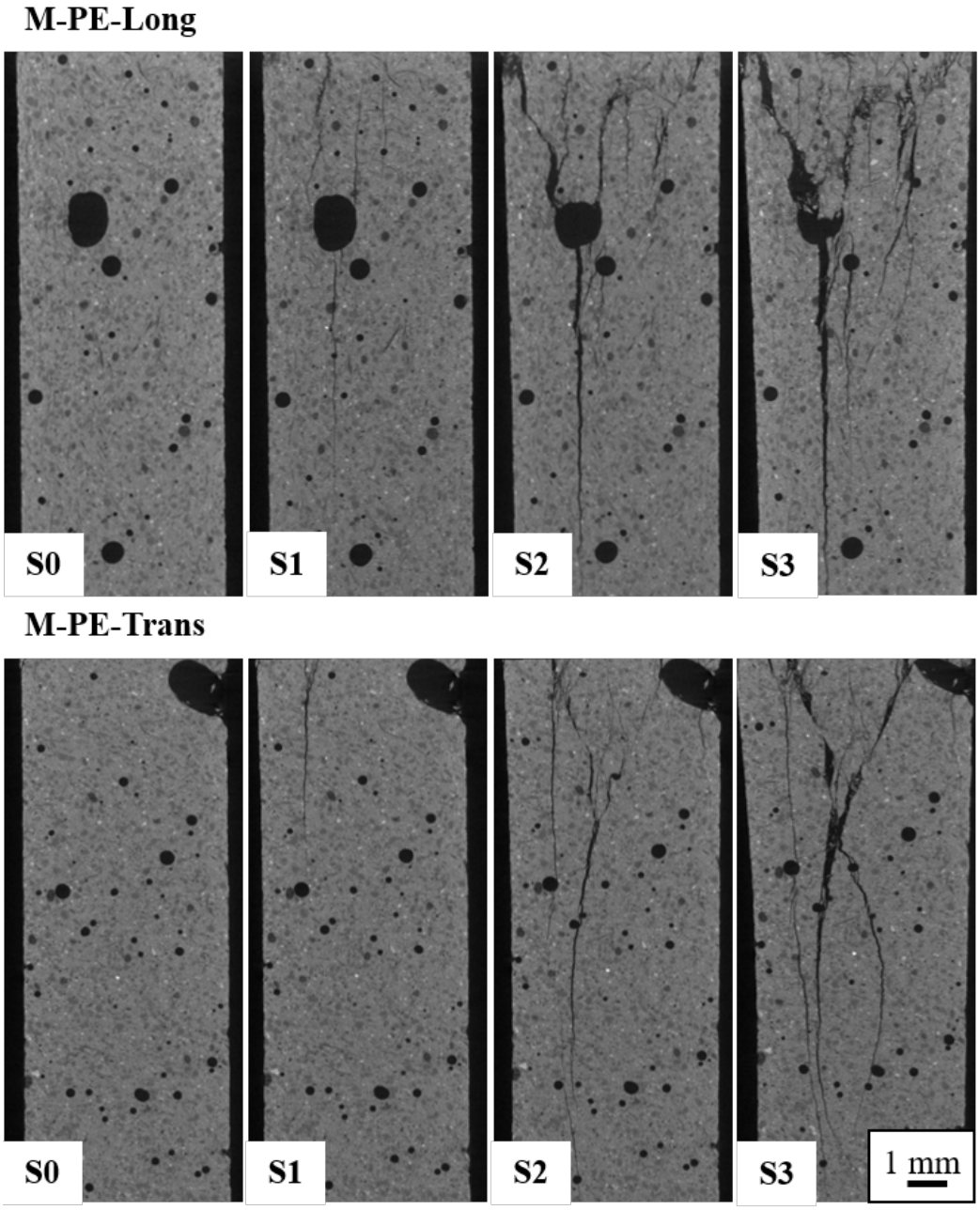

Figure 5.21: Sequence of CT scans of M-PE-Long (top) and M-PE-Trans (bottom).

Figure 5.23 presents that the DVC evaluations captured the apparently eccentric axial loading in the specimen, this being a result of a non-parallelism of the specimen faces. This inexact geometry leads to the formation of a crack, see Figure 5.21 in S1. Subsequently, in S2, another crack forms from a large pore. Finally, it is noted in S3 that the fracture occurs due to the joining of these two cracks.

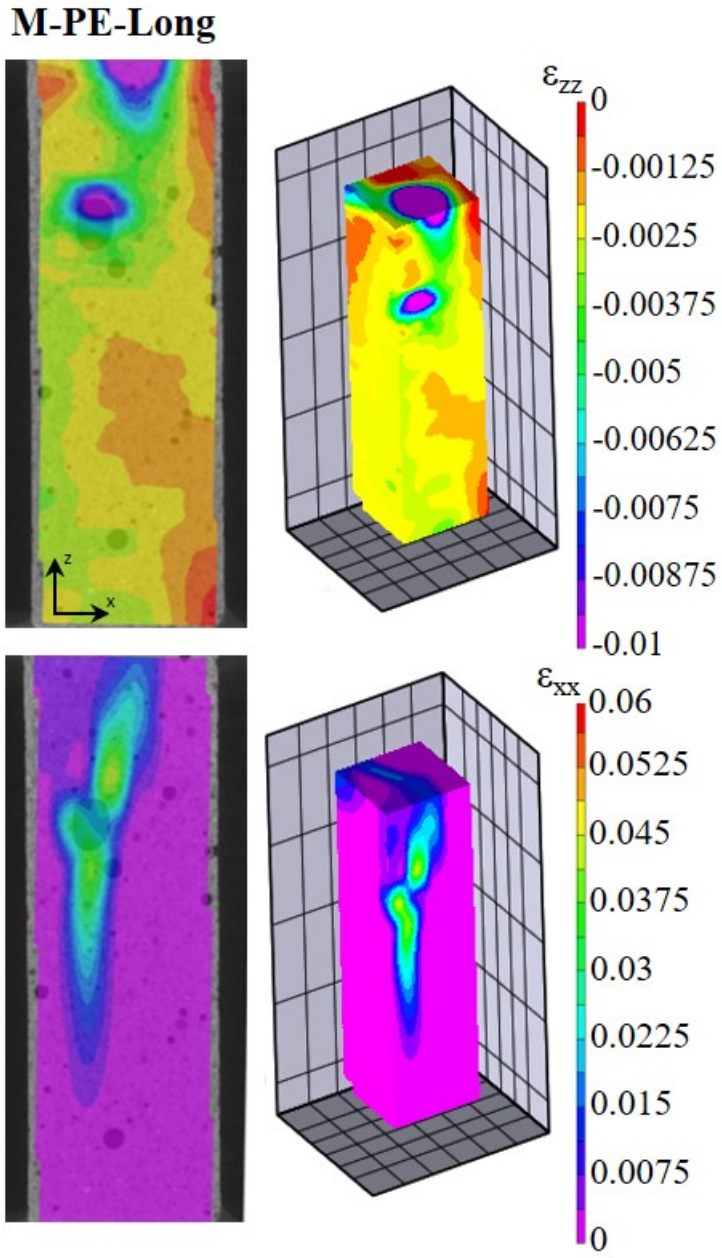

Figure 5.22: DVC analysis of the strain distribution in M-PE-Long at the pre-peak loading Step 1 adopting the pre-loading Step 0 as reference. Strains along Z-axis are represented in the top images and the transversal strains along X-axis are represented in the bottom images.

Considering the similar peak forces of the tested specimens in conjunction with their different pore content and size distribution, fiber content and orientation as well as non-uniform loading, it becomes obvious that these parameters have concurrent effects and their individual influences can be only assessed based on an extensive experimental series involving additionally specimens without fibers. Also, as shown in Figure 5.13, the sand particles

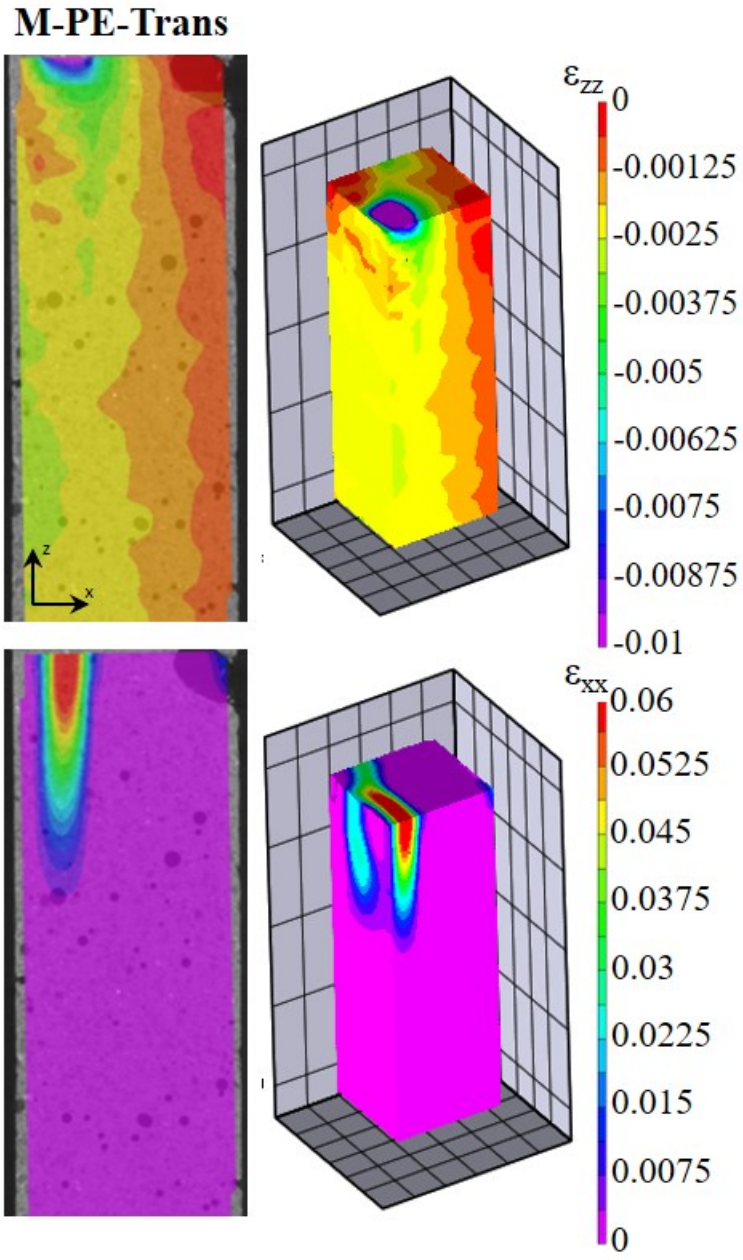

Figure 5.23: DVC analysis of the strain distribution in M-PE-Trans at the pre-peak loading Step 1 adopting the pre-loading Step 0 as reference. Deformation along Z-axis is represented in the top images and the transversal deformations along X-axis are represented in the bottom images.

are considerably smaller than the larger pores and they are also uniformly distributed. Because of this, numerical simulations of SHCC at this scale can imply a homogenized matrix without an explicit discretization of aggregates.

Additionally, it should be mentioned that DVC was also applied to the tension experiments. On one hand, as opposed to the compression tests, the

low strains prior to fracture did not allow for an accurate strain mapping. Furthermore, in the tension experiments the notches determined the fracture zone and the cracks exhibited a steady-state growth. On the other hand, in the compression tests the strains prior to fracture were significant, the cracks propagated gradually and they originated around the pores.

5.3.4 Conclusions and outlook

A high-strength strain-hardening cement-based composite (SHCC) was experimentally investigated in a combined mechanical-morphological framework. The tension and compression experiments were carried out on specially prepared miniature specimens in a testing rig integrated in an industrial computed microtomography. The small specimen dimensions enabled a high resolution of the 3D reconstructions and, in this way, also a detailed three-dimensional representation of their morphology in terms of pore content and size distribution, fiber content and orientation, as well as distribution of fine sand particles. The constituents' discretization involved an advanced segmentation technique based on DL.

The specimens tested in compression were additionally evaluated using Digital Volume Correlation for mapping and quantifying the corresponding strain fields and fracture initiations. The DVC analysis demonstrated the influence of pores on strain concentration and fracture localization, but also highlighted the effect of imperfect specimen geometry on the load distribution in the specimen cross-section.

It was demonstrated that such a combined analysis delivers considerably more information compared to the traditional micromechanical experiments solely by highlighting the pronounced heterogeneity of SHCC at the micro-level and by relating it to the composite mechanical behavior.

However, at this scale of observation, the effect of notches and pores appeared to be decisive on the fracture localization both in tension and compression. At larger scales of observation, it could be expected that the effect of such defects would be smeared by other features of statistical or structural nature. For generating more representative data, the experiments should be performed on larger specimens, which would require a different testing rig and possibly SHCC compositions with lower strength. This should be, however, adjusted based on the purpose of the investigation, since larger specimens

will lead to a lower scan accuracy (i.e. larger voxel size) and will impair the possibility of segmenting the finer constituents, such as fibers.

Moreover, the scanning duration should be reduced in order to limit relaxation effects and allow a higher time resolution of the microCT scans. For a more detailed analysis of crack formation and propagation, considerably smaller scanning intervals and lower displacement rates should be considered.

For assessing the crack bridging action of the fibers in compression as well as the effects of fiber distribution and orientation on the compressive behavior of the composites at the micro-scale, a larger tests series is required involving specimens with and without fibers.

Finally, the microCT in-situ methodology should be assessed regarding its potential in monitoring and quantifying active deterioration mechanisms in the specimens, e.g. at elevated temperatures, both with and without mechanical loading.

6
Digital Volume Correlation analysis of the tensile behavior of strain-hardening cement-based composites (SHCC)

6.1
Introduction

Strain-hardening cement-based composites (SHCC) are fiber-reinforced cementitious materials that achieve significant deformations through multiple cracks formation (30)(31)(18). The fibers act as bridges that block the further propagation of the cracks that previously occurred in the matrix. This means that will occur a multiple cracks formation before the material fails. Thus, the deformation of the material is directly linked to the amount of formed cracks. Moreover, the durability of the material is associated with the width of these cracks, since cracks allow water and chemicals to penetrate (1). As the crack opening behavior is strongly related to the macro behavior of the SHCC, meaningful studies have used digital image correlation (DIC) technique to measure the crack opening during tensile loading (14)(137)(138)(139). In this scenario, DVC appears as a powerful solution in the case where cracks can be analyzed in 3D throughout the interior of the specimen.

DVC is a technique that estimates full-field strain in 3D over the entire length of the specimen by correlating imaging volumes of the specimen in unloaded and loaded states (140). Shortly, it can be elucidated in three main steps sequence: acquisition of 3D images; use pattern-matching correlation procedure to measure a displacement vector field; calculation of the strain field from the displacement measured (61)(62). Advances in 3D image acquisition allowed DVC to gain ground as a strain mapping method (140). Henceforth, DVC has been effectively used to investigate distinct types of materials (63)(64)(65)(66)(58) and correlation codes have been improved to estimate more accurate displacement vectors (63)(141).

A traditional method for acquisition of volume images is by X-ray microcomputed tomography (microCT), which has been widely used for damage analysis of cementitious materials (127)(71)(7). A testing device combined with microCT is required to obtain sequences of 3D images at different loading

stages, a technique known as in-situ microCT (58)(60)(59). These devices often present instrumentation difficulties, since they are tiny devices that impair coupling of load cells or LVDTs and the results lead to additional deformations from the equipment. Therefore, a local deformation analysis may be more appropriate for such a test.

For cementitious materials, DVC has been commonly used to map internal displacement or strain distribution during in-situ microCT mechanical testing, highlighting local values on damages already detected in the microCT image (58)(142). Some authors detected microcracking estimated as one tenth of the voxel size in lightweight concrete images, detecting early age cracks which wouldn't have been noticed on the microCT images (143).

Given the typical microCT resolution and the size of the crack's width formed in a SHCC tensile test, occasionally minor cracks cannot be identified in the images. Due to this soft internal deformation, a DVC analysis needs a suitable code that can provide relevant information. This chapter focuses on testing suitable DVC free codes for SHCC in-situ tensile test analysis. The tested codes could not predict cracks formed in subsequent loading stages, but they showed relevant results on the mechanical behavior of the material during the tensile test.

6.2 DVCs free codes

Since DVC was required in material characterization research, many codes and software have been developed. Some software may present a friendlier user interface and bring more suitable parameter settings for some materials. On the other hand, for some analyzes, freely available codes can fit the user's needs. In the work at hand, three free codes applied to images obtained from an in-situ tensile test were evaluated and compared: the diamond DVC code; the Fast-Iterative Digital Volume Correlation Algorithm (FIDVC) and the Software for the Practical Analysis of Materials (SPAM).

6.2.1 Diamond DVC

Diamond DVC code was applied in the field of biomechanical systems, more specifically to evaluate musculoskeletal behavior through understanding the mechanical function of a joint. Images in nanoscale were obtained via synchrotron x-ray tomography (sCT) allowing DVC-based strain fields to be

calculated from displacements with an accuracy below 100 nm (141). Diamond code is available in (141) and provided for Linux x64 or Windows. On Windows, the c++ code is run at the command prompt, which reads a simple text file that contains required keywords and parameters. Three existing inputs are required: a reference and correlated (deformed) image in a single uncompressed raw data file and the point cloud name of tab-txt nxyz file. The latter is a file containing data for all measurement points in the Region of Interest (ROI). In which, n is a number for the point and x y z are the coordinates of the corresponding points in the image. Also, a base output file name for results of code execution is required.

A description of the voxel data files that are targeted for analysis are defined, such as the bit depth and the geometry of both reference and correlated input image volumes.

Afterward, one must define the geometry and size of the subset (subvolumes) around each search point, defining the subset on which pattern matching correlation will be applied. The traditional geometry used in the subsets of the DVC codes are cubes. Also, the number of interpolation points within each subset needs to be defined, and the reference image volume is used to establish templates with arbitrary point locations. For cubes, a uniform grid is generated. This parameter is strongly related to computation time.

Finally, required parameters for the default optimization process such as expected maximum displacement, degree-of-freedom set for the final stage of the search, objective function and interpolation method have to be defined in the text file.

The results are provided in a text file containing the coordinates of the displacement u, v and w for each nxyz point.

6.2.2 FIDVC

The other code used in this work is available on GitHub of "Franck Laboratory - Cell mechanics & soft materials" and called Fast Iterative Digital Volume Correlation Algorithm (FIDVC) (144). It is a MATLAB code, that determines the 3D displacement fields at low computational cost. Even though being CPU-based, it does not require extreme computational effort and can be easily run on conventional computers in a non-exorbitant time.

FIDVC is a 3D full-field measurement technique for determining large deformation internal displacement fields in soft materials and to validate it an example based on simulated deformation fields was performed. A zero-strain deformation of a polyacrylamide hydrogel embedded with 0.5 micron-sized fluorescent particles was experimentally acquired by laser scanning confocal microscopy (LSCM) and then rigidly translated by 4.4 voxels along one direction through simulation (145).

The technique utilizes a classic fast Fourier transform (FFT) based cross-correlation formulation in conjunction with the iterative deformation method (IDM). The IDM warps the reference and deformed images by an incremental displacement field ($u = (u_1,u_2,u_3)$) until they reach the same final configuration. This configuration is estimated in terms of the cross-correlation coefficient ($C(d_u)= \sum_{x=\frac{-L}{2}}^{\frac{L}{2}} f(x).\widehat{f}(x + d_u)$, in which $f(x)$ is a function related to the gray level intensity values of the reference and $\widehat{f}(x)$ of the deformed image). In each iteration, a convergence criterion based on the normalized sum of squared error is performed and the code stop when the error is less than the defined threshold error. So, the displacement field is determined by the last iteration calculated. In this code the user needs to provide the reference and deformed 3D images saved in a three-dimensional matrix (intensity values are stored at x, y and z position) in .mat files. These files names, such as the output file are defined in the main run code. Also, in the main run file the user can change the default subset size. The step size is determined by a file called dm.mat contained in the path, that can be easily changed by the user as well. The results are provided in three 3D matrices, corresponding to the u, v and w displacements.

6.2.3 SPAM

The calculation of displacements by SPAM is quite similar to Diamond. Both use the sum of square differences as the error function of differences between loaded and unloaded specimen images. SPAM uses Newton optimization to iteratively find the minimum of the error function by small increments on the deformation matrix. Diamond code minimizes the error function by the Gauss-Newton method, which is an iterative algorithm to solve nonlinear least-squares problems. SPAM linearizes the error function using the Taylor expansion, in order to simplify the computation of the gradients. On the other

hand, Diamond does not mention linearization in (141), and due to the closed code it is not possible to know if linearization is performed.

SPAM is a Python package containing a series of toolkits for handling and correlating 3D fields for applications in material science/mechanics (67). The first step uses a robust registration tool based on (28)(29) with some cutting edge tools from (146). This step generates a tsv file that contains information regarding a registration of the images before and after the deformation. This tsv file, in addition to the tiff of un- and deformed images, will be required in the next step.

The following step involves running the script that calculates the displacement. As in previous codes cited in this work, the user can set the step size and the subset. This calculation is basically done by minimizing the error function, which is the classic sum-of-squares difference between the un- and deformed images. The SPAM displacement script improves the previous work of (29), that searched the space of displacements, rotations, etc. making small steps to decrease the error. The incremental (147) approach for image correlation was implemented. The results of this step are a sequence of tiff images, in which each pixel contains a displacement information of each point calculated.

Once the displacement gradient fields are determined, either infinitesimal or finite strain values can be computed from it. The SPAM code advantage is that it provides the strain calculation, supported by basic notions of continuum mechanics. Continuum mechanics is based on the calculation of the transformation gradient tensor (F), in which the strains are computed based on a local variation in a displacement field relative to the neighbors' points. SPAM uses a Q8 shape function linking 8 neighboring nodes. The strain can be calculated in a general framework known as large (finite) strain theory. However, if the calculated displacements are much smaller than any dimension of the sample, an infinitesimal strain theory can be used. In this work, a small strains framework was assumed. The results were provided as a sequence of tiff images.

6.3 Results and discussions

The image sequences were obtained from an in-situ tensile microCT already presented in the authors' previous work (chapter 5) (10). The reference microCT, step 1, was performed with the unloaded specimen. In the subsequent steps, the tensile test was stopped at relevant points of the stress-strain curve

and microCT was performed. From the eight microCT sequences shown in (10), steps 2 and 8 were excluded. This is due to the fact step 2 does not present relevant internal deformation, and step 8 represents the failure of the material. Thus, the present work will analyze 6 step sequences.

First, all volumes were aligned using the dataset registration tool in Dragonfly software (Object Research Systems, Montreal, Canada). This procedure automatically registers datasets by applying the scaling, rotations, and/or translations required to match features between two datasets. Thus, steps 2 to 6 were registered using step 1 as a fixed dataset. A parameter available for registering datasets is the "use a fixed mask", which restricts the calculations to the defined 3D region. Since the loading is carried out by pulling one side of the specimen, on the opposite side the mask was set in order to align the images according to the least deformed volume in the specimen. The calculation was performed using linear interpolation, that considers the closest 2x2 neighborhood and then takes a weighted average of the four pixels to arrive at a final interpolated value, and the registration metric used was "mutual information".

Also, in the Dragonfly software, all volumes were cropped to reduce computational effort during DVC processing. Thus, the new datasets were extracted from the same clip box, which was determined to cover the entire crack formation up to step 6. The size of the images should fit some requirements of the DVC codes tested. Moreover, as the goal was to compare the three codes, results using the same parameters applied in the same points in the image should bring a more accurate analogy.

In order to run the Diamond code, it is required that the cloud points are internal to the image to prevent the subset from exceeding the edges. The first point calculated in the FIDVC code is on the first voxel of the image and in the SPAM is one step size into the volume. Therefore, it is important that the input image sizes are divisible by the step size (8 voxels), so that the border points calculated by the FIDVC/SPAM could be eliminated and the internal ones would match the points calculated by the Diamond code. Furthermore, the FIDVC code requires that the size of the input image should be divisible by 0.5 times the size of the subset. The subset used was $(32 \text{ voxels})^3$. Taking notice of these issues and in order to facilitate the next steps, the cropping was performed resulting in 6 datasets with 224 slices and 336 x 336 pixels each one, see Figure 6.1

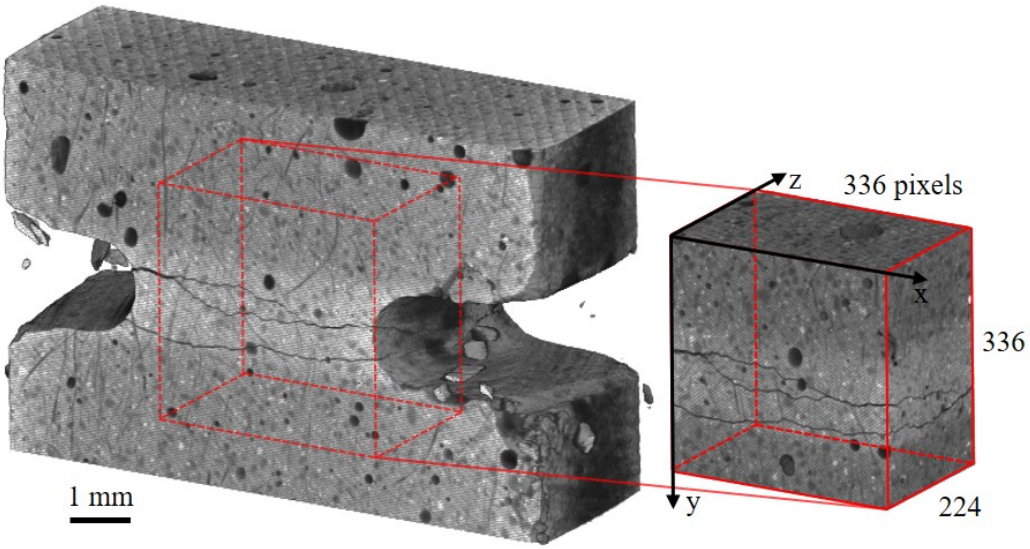

Figure 6.1: Red highlights a cropped volume used as input for the three DVC codes tested with the origin of the X Y Z axis. Yellow highlights the 2D section to be analyzed.

As the resulting datasets had no background, the point clouds of the ROI set for the Diamond code could be chosen uniformly, and were generated with a step of 8 voxels. However, the point clouds were restricted to 32 voxels from the surface to avoid surface edge effects during the correlation process. This resulted in 25725 points uniformly distributed in the ROI. The subset size was defined as a 32 voxels edge cube, and 5000 points to distribute within the subset.

In the FIDVC code, there are no point clouds previously defined. Those are created from image size and step size inputs. The result are 3D matrices of 43x43x29. After that the edge values were eliminated in a way that the final matrices were 35x35x21. This procedure means the same 25725 points defined for the Diamond code. SPAM generated 27 sequences of 41x41 pixels image, which were then also cropped to create in 21 sequences of 35x35 pixels images, that is the same 25725 points analyzed by the two other codes.

The three DVC codes were processed five times with inputs from two subsequent steps. First, step 1 was defined as a reference (non-deformed) image and step 2 as a deformed image. In the last "run" the reference and deformed images had steps 5 and 6, respectively, as input. It was performed in this way to avoid the code getting lost when searching for the corresponding subset since non-subsequent steps could present huge deformations. Furthermore,

displacement vectors could be summed to obtain the accumulated steps' displacements if this information was required.

To facilitate the visualization and analysis, all results were plotted in 2D overlapped on the final loaded dataset input in the Dragonfly software. This means that, for example, the displacement or strain calculated from step 1 to step 2 was overlapped on the step 2 dataset. Figure 6.2 shows the plotted y-axis displacements results of Diamond, FIDVC and SPAM codes, in which the same scale range was defined, from -4 to 2. The measurements of the displacements are given in voxels.

The results of three methods were consistent. However, FIDVC code presents more precise displacement details within the SHCC microstructure, such as greater deformations concentrated in pores, which cannot be distinguished by the Diamond and SPAM codes. On the other hand, as they provide a more generic analysis, the Diamond and SPAM code indicate the existence of a non-uniform tensile strain in the y-axis direction. Given that the y-axis grows downward, negative values mean tension. Thus, since the first sequence of steps, the Diamond and SPAM code results present higher displacement on the upper left of the specimen, which becomes more prominent in subsequent steps. It may indicate a torsion in the specimen during the test, that could be confirmed analyzing other axis displacements, as the x and z-axis that will be investigated in the following. In the last step (displacement 5-6), this non-linearity in the y-axis does not occur anymore. At this point, the larger and uniform displacements above the top crack and the smaller and uniform displacements below it become evident, suggesting that this crack will open until the material fails.

Displacement values obtained by SPAM and Diamond were quite similar. The displacements from step 3 to 4 obtained by SPAM were plotted in the open-source software ParaView (148). The displacements are represented by arrows that start at the points set for the calculation (in step 3) and point to the direction that these have moved (in step 4). For better visualization, only 4.500 of the 25.725 calculated points were plotted and the arrows were scaled by a factor of 6. The top part of Figure 6.3 presents these arrows colored according to the magnitude of the displacement vector, in which the trend of internal displacement is perceived at this stage of the test. Despite being a direct tensile test and displacements just on the y-axis were expected, the arrows point to displacements also on the x and z-axis. Also, it can be seen that the vector sizes are larger in the upper left corner, which was expected

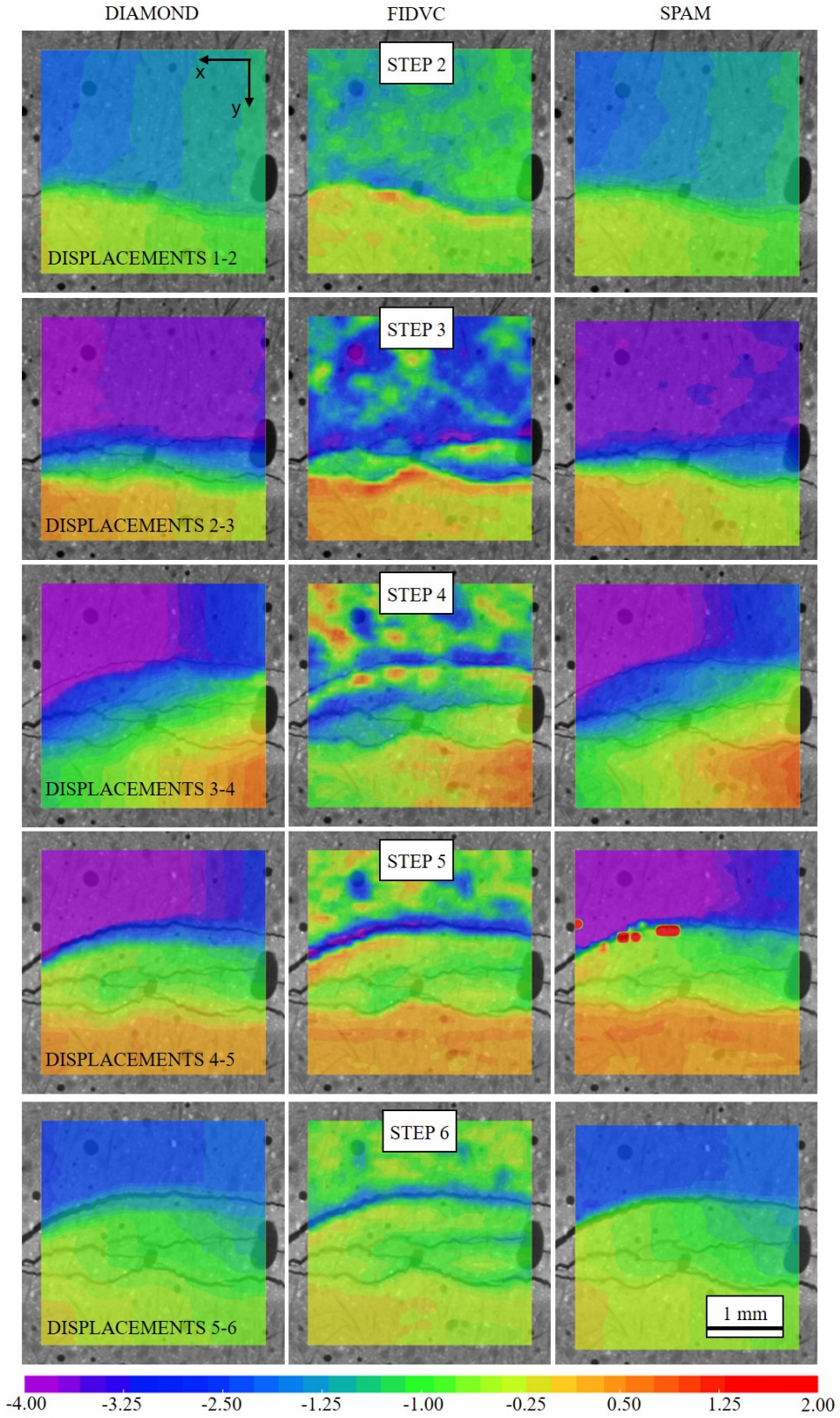

Figure 6.2: Plotted y-axis displacements (in pixel) obtained by Diamond DVC code (left), FIDVC (middle) and SPAM (right) overlapped on the final loading dataset.

since the displacements on the y-axis are more expressive and Figure 6.2 had already shown that for displacements in the y-axis.

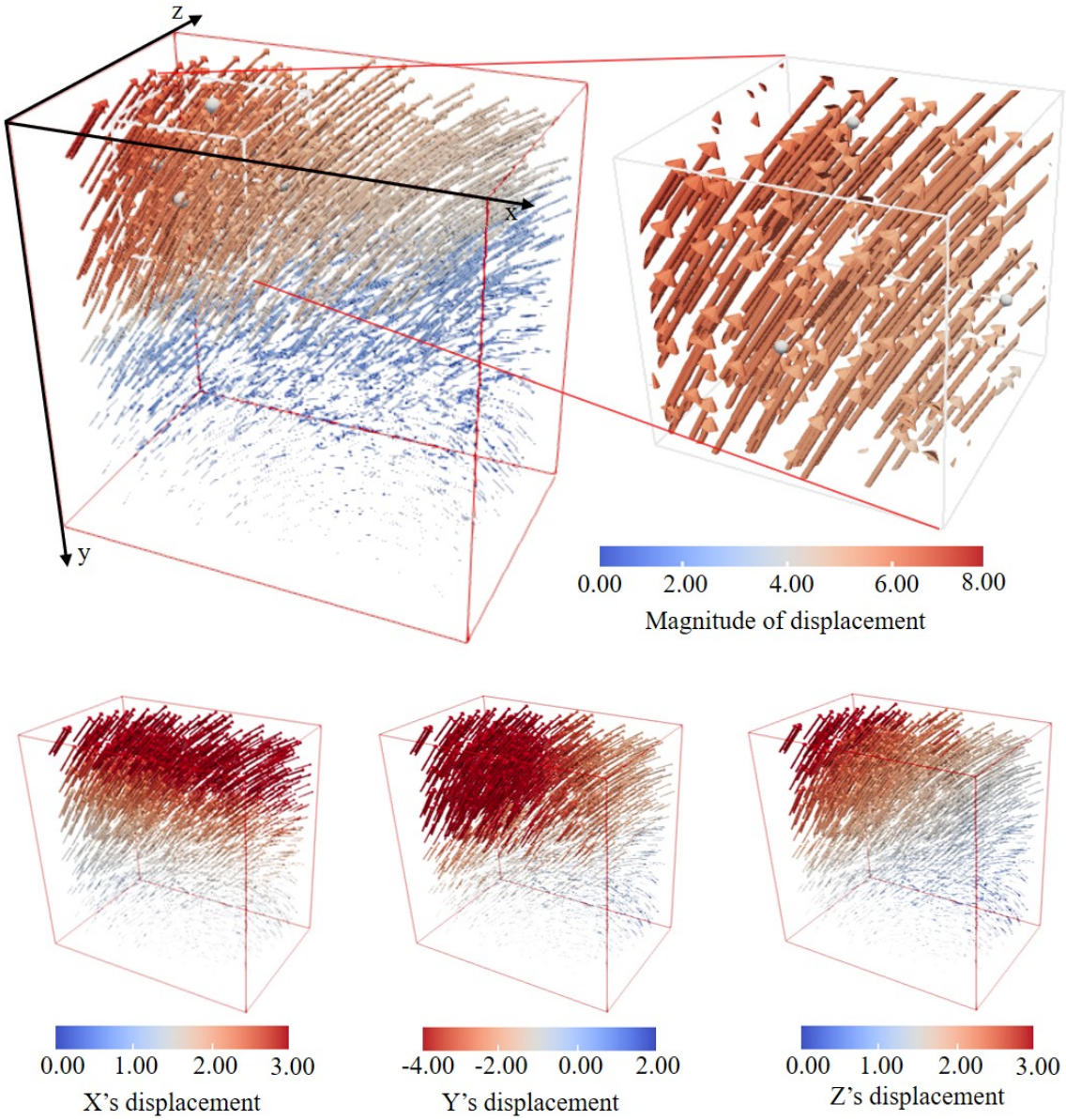

Figure 6.3: Displacements from step 3 to step 4 obtained by SPAM code represented by arrows. Color scale based on the magnitude of the displacement (top) and on each separate axis (bottom).

Due to the displacements occurring in the three directions, plotting vectors with the color scale based on each separate axis can provide relevant information. This is shown at the bottom of the Figure 6.3. The plot with color scale based on x-axis displacement shows that the upper part of the specimen moved in the x-axis more than the bottom part. Color scale based on z-axis

displacement shows that the upper left part has a greater displacement on the z-axis than the rest of the specimen. This was used to check the occurrence of torsion in the specimen during the test.

Once the displacement gradient fields are determined, strain values can be computed. The strain script computed the strain field under the hypothesis of small strains, meaning that for every point in the field the strain tensor e is computed using the Q8 element (67). Figure 6.4 shows these e_{yy} results. The strain calculation brought some interesting information about the crack opening and relaxation. Note in the sequence that until step 3, the first crack formed concentrates greater strain. From step 4 on, when the top crack appears, the strain decreases in the lower cracks, and the strain in the upper cracks becomes more prominent. This means that there is a relaxation in the bottom crack and the strain concentrated in the upper crack, where the rupture occurs. Previous work by the author (10) shows the failure coming from the top crack.

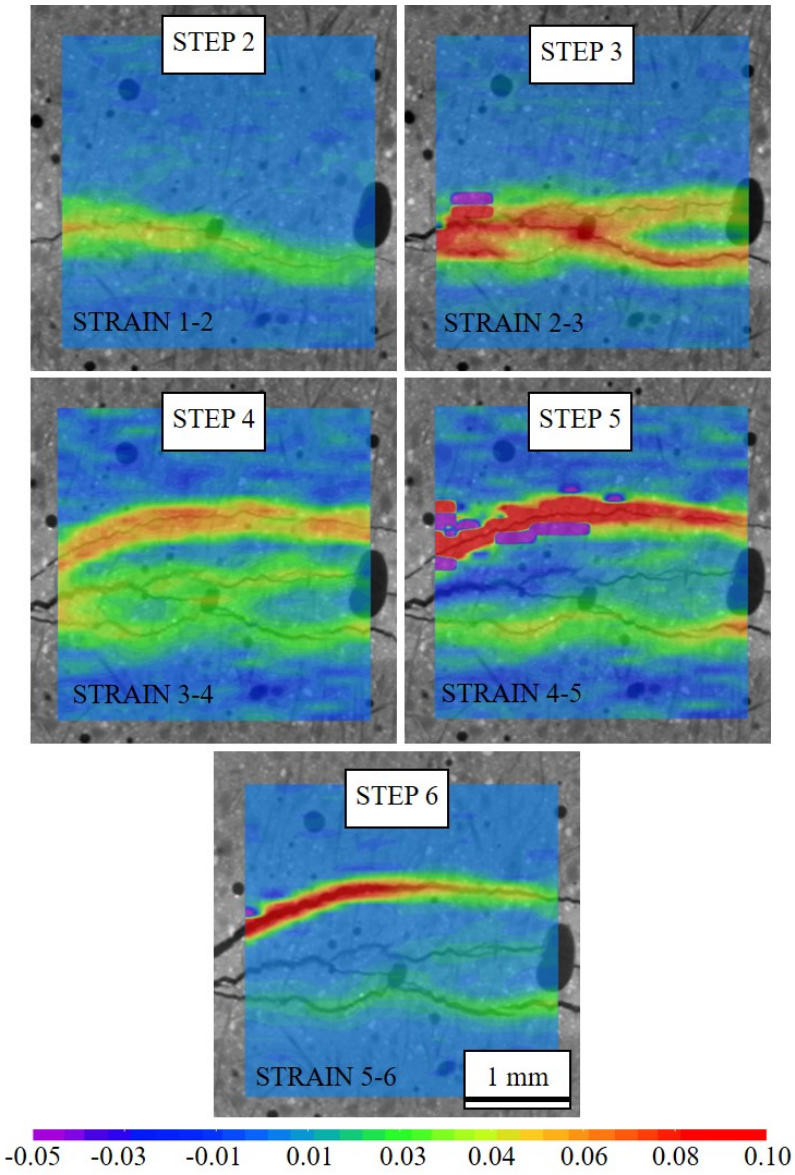

Figure 6.4: Plotted y-axis strain (e_{yy}) obtained by SPAM overlapped on the final loading dataset of each analysis.

6.4 Conclusions

Regarding computational performance, the three codes tested were similar. All of them could be run on a commercial computer with viable time spent, for the image size used (336 x 336 x 224 pixels) and DVC parameters defined in this work.

Comparing the results, the Diamond and SPAM codes presented practically identical displacement results. This is due to the similarity of the calculations used in both codes. FIDVC code presented more detailed information

such as pore displacement concentrations, which cannot be perceived in the Diamond and SPAM codes. On other hand, Diamond and SPAM codes showed crucial information about non-axial displacements, which proved that a torsion occurred during the in-situ test.

The strain result calculated from SPAM code brought information about the crack opening and relaxation during the in-situ test, showing the crack responsible for the material failure at the end of the test.

In a previous work by the authors (10) it was mentioned that DVC commercial code was tried in these tensile experiments, but the results did not allow for an accurate strain mapping like for the compression tests, due the low strains prior to fracture. The codes applied in the present study proved to be more suitable for the analysis of these low displacements. Even though, the DVC results still indicate that the fracture zone was determined by the notches and reveal no relation to the presence of pores, as was evidenced a strain concentration around the pores in the compression tests. Although the FIDVC code proves that there were concentrations in the pores, this was not decisive for the failure of the material in this tensile test. Possibly the influence of the torsion that occurred in the specimen has outweighed the influence of the pores for the failure of the material.

The results also showed a significant difference in the order of magnitude of the displacements obtained by DVC and by the in-situ device (Figure 5.8). This may be related to equipment deformation, which in these tests cannot be resolved by other instrumentation techniques such as strain gages or LVDTs. Therefore, it is important that the deformation analysis of the material is done through techniques such as DVC.

7
Conclusions and future works

Steel fibers and pores within the cementitious matrix were easily distinguished on images obtained by X-ray microtomography. Therefore, segmentation by the traditional thresholding method works well for these two SHCC phases. Hybrid fiber reinforced strain-hardening cementitious composites showed a slight tendency towards the axial orientation of the steel fibers when increasing the PVA replacement amount by steel fibers. Also, when increasing the PVA replacement amount by steel fibers, the porosity decreases. In this work the PVA fibers could not be analyzed.

In smaller SHCC specimen made only with PVA or PE fibers, in which it was possible to obtain a higher resolution, the fibers were segmented through machine learning. The algorithm used was of the deep learning type, and the ideal parameters were successfully determined. PVA and PE fibers were accurately segmented and were quantified in volume and orientation. These networks also identified the pores and sand particles. The pores did not necessarily need to be segmented by deep learning, the segmentation by thresholding is sufficient given the difference in density of the air and matrix phases. The sand segmentation showed that they are uniformly distributed. Also, because sand particles are considerably smaller than the larger pores, numerical simulations of SHCC at this scale can imply a homogenized matrix without an explicit discretization of aggregates.

The results of segmentation by DL were qualitatively evaluated and also compared with the volume fractions actually used in producing the SHCC specimens. However, evaluation metrics, such as error rates and confusion matrix, should be done in further works. For that, a training data needs to be destined for the validation of the results.

From the segmentation by deep learning, the quantification of the SHCC constituent phases could be correlated with their mechanical behavior through an in-situ test. In the sequence of images obtained from the in-situ test, DVC was applied. For compression SHCC tests the DVC analysis demonstrated the influence of pores on strain concentration and fracture localization, and also

highlighted the effect of imperfect specimen geometry on the load distribution in the specimen cross-section. For tensile SHCC tests, DVC showed the loading path that occurred during the test. For example, a displacement tendency in the direction of the non-axial axes characterized a torsion during the test, in addition to the tensile loading.

This work used innovative techniques to present relevant solutions for mesoscale characterization of SHCC materials through processing and analysis of 3D images. The microstructural quantification and its mesoscale mechanical response were the main gains for SHCC research, and other advances can be suggested from this work.

Future works could use the phases segmented in this work by DL as input for mesoscale numerical models, thus being able to validate models not yet validated.

MicroCT techniques that achieve higher resolutions would allow the microstructural quantification in larger specimens, facilitating the correlation with mechanical laboratory tests. In addition to making the segmentation of internal phases more accurate, either by thresholding or by deep learning. Synchronton light microCT is a promising technique for this task.

Furthermore, different in-situ mechanical tests coupled with DVC analysis would improve the material's characterization. The mechanical testing stage with higher load capacity would allow for a greater variety in mechanical tests and specimen sizes.

Lastly, future research could use these techniques for analysis and characterization of other materials. Segmentation by deep learning is quite suitable for any material with complex microstructure and DVC can be applied to any material that has enough microstructural variation.

Bibliography

[1] VAN ZIJL GPAG, WITTMANN FH, OH BH, KALEBE P, TOLEDO FILHO RD, FAIRBAIRN EMR, SLOWIK V, OGAWA A, HOSHIRO H, MECHTCHERINE V, ATMANN F, LEPECH MD. **Durability of strain-hardening cement-based composites (shcc)**. Material and Structures, V.45:pp.1447–1463, 2012.

[2] MECHTCHERINE V, MILLON O, BUTLER M, THOMA K. **Mechanical behaviour of strain hardening cement-based composites under impact loading**. Cement & Concrete Composites, V.33:pp.1–11, 2011.

[3] MINORU K, KEITETSU R. **Recent progress on hpfrcc in japan required performance and applications**. Journal of Advanced Concrete Technology, V.4:pp.19–33, 2006.

[4] PAUL SC, PIRSKAWETZ S, VAN ZIJL GPAG, SCHMIDT W. **Acoustic emission for characterising the crack propagation in strain-hardening cement-based composites (shcc)**. Cement and Concrete Research, V.69:pp.19–24, 2015.

[5] TOSUN-FELEKOGLU K; FELEKOGLU B; LEE BY, LI VC. **The role of flaw size and fiber distribution on tensile ductility of pva-ecc**. Composites Part B: Engineering, V.56:pp.536–545, 2014.

[6] BAY BK, SMITH TS, FYHRIE DP, SAAD M. ***Digital volume correlation: Three-dimensional strain mapping using x-ray tomography***. CExperimental Mechanics, V.39:pp.217–226, 1999.

[7] LORENZONI R, PACIORNIK S, SILVA FA. **Characterization by micro-computed tomography of class g oil well cement paste exposed to elevated temperatures**. Journal of Petroleum Science and Engineering, V.175:pp.896–904, 2019.

[8] LORENZONI R, TINOCO M, PACIORNIK S, SILVA FA. ***The use of X-ray microtomography to investigate the shear behavior of hybrid fiber reinforced strain hardening cementitious composites***. Journal of Building Engineering, V.43:103126, 2021.

[9] LORENZONI R, CUROSU I, PACIORNIK S, MECHTCHERINE V, OPPERMANN M, SILVA FA. **Semantic segmentation of the microstructure of strain-hardening cement-based composites (shcc) by applying deep learning on micro-computed tomography scans**. Cement and Concrete Composites, V.108, 2020.

[10] LORENZONI R, CUROSU I, LÉONARD F, PACIORNIK S, MECHTCHERINE V, SILVA FA, BRUNO G. **Combined mechanical and 3d-microstructural analysis of strain-hardening cement-based composites (shcc) by in-situ x-ray microtomography**. Cement and Concrete Research, V.136:106139, 2020.

[11] LORENZONI R, CUROSU I, PACIORNIK S, MECHTCHERINE V, SILVA FA, BRUNO G. **Digital volume correlation (dvc) applied to in-situ microct images of strain-hardening cement-based composites (shcc)**. Conference: 28 Congresso da Sociedade Brasileira de Microscopia e Microanálise - CSBMM, 2021.

[12] MÜLLER S, MECHTCHERINE V. **Fatigue behaviour of strain-hardening cement-based composites (shcc)**. Cement and Concrete Research, 93:75–83, 2017.

[13] MECHTCHERINE V. **Novel cement-based composites for the strengthening and repair of concrete structures**. Construction and Building Materials, V.41:pp.365–373, 2013.

[14] CUROSU I; MECHTCHERINE V; MILLON O. **Effect of fiber properties and matrix composition on the tensile behavior of strain-hardening cement-based composites (shccs) subject to impact loading**. Cement and Concrete Research, V.82:pp.23–35, 2016.

[15] LI VC, LEUNG CK. **Steady-state and multiple cracking of short random fiber composites**. Journal of Engineering Mechanics, V.118:pp.2246–2264, 1992.

[16] YANG EH, LI VC. **Strain-hardening fiber cement optimization and component tailoring by means of a micromechanical model**. Construction and Building Materials, V.24:pp.130–139, 2010.

[17] YANG EH, LI VC. **Strain-rate effects on the tensile behavior of strain-hardening cementitious composites**. Construction and Building Materials, V.52:pp.96–104, 2014.

[18] CUROSU I, LIEBSCHER M, MECHTCHERINE V, BELLMANN C, MICHEL S. **Tensile behavior of high-strength strain-hardening cement-based composites (hs-shcc) made with high-performance polyethylene, aramid and pbo fibers**. Cement and Concrete Research, V.98:pp.71–81, 2017.

[19] MECHTCHERINE V, SILVA FA, MÜLLER S, JUN P, TOLEDO FILHO RD. **Coupled strain rate and temperature effects on the tensile behavior of strain-hardening cement-based composites (shcc) with pva fibers**. Cement and Concrete Research, V.42:pp.1417–1427, 2012.

[20] HERNÁNDEZ-CRUZ D, OSTERTAG CP, DUNCAN JF, MONTEIRO PJM, NGUYEN W, CELIK K. **In-situ tensile and corrosion damage characterization of fiber-reinforced cementitious composites using x-ray micro-computed tomography**. 9th International Conference on Fracture Mechanics of Concrete and Concrete Structures, 2016.

[21] PACIORNIK S, AUGUSTO KS. **Porosity characterization of iron ore pellets by x-ray microtomography**. Materials Research, V.21, 2018.

[22] LANDIS EN, KRAVCHUK KS, LOSHKOV D. **Experimental investigations of internal energy dissipation during fracture of fiber-reinforced ultra-high-performance concrete**. Frontiers of Structural and Civil Engineering, V.13:pp.190–200, 2019.

[23] AZIMI SM, BRITZ D, ENGSTLER M, FRITZ M. **Advanced steel microstructure classification by deep learning methods advanced steel microstructure classification by deep learning methods**. 2017.

[24] LIU Y, ZHAO T, JU W, SHI S. **Materials discovery and design using machine learning**. Journal of Materiomics, V.3:pp.159–177, 2017.

[25] LIU Y, ZHAO T, JU W, SHI S. **Advanced steel microstructure classification by deep learning methods advanced steel microstructure classification by deep learning methods**. Journal of Materiomics, V.3:pp.159–177, 2017.

[26] ALBUQUERQUE VHC, ALEXANDRIA AR, CORTEZ PC, TAVARES JMRS. **Evaluation of multilayer perceptron and self-organizing map**

neural network topologies applied on microstructure segmentation from metallographic images. NDT and E International, V.42:pp.644–651, 2009.

[27] BÖHM R, STILLER J, BEHNISCH T, ZSCHEYGE M, PROTZ R, RADLOFF S, GUDE M, HUFENBACH W. **A quantitative comparison of the capabilities of *in situ* computed tomography and conventional computed tomography for demage analysis os composites**. Composites Science and Technology, V.110:pp.62–68, 2015.

[28] TUDISCO E; ANDÒ E; CAILLETAUD R; HALL SA. **Tomowarp2: Measuring 3d displacement fields through digital volume correlation**. 3rd International Conference on Tomography of Materials and Structures, Lund, Sweden, p. pp.26–30, 2017.

[29] TUDISCO E; ANDO E; CAILLETAUD R; HALL SA. **Tomowarp2: A local digital volume correlation code**. SoftwareX, V.6:pp.267–270, 2017.

[30] LI VC. **On engineered cementitious composites (ecc) a review of the material and its applications**. Journal of Advanced Concrete Technology, V.6:pp.215–230, 2003.

[31] JUN P; MECHTCHERINE V. **Behaviour of strain-hardening cement-based composites (shcc) under monotonic and cyclic tensile loading. part 1 – experimental investigations**. Cement & Concrete Composites, V.32:pp.801–809, 2010.

[32] PEREIRA EB, FISCHER G, BARROS JAO. **Direct assessment of tensile stress-crack opening behavior of strain hardening cementitious composites (shcc)**. Cement and Concrete Research, V.42:pp.834–846, 2012.

[33] QIAN S; LI VC. **Simplified inverse method for determining the tensile properties of strain hardening cementitious composites (shcc)**. Jounal of Advanced Concrete Technology, V.6 No.2:pp.353–363, 2008.

[34] YU J, CHEN Y, LEUNG CKY. ***Mechanical performance of Strain-Hardening Cementitious Composites (SHCC) with hybrid polyvinyl alcohol and steel fibers***. Composite Structures, V.226:111198, 2019.

[35] YANG E; LI VC. **Strain-rate effects on the tensile behavior of strain-hardening cementitious composites**. Construction and Building Materials, V.52:pp.96–104, 2014.

[36] LI VC; WANG S; WU C. **Tensile strain-hardening behavior of polyvinyl alcohol engineered cementitious composite (pva-ecc)**. Aci Materials Journal, V.98 No.6:pp.483–492, 2001.

[37] OLIVITO RS, ZUCCARELLO FA. ***An experimental study on the tensile strength of steel fiber reinforced concrete***. Composites: Part B, V.41:pp.246–255, 2010.

[38] VAN ZIJL GPAG, WITTMANN FH. **On durability of shcc**. Nuclear Instruments and Methods in Physics Research A, V.8 No.3:pp.261–271, 2010.

[39] ZHANG P; WITTMANN FH; ZHAO TJ; LERMANN EH; TIAN L; VONTOBEL P. **Observation and quantification of water penetration into strain hardening cement-based composites (shcc) with multiple cracks by means of neutron radiography**. Nuclear Instruments and Methods in Physics Research A, V.620:pp.414–420, 2010.

[40] MECHTCHERINE V; JUN P. **Stress-strain behaviour of strain-hardening cement-based composites (shcc) under repeated tensile loading**. 2015.

[41] COROSU I; MECHTCHERINE V; FORNIB D; CADONIB E. **Performance of various strain-hardening cement-based composites (shcc) subject to uniaxial impact tensile loading**. Cement and Concrete Research, V.102:pp.16–28, 2017.

[42] VAN ZIJL GPAG. **Improved mechanical performance: Shear behaviour of strain-hardening cement-based composites (shcc)**. Cement and Concrete Research, V.37:pp.1241–1247, 2007.

[43] BAGHI H; BARROS JAO. **Shear properties of the strain hardening cementitious composite material**. Journal of Materials in Civil Engineering, V.28, 2016.

[44] YUN H. **Flexural behavior and crack-damage mitigation of plain concrete beam with a strain-hardening cement composite (shcc) layer at tensile region**. Composites: Part B, V.45:pp.377–387, 2013.

[45] KAMAL A, KUNIEDA M, UEDA N, NAKAMURA H. **Evaluation of crack opening performance of a repair material with strain hardening behavior**. Cement & Concrete Composites, V.30:pp.863–871, 2008.

[46] LANDIS EN; KEANE DT. **X-ray microtomography**. Materials Characterization, V.61:pp.1305–1316, 2010.

[47] GOMES OFM. ***Processamento e análise de imagens aplicado à caracterização automática de materiais***. Masters thesis, V.102:pp.16–28, 2001.

[48] DENKER JS, GARDNER WR, GRAF HP, HENDERSON D, HOWARD RE, HUBBARD W, JACKEL LD, BAIRD HS, GUYON I. **Neural network recognizer for hand-written zip code digits**. p. pp.323–331, 1989.

[49] GOLOMB BA, LAWRENCE DT, SEJNOWSKI TJ. **Sexnet: A neural network identifies sex from human faces**. 1991.

[50] ZEILER MD, FERGUS R. **Visualizing and understanding convolutional networks**. Experimental Mechanics, p. pp.2–5, 2012.

[51] IGLESIAS JCA, SANTOS RBM, PACIORNIK S. **Deep learning discrimination of quartz and resin in optical microscopy images of minerals**. Minerals Engineering, V.138:pp.79–85, 2019.

[52] DE ALBUQUERQUE VC, TAVARES JMRS, DURÃO LMP. **Evaluation of delamination damage on composite plates using an artificial neural network for the radiographic image analysis**. Journal of Composite Materials, V.44:pp.1139–1159, 2010.

[53] COLLINS PC, WELK B, SEARLES T, TILEY J, RUSS JC, FRASER HL. **Development of methods for the quantification of microstructural features in alpha + beta-processed alpha/beta titanium alloys**. Materials Science and Engineering A, V.508:pp.174–182, 2009.

[54] DOBRZANSKI LA, SROKA M, DOBRZANSKI J. **Application of neural networks to classification of internal damages in steels working in creep service**. Journal of Achievements in Materials and Manufacturing Engineering, V.20, 2007.

[55] DE ALBUQUERQUE VC, CORTEZ PC, DE ALEXANDRIA AR, TAVARES JMRS. **A new solution for automatic microstructures analysis from images based on a backpropagation artificial neural network**. Nondestructive Testing and Evaluation, V.23:pp.273–283, 2008.

[56] SONG Y, HUANG Z, SHEN C, SHI H, LANGE DA. **Deep learning-based automated image segmentation for concrete petrographic analysis**. Cement and Concrete Research, V.135:pp.106118, 2020.

[57] LECUN Y, BENGIO Y, HINTON G. **Deep learning**. Nature, V.521:pp.436–444, 2015.

[58] YANG Z, REN W, SHARMA R, MCDONALD S, MOSTAFAVI M, VERTYAGINA Y, MARROW TJ. **In-situ x-ray computed tomography characterisation of 3d fracture evolution and image-based numerical homogenisation of concrete**. Cement and Concrete Composites, V.75:pp.74–83, 2017.

[59] WAN K, XUE X. **In situ compressive damage of cement paste characterized by lab source x-ray computer tomography**. Materials Characterization, V.82:pp.32–40, 2013.

[60] DE WOLSKI SC, BOLANDER JE, LANDIS EN. **An in-situ x-ray microtomography study of split cylinder fracture in cement-based materials**. Experimental Mechanics, V.54:pp.1227–1235, 2014.

[61] BAY BK. **Methods and applications of digital volume correlation**. Journal of Strain Analysis for Engineering Design, 43:745–760, 2008.

[62] SMITH TS, BAY BK, RASHID MM. **Digital volume correlation including rotational degrees of freedom during minimization**. Experimental Mechanics, 42:272–278, 2002.

[63] FRANCK C, HONG S, MASKARINEC SA, TIRRELL DA, RAVICHANDRAN G. **Three-dimensional full-field measurements of large deformations in soft materials using confocal microscopy and digital volume correlation**. Experimental Mechanics, 47:427–438, 2007.

[64] MOSTAFAVI M, COLLINS DM, CAI B, BRADLEY R, ATWOOD RC, REINHARD C, JIANG X, GALANO M, LEE PD, MARROW TJ. **Yield behavior beneath hardness indentations in ductile metals, measured by three-dimensional computed x-ray tomography and digital volume correlation**. Acta Materialia, 83:468–482, 2015.

[65] FORSBERG F, SJÖDAHL M, MOOSER R, HACK E, WYSS P. **Full three-dimensional strain measurements on wood exposed to three-point bending: Analysis by use of digital volume correlation applied to synchrotron radiation micro-computed tomography image data**. Strain, 46:47–60, 2010.

[66] HUANG J, PAN X, LI S, PENG X, XIONG C, FANG J. **A digital volume correlation technique for 3-d deformation measurements of soft gels**. International Journal of Applied Mechanics, 3:335–354, 2011.

[67] STAMATI O, ANDÒ E, ROUBIN E, CAILLETAUD R, WIEBICKE M, PINZON G, COUTURE C, HURLEY R, CAULK R, CAILLERIE D, MATSUSHIMA T, BÉSUELLE P, BERTONI F, ARNAUD T, LABORIN A, RORATO R, SUN Y, TENGATTINI A, OKUBADEJO O, COLLIAT J, SAADATFAR M, GARCIA F, PAPAZOGLOU C, VEGO I, BRISARD S, DIJKSTRA J, BIRMPILIS G. **spam: Software for practical analysis of materials**. Journal of Open Source Software, 5:2286, 2020.

[68] SAVIJA B; LUKOVIC M; HOSSEINI SAS; PACHECO J; SCHLANGEN E. **Corrosion induced cover cracking studied by x-ray computed tomography, nanoindentation, and energy dispersive x-ray spectrometry (eds)**. Materials and Structures, V.48:pp.2043–2062, 2015.

[69] LIU F, XU K, DING W, QIAO Y, WANG L. **Microstructural characteristics and their impact on mechanical properties of steel-pva fiber reinforced concrete**. Cement and Concrete Composites, 124:104196, 2021.

[70] OBERPEILSTEINER S, REITER T, SALABERGER D. **Coupling of in-situ-ct with virtual testing by fem of short fiber reinforced materials**. International Conference on Industrial Computed Tomography, p. pp.299–305, 2014.

[71] JUNG J; HAMACHI M; OBARA Y; TANIKURA I; WATANABE S. **Analysis of damage in specimen under cyclic uniaxial loading test by x-ray ct method**. 8th Asian Rock Mechanics Symposium, p. pp.365–371, 2014.

[72] SCHLADITZ K. **Quantitative micro-ct**. Journal of Microscopy, V.243:pp.111–117, 2011.

[73] DU PLESSIS A, OLAWUYI BJ, BOSHOFF WP, LE ROUX SG. **Simple and fast porosity analysis of concrete using x-ray computed tomography**. Materials and Structures, V.49:pp.553–562, 2016.

[74] CHANDRAPPA AK, BILIGIRI KP. **Pore structure characterization of pervious concrete using x-ray microcomputed tomography**. Journal of Materials in Civil Engineering, V.30:04018108, 2018.

[75] MACHADO AC, SILVA MA, FILHO RDT, PFEIL MS, LIMA I, LOPES RT. **3d investigation of steel fiber distribution in reinforced concrete by x-ray microtomography**. Revista IBRACON de Estruturas e Materiais, V.8:pp.707–720, 2015.

[76] PACHECO F, CHRIST R, GIL AM, TUTIKIAN BF. **Sem and 3d microtomography application to investigate the distribution of fibers in advanced cementitious composites**. Revista IBRACON de Estruturas e Materiais, V.9:pp.824–841, 2015.

[77] GONZÁLEZ DC, MÍNGUEZ J, VICENTE MA, CAMBRONERO F, ARAGÓN G. **Study of the effect of the fibers' orientation on the post-cracking behavior of steel fiber reinforced concrete from wedge-splitting tests and computed tomography scanning**. Construction and Building Materials, V.192:pp.110–122, 2018.

[78] RÍOS JD, LEIVA C, ARIZA MP, SEITL S, CIFUENTES H. **Analysis of the tensile fracture properties of ultra-high-strength fiber-reinforced concrete with different types of steel fibers by x-ray tomography**. Materials and Design, V.165:107582, 2019.

[79] WANG X; SHEN S; SHI G; XU Y; ZHANG P. **Iterative non-local means filter for salt and pepper noise removal**. Journal of Visual Communication and Image Representation, V.38:pp.440–450, 2016.

[80] SCHINDELIN J; ARGANDA-CARRERAS I; FRISE E; KAYNIG V; LONGAIR M; PIETZSCH T; PREIBISCH S; RUEDEN C; SAALFELD S; SCHMID B; TINEVEZ JY; WHITE DJ; HARTENSTEIN V; ELICEIRI K; TOMANCAK P; CARDONA A. **Fiji: An open-source platform for biological-image analysis**. Nature Methods, V.9:pp.676–682, 2012.

[81] AGAR-OZBEK AS, WEERHEIJM J, SCHLANGEN E, VAN BREUGEL K. **Investigating porous concrete with improved strength: Testing at different scales**. Construction and Building Materials, V.41:pp.480–490, 2013.

[82] TINOCO MP, SILVA FA. **On the mechanical behavior of hybrid fiber reinforced strain hardening cementitious composites subjected to monotonic and cyclic loading**. Journal of Materials Research and Technology, V.11:pp.754–768, 2021.

[82] TINOCO MP, SILVA FA. **Repair of pre-damaged rc beams using hybrid fiber reinforced strain hardening cementitious composites**. Engineering Structures, V.235:112081, 2021.

[84] LIU F, XU K, DING W, QIAO Y, WANG L. **Microstructural characteristics and their impact on mechanical properties of steel-pva fiber reinforced concrete**. Cement and Concrete Composites, V.123:104196, 2021.

[85] FIDELIS MEA, TOLEDO FILHO RD, SILVA FA, MOBASHER B, MÜLLER S, MECHTCHERINE V. **Interface characteristics of jute fiber systems in a cementitious matrix**. Cement and Concrete Research, V.116:pp.252–265, 2018.

[86] RANADE R, LI VC, STULTS MD, RUSHING TS, ROTH J, HEARD WF. **Micromechanics of high-strength , high-ductility concrete**. ACI Materials Journal, V.110:pp.375–384, 2013.

[87] KABELE P. **Multiscale framework for modeling of fracture in high performance fiber reinforced cementitious composites**. Engineering Fracture Mechanics, V.74:pp.194–209, 2007.

[88] LUKOVIĆ M, DONG H, ŠAVIJA B, SCHLANGEN E, YE G, BREUGEL K. **Tailoring strain-hardening cementitious composite repair systems through numerical experimentation**. Cement and Concrete Composites, V.53:pp.200–213, 2014.

[89] KUNIEDA M, OGURA H, UEDA N, NAKAMURA H. **Tensile fracture process of strain hardening cementitious composites by means of three-dimensional meso-scale analysis**. Cement and Concrete Composites, V.33:pp.956–965, 2011.

[90] COROSU I, PIRSKAWETZ S, MECHTCHERINE V. **Characterizing the crack development in strain-hardening cement-based composites (shcc) by means of acoustic emission**. 9th International Conference on Fracture Mechanics of Concrete and Concrete Structures, FraMCoS-9, 2016.

[91] KANG J, BOLANDER JE. **Event-based lattice modeling of strain-hardening cementitious composites**. International Journal of Fracture, V.206:pp.245–261, 2017.

[92] KARAMNEJAD A, SLUYS LJ. **A dispersive multi-scale crack model for quasi-brittle heterogeneous materials under impact loading**.

Computer Methods in Applied Mechanics and Engineering, V.278:pp.423–444, 2014.

[92] TAMSEN E, WEBER W, BALZANI D. **First steps towards the direct micro-macro simulation of reinforced concrete under impact loading**. Pamm, V.18:pp.1–2, 2018.

[94] DE SOUZA NETO EA, BLANCO PJ, SÁNCHEZ PJ, FEIJÓO RA. **An rve-based multiscale theory of solids with micro-scale inertia and body force effects**. Mechanics of Materials, V.80:pp.136–144, 2015.

[95] TROFIMOV A, MISHUROVA T, LANZONI L, RADI E, BRUNO G, SEVOSTIANOV I. **Microstructural analysis and mechanical properties of concrete reinforce d with polymer short fibers**. International Journal of Engineering Science, V.133:pp.210–218, 2018.

[96] LEIBOWITZ M, CLARKE AJ, QIU W, LU X, BALE H, MERTENS JCE, ETCHIN S, HARTWELL R, BRADLEY RS, TRAPP D, ZHANG B, TKACHUK A, HORNBERGER B, HENDERSON K, CORDES NL, PATTERSON BM, MERKLE A, WITHERS PJ. **In situ laboratory-based transmission x-ray microscopy and tomography of material deformation at the nanoscale**. Experimental Mechanics, V.56:pp.1585–1597, 2016.

[97] GEERS MGD, KOUZNETSOVA VG, BREKELMANS WAM. **Multi-scale computational homogenization: Trends and challenges**. Journal of Computational and Applied Mathematics, V.234:pp.2175–2182, 2010.

[98] BULJAC A, JAILIN C, MENDOZA A, NEGGERS J, TAILLANDIER-THOMAS T, BOUTERF A, SMANIOTTO B, HILD F, ROUX S. **Digital volume correlation: Review of progress and challenges**. Experimental Mechanics, V.58:pp.661–708, 2018.

[99] BORDELON AC, ROESLER JR. **Spatial distribution of synthetic fibers in concrete with x-ray computed tomography**. Cement and Concrete Composites, V.53:pp.35–43, 2014.

[100] ABADI M, BARHAM P, CHEN J, CHEN Z, DAVIS A, DEAN J, DEVIN M, GHEMAWAT S, IRVING G, ISARD M, KUDLUR M, LEVENBERG J, MONGA R, MOORE S, MURRAY DG, STEINER B, TUCKER P, VASUDEVAN V, WARDEN P, WICKE M, YU Y, ZHENG X. **Tensorflow: A system for large-scale machine learning**. 12th USENIX Symposium on Operating Systems Design and Implementation, p. pp.265–283, 2015.

[101] CHOLLET F. **https://github.com/keras-team/keras**.

[102] MAKOVETSKY R, PICHE N, MARSH M. **Dragonfly as a platform for easy image-based deep learning applications**. 12th USENIX Symposium on Operating Systems Design and Implementation, V.24:pp.532–533, 2018.

[103] RONNEBERGER O, FISCHER P, BROX T. **U-net: Convolutional networks for biomedical image segmentation**. Proc. Int. Conf. Med. Image Comput. Comput.-Assist. Intervent, p. pp.234–241, 2015.

[104] MÜLLER S, MECHTCHERINE V. **Fatigue behaviour of strain-hardening cement-based composites (shcc)**. Cement and Concrete Research, V.92:pp.75–83, 2017.

[104] SHEHNI A, HÄUSSLER-COMBE U, CUROSU I, GONG T, MECHTCHERINE V. **Numerical simulation of hs-shcc under quasi-static tensile loading**. 10th International Conference on Fracture Mechanics of Concrete and Concrete Structures FraMCoS-X, 2019.

[106] GE SENSING AND INSPECTION TECHNOLOGIES GMBH. **Phoenix nanotom m**. Phoenix nanotom, 2013.

[107] HILDEBOLT CF, WALKUP RK, CONOVER GL, YOKOYAMA-CROTHERS N, BARTLETT TQ, VANNIER MW, SHROUT MK, CAMP JJ. **Histogram-matching and histogramflattening contrast correction methods: A comparison**. Dentomaxillofacial Radiology, V.25:pp.42–47, 1996.

[108] LEE BY; KIM JK; KIM JS, KIM YY. **Quantitative evaluation technique of polyvinyl alcohol (pva) fiber dispersion in engineered cementitious composites**. Cement and Concrete Composites, V.31:pp.408–417, 2009.

[109] MISHUROVA T; RACHMATULIN N; FONTANA P; OESCH T; BRUNO G; RADI E; SEVOSTIANOV I. **Evaluation of the probability density of inhomogeneous fiber orientations by computed tomography and its application to the calculation of the effective properties of a fiber-reinforce d composite**. Cement and Concrete Composites, V.122:pp.14–29, 2018.

[110] KANDA T, LI VC. **Practical design criteria for saturated pseudo strain hardening behavior in ecc**. Journal of Advanced Concrete Technology, 4:pp.59–72, 2006.

[111] LI VC, MISHRA DK, WU HC. **Matrix design for pseudo-strain-hardening fibre reinforced cementitious composites**. Materials and Structures, 28:pp.586–595, 1995.

[112] LI VC, WANG Y, BACKER S. **A micromechanical model of tension-softening and bridging toughening of short random fiber reinforced brittle matrix composites**. Journal of the Mechanics and Physics of Solids, 39:pp.607–625, 1991.

[113] LU C, LEUNG CKY. **A new model for the cracking process and tensile ductility of strain hardening cementitious composites (shcc)**. Cement and Concrete Research, V.79:pp.353–365, 2016.

[114] WU C, LEUNG CKY, LI VC. **Derivation of crack bridging stresses in engineered cementitious composites under combined opening and shear displacements**. Cement and Concrete Research, V.107:pp.253–263, 2018.

[115] YAO J, CHEN Y, WU C, LEUNG CKY. **A new model for calculating inclined single fiber bridging stress in strain-hardening cementitious composites based on beam theory**. Cement and Concrete Composites, V.103:pp.89–103, 2019.

[116] YANG EH, WANG S, YANG Y, LI VC. **Fiber-bridging constitutive law of engineered cementitious composites**. Journal of Advanced Concrete Technology, V.6:pp.181–193, 2008.

[117] LI VC, WANG S. **Microstructure variability and macroscopic composite properties of high performance fiber reinforced cementitious composites**. Probabilistic Engineering Mechanics, V.21:pp.201–206, 2006.

[118] LI M, LI VC. **Rheology, fiber dispersion, and robust properties of engineered cementitious composites**. Materials and Structures/Materiaux et Constructions, V.46:pp.405–420, 2013.

[119] WU HC, LI VC. **Stochastic process of multiple cracking in discontinuous random fiber reinforced brittle matrix composites**. International Journal of Damage Mechanics, V.4:pp.83–102, 1995.

[120] LU C, LI VC, LEUNG CKY. **Flaw characterization and correlation with cracking strength in engineered cementitious composites (ecc)**. Cement and Concrete Research, V.107:pp.64–74, 2018.

[121] RANADE R, LI VC, HEARD WF. **Tensile rate effects in high strength-high ductility concrete**. Cement and Concrete Research, V.68:pp.94–104, 2015.

[122] CUROSU I. **Influence of fiber type and matrix composition on the tensile behavior of strain-hardening cement-based composites (shcc) under impact loading**. 2017.

[123] YU J, CHEN Y, LEUNG CKY. **Mechanical performance of strain-hardening cementitious composites (shcc) with hybrid polyvinyl alcohol and steel fibers**. Composite Structures, V.226, 2019.

[123] HUANG T, ZHANG YX, YANG C. **Multiscale modelling of multiple-cracking tensile fracture behaviour of engineered cementitious composites**. Engineering Fracture Mechanics, V.160:pp.52–66, 2016.

[125] SMOLČIĆ Ž, OŽBOLT J. **Meso scale model for fiber-reinforced-concrete: Microplane based approach**. Computers and Concrete, V.19:pp.375–385, 2017.

[126] ŽIRGULIS G, ŠVEC O, GEIKER MR, CWIRZEN A, KANSTAD T. **Variation in fibre volume and orientation in walls: experimental and numerical investigations**. Structural Concrete, V.17:pp.576–587, 2016.

[127] ERIC B; ASSOCIATE NL; NAGY EN; KEANE DT. **Microtomographic measurements of internal damage in portland-cement-based composites**. Journal of Aerospace Engineering, V.10:pp.2–6, 1997.

[128] NAIK NN; KURTIS KE; WILKINSON AP; JUPE AC; STOCK SR. **Sulfate deterioration of cement-based materials examined by x-ray microtomography**. Proceedings of SPIE - The International Society for Optical Engineering, 2004.

[129] HUANG Y; YANG Z; REN W; LIU G; ZHANG C. **3d meso-scale fracture modelling and validation of concrete based on in-situ x-ray computed tomography images using damage plasticity model**. International Journal of Solids and Structures, V.67-68:pp.340–352, 2015.

[130] AFROUGHSABET V; BIOLZI L; OZBAKKALOGLU T. **High-performance fiber-reinforced concrete: a review**. Journal of Materials Science, V.51:pp.6517–6551, 2016.

[131] DE-DEUS G, MARINS J, NEVES AA, REIS C, FIDEL S, VERSIANI MA, ALVES H, LOPES RT, PACIORNIK S. **Assessing accumulated**

hard-tissue debris using micro-computed tomography and free software for image processing and analysis. Journal of Endodontics, V.40:pp.271–276, 2014.

[132] CUROSU I, MECHTCHERINE V, HERING M, CURABACH M. **Mineral-bonded composites for enhanced structural impact safety - overview of the format, goals and achievements of the research group grk 2250**. 10th International Conference on Fracture Mechanics of Concrete and Concrete Structures FraMCoS-X, 2019.

[133] GONG T, HERAVI AA, ALSOUS G, CUROSU I, MECHTCHERINE V. **The impact-tensile behavior of cementitious composites reinforced with carbon textile and short polymer fibers**. Applied sciences, 2019.

[134] EUROFIBERS. **Dyneema fact sheet, ultra high molecular weight polyethylene fiber form dyneema**. https://issuu.com/eurofibers/docs/name8f0d44, 2010.

[135] SUTTON MA, ORTEU JJ, SCHREIER HW. **Image Correlation for Shape, Motion and Deformation Measurements: Basic Concepts, Theory and Applications**. Springer, 2009.

[136] CORRELATED SOLUTIONS. **Vic-Volume: Reference Manual**. 2009.

[137] PAUL SC, VAN ZIJL GPAG. **Mechanically induced cracking behaviour in fine and coarse sand strain hardening cement based composites (shcc) at different load levels**. Journal of Advanced Concrete Technology, 11:301–311, 2013.

[138] VAN ZIJL GPAG, SLOWIK V, TOLEDO FILHO RD, WITTMANN FH, MIHASHI H. **Comparative testing of crack formation in strain-hardening cement-based composites (shcc)**. Materials and Structures, 49:1175–1189, 2016.

[139] FIGUEIREDO TCSP, CUROSU I, GONZÁLES GLG, HERING M, SILVA FA, CURBACH M, MECHTCHERINE V. **Mechanical behavior of strain-hardening cement-based composites (shcc) subjected to torsional loading and to combined torsional and axial loading**. Materials and Design, 198, 2021.

[140] BAY BK, SMITH TS, FYHRIE DP, SAAD M. **Digital volume correlation: Three-dimensional strain mapping using x-ray tomography**. Experimental Mechanics, 39:217–226, 1999.

[141] MADI K, STAINES KA, BAY BK, JAVAHERI B, GENG H, BODEY AJ, CARTMELL S, PITSILLIDES AA, LEE PD. **In situ characterization of nanoscale strains in loaded whole joints via synchrotron x-ray tomography**. Nature Biomedical Engineering, 4:343–354, 2020.

[142] FLANSBJER M, PORTAL NW, HALL S, ENGQVIST J. **Analysis of failure modes in fiber reinforced concrete using x-ray tomography and digital volume correlation**. Proceedings, 2:401, 2018.

[143] CHATEAU C, NGUYEN TT, BORNERT M, YVONNET J. **Dvc-based image subtraction to detect microcracking in lightweight concrete**. Strain, 54:1–18, 2018.

[144] FRANCKLAB · GITHUB. **https://github.com/francklab**.

[145] BAR-KOCHBA E, TOYJANOVA J, ANDREWS E, KIM KS, FRANCK C. **A fast iterative digital volume correlation algorithm for large deformations**. Experimental Mechanics, 55:261–274, 2015.

[146] ROUBIN E, ANDÒ E, ROUX S. **The colours of concrete as seen by x-rays and neutrons**. Cement and Concrete Composites, 105:103336, 2019.

[147] LUCAS BD, KANADE T. **An iterative image registration technique with an application to stereo vision**. DARPA Image Understanding, p. 121–130, 1981.

[148] AHRENS J, GEVECI B, LAW C. **Paraview: An end-user tool for large-data visualization**. The Visualization Handbook, p. 717–731.